Niels Guertler

Predicting Zonal Flows -

The Reynolds-stress response functional for large-scale flows generated by turbulence in magnetized plasmas

TECHNISCHE UNIVERSITÄT MÜNCHEN
Max-Planck-Institut für Plasmaphysik

- Predicting Zonal Flows -
The Reynolds-stress response functional for large-scale flows generated by turbulence in magnetized plasmas

Niels Christian Guertler

Vollständiger Abdruck der von der Fakultät für Physik
der Technischen Universität München
zur Erlangung des akademischen Grades eines
Doktors der Naturwissenschaften (Dr. rer. nat.)
genehmigten Dissertation.

Vorsitzender:		Univ.-Prof. Dr. L. Oberauer
Prüfer der Dissertation:	1.	Priv.-Doz. Dr. K. Hallatschek
	2.	Univ.-Prof. Dr. R. Metzler

Die Dissertation wurde am 27.01.2011 bei der Technischen Universität München
eingereicht und durch die Fakultät für Physik am 12.10.2011 angenommen.

Abstract

Understanding and reduction of turbulent or anomalous transport in magnetized plasmas is of a primary concern for confinement fusion. In certain regimes the turbulence self-organizes itself and forms large scale poloidal flows, Zonal Flows (ZF). Due to their shearing effect on turbulent eddies they represent an intrinsic key-mechanism towards the reduction of radial transport. It is therefore imperative to account for ZF activity in any description of turbulence more advanced than overall scaling laws in dimensionless parameters or anomalous diffusion coefficients.

Current ZF theories do not self-consistently describe the nearly stationary ZF-turbulence equilibrium and mostly focus on the ZF excitation only. First-principles-plasma-turbulence two-fluid studies are used to examine the excitation and evolution of ZFs and their influence on ion-temperature-gradient turbulence to gain an insight on the ZF-turbulence interaction and the properties of ZFs. The characteristic features observed in the ZF-turbulence equilibria define the requirements upon a functional describing the significant deterministic parts of the perpendicular and parallel Reynolds stresses that govern the ZFs.

Artificial flows are then used in extensive turbulence studies with a slight offset from the self-consistent ZF-turbulence equilibrium to identify the correlations between the perpendicular and parallel stresses, the ZF and the turbulence - all in order to construct a Reynolds stress response functional. It is validated that the functional reproduces all stress features observed in self-consistent ZF studies and that numerical solutions of the ZF momentum equation induced by the functional show the proper ZF characteristics. The constructed stress functional allows, for the first time, a self-consistent prediction of the time-evolution of ZFs and permits a reliable mapping of ZF-turbulence equilibria.

Contents

Chapter 1

Introduction

It is one of the most intriguing facts in toroidally confined fusion plasma physics that the confinement of macroscopically stable equilibria is nonetheless determined by the behavior of micro-instabilities. The transport of particles and heat perpendicular to the magnetic field is governed by small scale turbulence [1, 2, 3, 4] as the other transport processes, classical and neo-classical diffusion [5, 6], are too small to account for the experimentally observed transport values. Understanding of instabilities, turbulence excitation and possible reduction mechanisms for turbulent or anomalous transport is therefore important to improve plasma confinement.
Zonal Flows (ZF) [7, 8, 9], radially varying flux-surface averaged potential perturbations, self-excited by the turbulence represent an intrinsic key-mechanism towards the reduction of radial transport due to their shearing effect on the turbulent eddies [10]. Any turbulence description more advanced than overall scaling laws in dimensionless parameters or anomalous diffusion coefficients is therefore inseparably linked to the comprehension of the excitation and time-evolution of ZFs. As discussed in the following section, current ZF theories up until now either aimed towards an understanding of the initial ZF excitation phase only or were unable to self-consistently predict the time-evolution of the ZF-turbulence equilibrium adequately.
This motivates the detailed examination of the behavior of ZFs and their interaction with the turbulence in first-principles-plasma-turbulence studies within this thesis. From these observations a Reynolds stress response functional that governs the evolution of the ZFs is derived without any of the presuppositions that constrict previous theories. The functional reproduces the major ZF features and allows, for the first time, a self-consistent prediction of the time-evolution of ZFs. This greatly improves the research in plasma confinement as it permits a reliable mapping of ZF-turbulence equilibrium states.

1.1 Overview

Numerous instabilities in confinement equilibria, of which many are reviewed in [1, 2, 3, 4, 6, 11, 12, 13], have been found since they became a focus of interest in the late 1940's. Some instabilities, mostly large scale magnetohydrodynamic, can be suppressed by customized

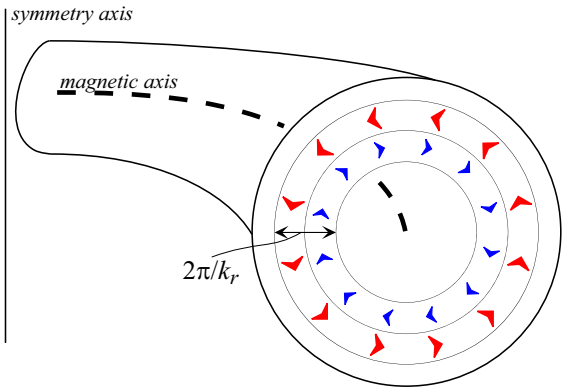

Figure 1.1: Schematics of Zonal Flows with a characteristic radial wave-number k_r in an axisymmetric magnetic confinement plasma.

confinement field configurations [14, 15, 16] or adaptive feedback methods [17]. But, the temperature and density gradients inherent to a confined fusion plasma always constitute an energy source for gradient-driven micro-instabilities, e.g. drift-waves (DW) [18, 19] or ion-temperature-gradient (ITG) [20] modes (both shortly revisited in Chap. 3), that generally saturate in a turbulent state.

Many early studies of turbulent transport restricted themselves to describing the plasma with scaling-laws or anomalous-diffusion coefficients [1, 2, 3, 4, 21, 22], often employing weak turbulence approximations. This approach is already questionable when several microscale instabilities coexist, which is usually the case, and the different diffusivity contributions cannot be identified anymore due to strong nonlinear interaction. Moreover, the method is entirely inadequate to describe the experimentally observed turbulence bifurcations, e.g. the transition to an improved confinement mode (H-mode) [23] with very steep gradients on the edge of the confinement region or the formation of an internal transport barrier [24, 25].

To gain a deeper insight into the turbulence interaction the focus of interest shifted towards the analysis of the entire turbulence spectrum both theoretically [26, 27, 28] and experimentally [29] in the 1970's as opposed to the previous restriction to a spectrum integrated diffusion coefficient or scaling law. As the plasma motion in a strong magnetic field is highly anisotropic, because gyration restricts perpendicular motion, the turbulence scales along the field are large whereas perpendicular they are short, which suggested that a confined plasma may have some properties of two-dimensional turbulence, e.g. inverse cascades from small scales to large scales [30]. And indeed an inverse cascade of energy towards large scales was revealed in a three-wave cascade model [7]. It was found that the energy condensates in a flow with a poloidal wave-number $k_\theta = 0$ and a characteristic radial wave-number $k_r = k_c$, forming nested layers of clockwise and counterclockwise poloidal flows (Fig. 1.1). In analogy to the same phenomenon observed in atmospheric Rossby waves [31] these flows were named Zonal Flows (ZF). A later study of DW turbulence in a cylindrically confined plasma demonstrated the ZF self-formation process directly [8].

The question of a ZF generation mechanism is instructively answered in a fluid framework: An average $\langle \ldots \rangle$ (discussed in detail in chap. 4) of the fluid momentum equation yields a Reynolds stress contribution $\langle \tilde{v}_r \tilde{v}_\theta \rangle$ to the ZF momentum equation

$$\partial_t \langle v_\theta \rangle \sim -\partial_r \langle \tilde{v}_r \tilde{v}_\theta \rangle \ , \tag{1.1}$$

where $\langle v_\theta \rangle$ is the ZF velocity and $\tilde{v}_r$ and $\tilde{v}_\theta$ are the turbulent radial and poloidal velocity fluctuations. Thus, the divergence of a Reynolds stress generated by anisotropic turbulence can excite ZFs [32].

Assuming a spatiotemporal scale separation between the ZFs and the ambient turbulence an effort was made to separate the dynamics into two coupled equations [33] and explain the ZF-turbulence interaction with a wave-kinetic scattering process of turbulence quanta on shear flows [34]. The growth of ZFs as a "self-organized instability" was observed but no description for the time-evolution was derived [33].

With the increase of available supercomputer power in the 1990's turbulence computations including temperature fluctuations and toroidal geometry became possible: A local gyro-fluid ITG-turbulence study in toroidal geometry revealed that ZFs are excited by ITG-turbulence in the plasma core region and that they are essential for the saturation of radial heat transport [10]. It was further pointed out that the ZF-turbulence equilibrium wave-number spectrum is down-shifted from the fastest growing linear mode of the primary instability. A global gyro-kinetic ITG-turbulence study in toroidal geometry [35] validated that a key mechanism for the reduction of transport is the breaking apart of eddies by the ZF and thus a reduction of the radial decorrelation length, as suggested in [36, 37]. It was also shown that the radial profile of the ZFs in local and global simulations is qualitatively similar.

An analytic analysis of potential saturation mechanisms yielded that stationary poloidal flows are not damped by linear collisionless processes [38], e.g. Landau damping, but are subject to ion-collisional damping [39], implying larger poloidal flows at high temperatures since the collision frequency $\nu_{ii} \sim T^{-3/2}$ scales inversely with the temperature. This was supported by collisional gyro-kinetic studies [40, 41] of marginal ZFs where a linear dependence between ion diffusivity and collision frequency and further a proportionality between the anomalous transport and the mean square of the turbulence fluctuations was observed. Another study revealed that ZFs are not prone to Kelvin-Helmholtz (KH) like instabilities even though their profile varies radially with neighboring ranges of different poloidal velocities [42]. This rules out KH instabilities as a saturation mechanism for poloidal flows.

To describe the ZF-turbulence bidirectional feedback mechanism it was suggested that the turbulence and ZF intensities follow a "predator-prey" behavior since the ZFs reduce the turbulence intensity by shear suppression on one hand and the drift waves appear to be modulationally unstable to shear flow perturbations on the other [43, 44]. Within this framework it was shown that in the transitional regime, between weakly and strongly collisionally damped ZFs, bifurcations in the turbulence intensity can occur [45, 46, 47]. However, observation of an offset (Dimits shift) to the linear ITG instability threshold, i.e. a total quench of turbulence, due to a stable residual ZF [48] already indicates that

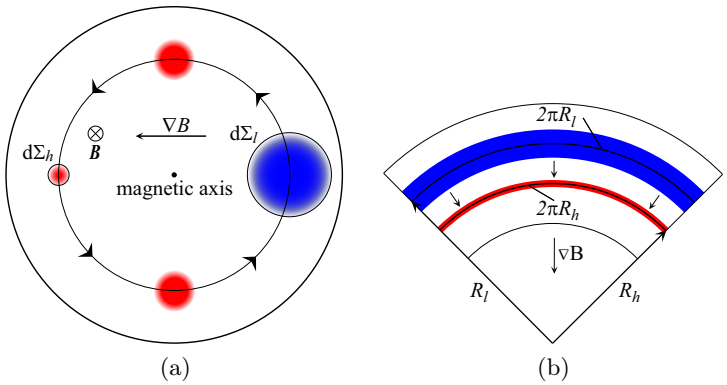

Figure 1.2: **(a)** Schematic of the poloidal cross-section of a toroidal confinement configuration. A fluid element with the cross-section $\mathrm{d}\boldsymbol{\Sigma}_l$ is moving poloidally to the high field side $\mathbf{B}_h$ and magnetic flux conservation results in a perpendicular compression. **(b)** Top view of a section of a toroidal confinement configuration. A fluid element moving poloidally from radius R_l to R_h is additionally compressed in the parallel direction due to the arclength difference. Therefore the volume dV of the poloidally moving fluid element is proportional to $dV \sim R^2$.

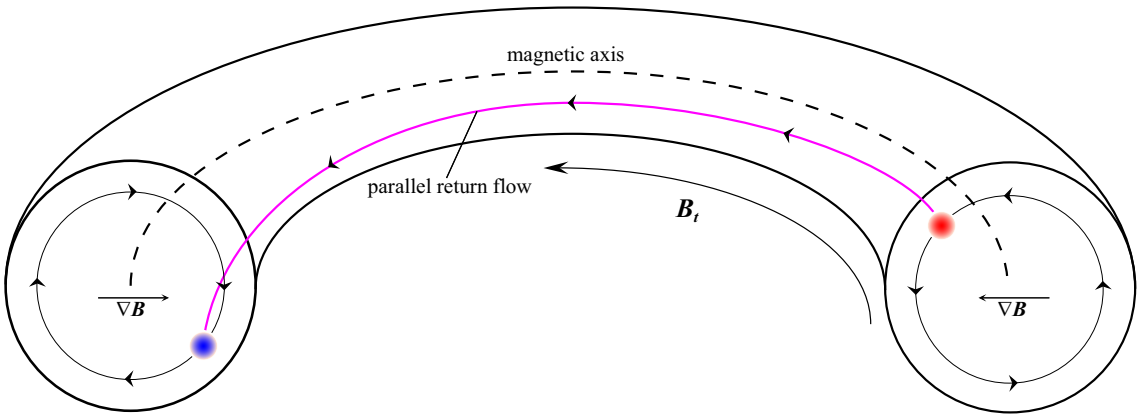

Figure 1.3: Half section of a toroidal confinement configuration. Schematic of the parallel return flow connecting perpendicular compression (red) with expansion regions (blue).

the "predator-prey" model oversimplifies the complex ZF-turbulence interaction as the "predator", the ZF, can survive without any "prey"-turbulence.

All the aforementioned ZF observations and theories restricted themselves to purely poloidal flows. However, stationary flows of this kind are only possible in a geometry without a geodesic curvature [49]. In a toroidal, highly conductive configuration with a magnetic field pressure significantly stronger than the thermal pressure the poloidal magnetic flux is conserved such that a fluid volume moving purely poloidally from the low field side $\mathbf{B}_l$ to the high field side $\mathbf{B}_h$ is compressed, since $\int \mathbf{B}_l \cdot \mathrm{d}\mathbf{\Sigma}_l = \int \mathbf{B}_h \cdot \mathrm{d}\mathbf{\Sigma}_h$ (Fig. 1.2a), where $\mathrm{d}\mathbf{\Sigma}$ is an area element of the poloidal cross section of the fluid element. The magnetic field is mostly toroidal $|\mathbf{B}| \sim 1/R$ and the arclength of the field lines is proportional to the radius R (Fig. 1.2b), hence the change in density of a poloidally moving fluid volume is $n_h/n_l = R_l^2/R_h^2$. Assuming an adiabatic process, the change in pressure is $p_h/p_l = (n_h/n_l)^{5/3} = (R_l/R_h)^{10/3}$. For typical values $R_l = 2\mathrm{m}$ and $R_h = 1\mathrm{m}$, the change in pressure is $p_h/p_l \approx 10$, which is well beyond what the available energy in the fluctuations could sustain. A parallel flow component is therefore essential for stationary ZFs to cancel the divergence of the poloidal flow [49], otherwise the accumulating pressure perturbation will result in an oscillating motion called Geodesic-Acoustic-Mode (GAM) [50, 51, 9]. Thus stationary ZFs are primarily expected in the core of a toroidal plasma where the parallel flow is strong, due to the small safety factor, whereas the edge is dominated by the GAMs.

Figure 1.3 shows how a fluid element moving poloidally from the low to the high-field side is perpendicularly compressed on the top side of the torus and decompressed on the bottom when moving from the high to low-field side. The return flow along the field lines connects regions of opposite pressure fluctuations on the top and bottom side thus canceling the divergence of the poloidal flow [49]. It can further be shown that the parallel flow represents the major part of the ZF energy [49] and its inclusion into a theory for ZFs is therefore imperative.

The most recent analytic ZF theories [52, 53, 54] refined and extended the wave-kinetic DW approach of [33] to derive a description for the steady state of ZFs. The theory states that the ZF-turbulence equilibrium can be categorized in three regimes for collisionally damped ZFs. The first regime is characterized by unstable DWs but absent ZFs for small turbulence-energy growth rates γ_L. The second regime is defined by an increasing ZF amplitude while the DW fluctuation level remains constant for increasing γ_L. In this case the transport coefficient appears to be highly dependent on the collisional damping of the ZFs, which reproduces previous results [40, 45, 55]. In the third regime both the level of DW fluctuations and of ZFs are most unstable and increase with γ_L whereas the transport is only weakly dependent on collisionality [56]. The collisionless case on the other hand shows a total quench of turbulence by a residual saturated ZF for small γ_L and a behavior similar to regime three of the collisional case for a γ_L above the critical threshold for the onset of DW turbulence with ambient shear flows [54]. In both cases, collisional and collisionless, of highly unstable ZFs, the level of turbulence remained finite which explains the weak dependence of the transport coefficients on collisionality observed in high temperature plasmas [56]. The wave-kinetic effect of concentration of fluctuation

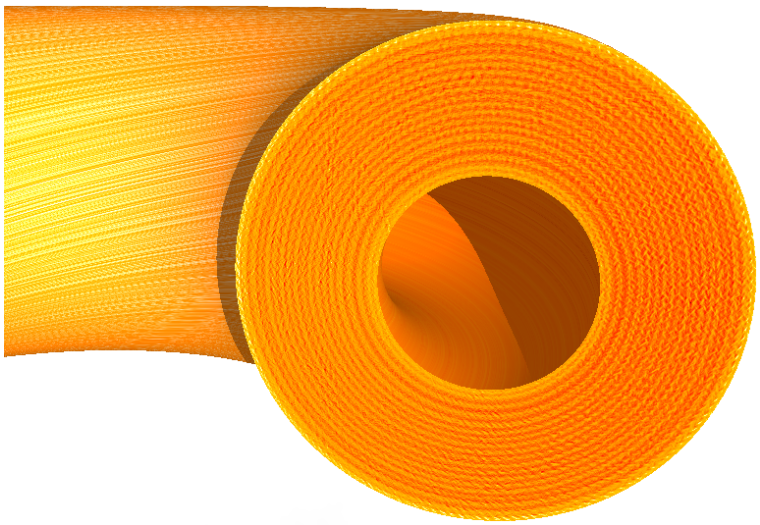

Figure 1.4: Poloidal ZF velocity from a large-aspect-ratio turbulence study, using the two-fluid code NLET [64], mapped to a torus.

energy, observable as local peaks in the radial heat-flux, favoring one poloidal flow direction (electron diamagnetic drift direction) over the other has been directly observed in numerical studies [57]. For a summary of the state of progress in ZF theory the reader is referred to [9].

Experimental measurements of stationary ZFs in the core remain difficult due to the high temperatures, but, employing heavy-ion-beam-probes (HIBP) [58, 59, 60] or beam-emission spectroscopy [61], the existence of stationary ZF with a characteristic radial scale was verified. For an extensive review of ZF measurements the reader is referred to [62].

Although all the previously mentioned ZF theories describe at least one detail in the ZF-turbulence behavior qualitatively adequate they should not be taken too literally. Neither can the turbulence in confined plasmas always be considered weak [63], confounding the weak turbulence based theories, nor is there a strict spatial scale separation between ZFs and turbulence, necessary for a wave-kinetic approach (details discussed in chap. 4). Additionally, the inverse cascade occurs in one major step as opposed to an incremental cascade from small over intermediate to large scales [63]. Moreover, theories that do include the parallel flow component [53, 54] still treat the corresponding parallel stress contribution simplified to a viscous modification of the ZF growth rate only. Even more importantly, none of the theories can reproduce the robust characteristic radial scale observed in numerical studies [49, 63] and thus cannot predict the ZF time-evolution, which will be demonstrated in chap. 5.

1.2 Outline

Figure 1.4 shows a ZF pattern in a tokamak confinement configuration obtained using the two-fluid code NLET [64]. The pattern changes only slowly over a time much larger than the turbulence time scale or even the time scale of one toroidal sound wave transit and it possesses a characteristic radial scale length which suggests a dominant deterministic mechanism governing its evolution.
The intent of this thesis is to find a self-consistent functional for the Reynolds stress governing the ZF evolution using extensive first-principles plasma-turbulence-computations only. The requirement upon the functional is that it reproduces all observed deterministic ZF features with the smallest number of degrees of freedom necessary. As both ZFs and turbulence are inseparably linked, a good understanding of the ZF-turbulence interaction is imperative to make predictions of the turbulence level and thus confinement capabilities in fusion devices. The derived stress approximation greatly simplifies further studies of the turbulence behavior as it describes the ZF excitation and evolution in a compact and comprehensible form. It is the first indispensable ingredient towards a plasma turbulence description that remains valid even in the vicinity of transport bifurcations as it allows a much more detailed insight into the turbulence evolution than overall scaling laws or anomalous diffusion coefficients provide.
For the analysis a two-fluid framework, NLET [64], will be used rather than a gyro-kinetic one because both qualitatively reproduce the evolution of ZFs in the regime of interest but the fluid description comes at a lower computational expense. The outline of the thesis is the following:
Chapter 2 concisely recapitulates some basics of plasma physics, toroidal confinement and the derivation of the fluid equations used in the following chapters and is mostly intended as a guideline for a reader unfamiliar with plasma physics.
Chapter 3 gives a summary of the DW and ITG instability mechanisms and the dispersion relations and illustrates a mechanism how small scale turbulence self-organizes itself into larger scales through an inverse cascade process [65]. The differences between the linear and turbulent ITG states with artificially suppressed ZFs are discussed using turbulence studies to elucidate the changes in the fluctuation spectra before the onset of ZF activity.
Chapter 4 is dedicated to the observation of characteristic features of ZFs and turbulence and their influence on each other in turbulence studies. First the $\mathbf{E} \times \mathbf{B}$- and diamagnetic-velocity contributions to the perpendicular stress are compared. The initial excitation phase of ZFs is examined to identify the turbulent behavior necessary to trigger the transition into a ZF-turbulence equilibrium state. The differences between the scale lengths and amplitudes of the initial and equilibrium states of self-consistently excited ZFs is exemplified. It is shown on what time scale the ZF pattern changes and examined how turbulent states, artificially modified by arbitrary flows, evolve. Further, the time-evolution of the stresses is studied to determine the level of determinism in the stresses and to demonstrate the influence of the different contributions in the ZF momentum equation. The ZF evolution in the two-fluid framework is compared with one obtained from the gyro-kinetic code GYRO [66] to justify the use of the two-fluid approach.
The response of self-consistent ZFs to strong local fluctuations of the radial heat-flux Q is

examined. Fixed artificial flow profiles slightly away from the ZF-turbulence equilibrium state are used to elucidate the corrugating influence the shear-flows exert upon the heat-flux, and to investigate the different turbulence responses with respect to flows in ion- and electron-diamagnetic drift direction. Furthermore, the relation between the radial heat-flux gradient $\partial_x \ln Q$ and the ZF shearing rate is studied and extensive turbulence studies with artificial flows of varying radial scales and amplitudes divulge the dependence of the radial average heat-flux level on both amplitude and scale of the ZFs. Additional studies with flow patterns alternating over time give an insight into the "memory" the turbulence possesses of the flows it was previously subjected to.

Chapter 5 is dedicated to the construction of the Reynolds stress functional and contains the most essential results of this thesis. It is shown that two degrees of freedom out of the large amount available for the turbulence are already sufficient to construct a functional describing the observed ZF evolution. Extensive turbulence studies with various artificial flow patterns and turbulence levels close to the self-consistent ones are used to identify the major deterministic features in the stress responses. The structures of the perpendicular and parallel stress contributions are thereby treated as equally important, in contrast to the approaches in previous ZF models, where only a viscous modification of the linear ZF growth rate accounted for a parallel contribution. It is demonstrated in what way the stresses relate to the turbulence level as well as its corrugations. The nonlinear, wavelength dependent stress functional constructed from these observations is used to reconstruct the stress patterns of self-consistent ZFs and it is verified that it reproduces all occurring prominent features observable in the stresses for a supplied shearing rate and turbulence pattern. However, numerical solutions of the ZF momentum equation, induced by the stress functional constructed from the aforementioned observations, do not reproduce the time-evolution of ZFs from arbitrary initial states adequately. To identify the term missing for a satisfactory reproduction of the ZF evolution, the evolution of ZFs observed in turbulence studies is compared to the evolution predicted by a growth rate derived from the nonlinear stress functional extended by a candidate term within a mean-field theory framework. Common approximation techniques, e.g. a least-squares approximation, failed to adequately verify the missing term for the stress functional as they yield sets of approximation coefficients qualitatively indistinguishable but quantitatively different depending on the level of random fluctuation remnants, interfering artificial artifacts (e.g. boundary effects) or locally different turbulence behavior. To, nevertheless, affirm the extended functional under these difficult conditions a minimal variance estimator method is developed. The estimator is used to measure the stress response behavior to a perturbatory flow for an ensemble of turbulence studies with artificial flows. Comparison of this measured stress contribution with the growth behavior described by the extended functional finally yields the desired verification which is further corroborated by numerical solutions of the ZF momentum equation, induced by the extended functional, now reproducing the evolution of ZFs from arbitrary initial states.

Chapter 6 discusses the wave-kinetic approach used in e.g. [53, 54, 32, 52, 67, 68] and derives a stress approximation analytically. The dispersion relation and observed turbulence behavior of the ITG-instability discussed in chapter 3 are used to make qualitative estimates about the analytic coefficients and compare them to the results of chapter 5.

Furthermore, it is elucidated why current wave-kinetic theories describe the ZF-turbulence equilibrium evolution inadequately so far.
The result of this thesis, a Reynolds stress response functional for ZFs, is summarily discussed in chapter 7.

Chapter 2

The Two-fluid Description of a Magnetically Confined Plasma

This chapter summarizes the basic properties of plasma confinement physics and explains the two-fluid description. It is primarily intended as a concise guideline for a reader unfamiliar with the intricacies of plasma physics. The set of turbulence equations used throughout the following chapters is shown at the end of section 2.3.

2.1 Confined Plasma Equilibrium

A plasma is a quasi-neutral gas of electrons and ions. Near the thermodynamical equilibrium the densities for the species $s \in \{i, e\}$ are distributed according to the Maxwell-Boltzmann equation $n_s = n_0 e^{-e_s \phi_0 / T}$ with e_s the charge, T the equilibrium temperature and the electrostatic potential ϕ_0. For small deviations from the equilibrium the densities are $n_s \approx n_0 \left(1 - e_s \phi / T\right)$ and the total charge density of a plasma with singly charged species is $\rho_p \equiv e \left(n_i - n_e\right) = -2e^2 n_0 \phi / T$. The potential perturbation, caused by a small localized charge density $\rho_t = q_0 \delta^3 \left(\mathbf{r}\right)$ with the Dirac δ-function, can be derived from the Poisson-equation

$$\begin{aligned} \Delta\phi &= -4\pi \left(\rho_p + \rho_t\right) / c \\ &= -4\pi \left(q_0 \delta^3 \left(\mathbf{r}\right) - 2e^2 n_0 \phi / T\right) / c \,, \end{aligned} \tag{2.1}$$

which has the solution $\phi(r) = q_0 e^{-r/\lambda_D} / cr$ where $\lambda_D = \sqrt{cT / 4\pi e^2 n_0}$ is the Debye-length. For scales L that are significantly larger than $L \gg \lambda_D$ the potential is $\phi(L) \approx 0$ and hence one can assume in this case that the plasma is quasi-neutral $n \equiv n_i = n_e$ [69].

The interaction of the plasma with electromagnetic fields is described by Maxwell's equations. However, since the time scales of electromagnetic waves and the plasma phenomena

of interest differ in several magnitudes the displacement current $\partial_t \mathbf{E}$ is neglected. Therefore the Maxwell equations in CGS units for the plasma are

$$\nabla \cdot \mathbf{E} = 0 \tag{2.2}$$
$$\nabla \cdot \mathbf{B} = 0 \tag{2.3}$$
$$\nabla \times \mathbf{B} = 4\pi \mathbf{j}/c \tag{2.4}$$
$$\nabla \times \mathbf{E} = -\partial_t \mathbf{B}/c\,, \tag{2.5}$$

with $\mathbf{B} = \nabla \times \mathbf{A}$, $\mathbf{E} = -\nabla\phi - \partial_t \mathbf{A}/c$ and $\nabla \cdot \mathbf{j} = 0$.
The idea behind magnetic confinement is to use the Lorentz force to balance the pressure gradient, $\nabla p = \mathbf{j} \times \mathbf{B}/c$, in the plasma. It is useful to note that this equilibrium relation can be rewritten as

$$\boldsymbol{\kappa} = 4\pi \nabla p / cB^2 + \nabla_\perp B/B\,, \tag{2.6}$$

where $\boldsymbol{\kappa} \equiv \hat{\mathbf{b}} \cdot \nabla \hat{\mathbf{b}}$ is the curvature and $\nabla_\perp \equiv \nabla - \hat{\mathbf{b}} \cdot \nabla$ with $\hat{\mathbf{b}} \equiv \mathbf{B}/B$. In a cylindrical coordinate system $(\hat{\mathbf{e}}_\mathbf{R}, \hat{\mathbf{e}}_\mathbf{z}, \hat{\mathbf{e}}_\varphi)$ an axisymmetric configuration ($\varphi = 0$ and $\partial_\varphi = 0$) for the magnetic field $\mathbf{B}$ and current $\mathbf{j}$ is defined by

$$\mathbf{B} = \hat{\mathbf{e}}_\mathbf{R} \partial_z A_\varphi + \hat{\mathbf{e}}_\varphi \left(\partial_R A_z - \partial_z A_R\right) - \hat{\mathbf{e}}_\mathbf{z} \partial_R \left(R A_\varphi\right)/R \tag{2.7}$$
$$4\pi \mathbf{j}/c = \hat{\mathbf{e}}_\mathbf{R} \partial_z B_\varphi + \hat{\mathbf{e}}_\varphi \left(\partial_R B_z - \partial_z B_R\right) - \hat{\mathbf{e}}_\mathbf{z} \partial_R \left(R B_\varphi\right)/R \tag{2.8}$$
$$\Psi \equiv R A_\varphi \tag{2.9}$$
$$F \equiv R B_\varphi\,. \tag{2.10}$$

Using the definitions for Ψ and F and the relation $\hat{\mathbf{e}}_\varphi \cdot \nabla \Psi = 0$ in the equations (2.7) and (2.8) results in

$$R\mathbf{B} = \nabla \Psi \times \hat{\mathbf{e}}_\varphi + F \hat{\mathbf{e}}_\varphi \tag{2.11}$$
$$4\pi R \mathbf{j}/c = \nabla F \times \hat{\mathbf{e}}_\varphi + 4\pi R j_\varphi \hat{\mathbf{e}}_\varphi / c\,. \tag{2.12}$$

This infers that $\nabla \Psi \cdot \mathbf{B} = 0$ and, using $\hat{\mathbf{e}}_\varphi \cdot \nabla p = 0$,

$$0 = \mathbf{j} \times \mathbf{B} \cdot \mathbf{B}/c = \nabla p \cdot \mathbf{B} = (\nabla \Psi \times \hat{\mathbf{e}}_\varphi) \cdot \nabla p = (\nabla p \times \nabla \Psi) \cdot \hat{\mathbf{e}}_\varphi\,, \tag{2.13}$$

showing that $\Psi = \text{const}$ is a magnetic surface and an isobar with $\nabla p \parallel \nabla \Psi$. In a local coordinate system $(\hat{\mathbf{e}}_\psi, \hat{\mathbf{e}}_\xi, \hat{\mathbf{e}}_\varphi)$ (Fig. 2.1) with $\hat{\mathbf{e}}_\psi \equiv \nabla\Psi/|\nabla\Psi|$ and $\hat{\mathbf{e}}_\xi \equiv \hat{\mathbf{e}}_\psi \times \hat{\mathbf{e}}_\varphi$ the components B_ξ and j_ξ defined by Eqs. (2.11) and (2.12) are

$$B_\xi = -\hat{\mathbf{e}}_\psi \cdot \nabla \Psi / R \tag{2.14}$$
$$j_\xi = -c \hat{\mathbf{e}}_\psi \cdot \nabla F / 4\pi R \tag{2.15}$$

showing that Ψ is the poloidal flux. Using these results in the $\hat{\mathbf{e}}_\psi$ component of the equilibrium condition $\nabla p = \mathbf{j} \times \mathbf{B}/c$ gives

$$\begin{aligned} \hat{\mathbf{e}}_\psi \cdot \nabla p &= \hat{\mathbf{e}}_\psi \cdot (\mathbf{j} \times \mathbf{B})/c \\ &= (j_\xi B_\varphi - j_\varphi B_\xi)/c \\ &= -\hat{\mathbf{e}}_\psi \cdot \nabla F B_\varphi / 4\pi R + j_\varphi \hat{\mathbf{e}}_\psi \cdot \nabla \Psi / cR \end{aligned} \tag{2.16}$$

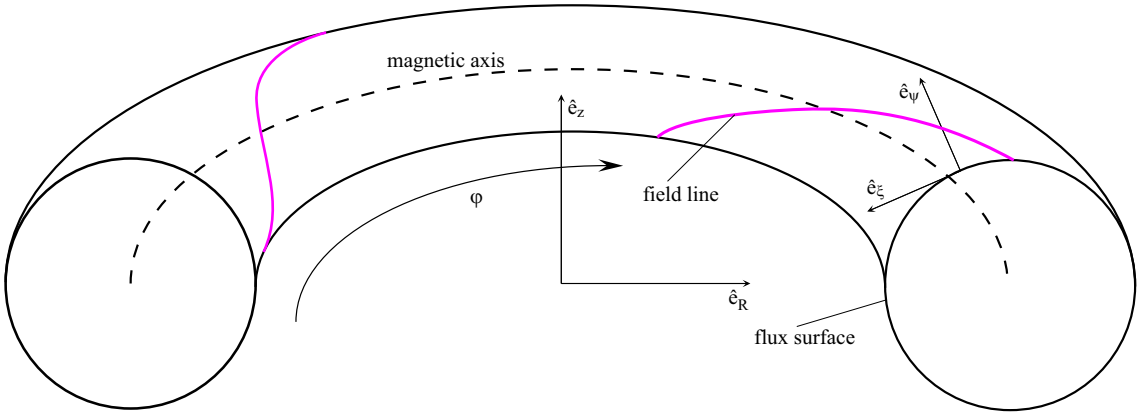

Figure 2.1: Cylindrical $(\hat{\mathbf{e}}_\mathbf{R}, \hat{\mathbf{e}}_\mathbf{z}, \hat{\mathbf{e}}_\varphi)$ and local coordinates $(\hat{\mathbf{e}}_\psi, \hat{\mathbf{e}}_\xi, \hat{\mathbf{e}}_\varphi)$.

which defines the φ component of the current

$$j_\varphi = cR\partial_\Psi p + cF\partial_\Psi F/4\pi R\,. \tag{2.17}$$

Since equation (2.8) simultaneously requires $4\pi j_\varphi R/c = -R\partial_R\left(\partial_R\Psi/R\right) + \partial_z^2\Psi$, the Grad-Shafranov equation [70] for an axisymmetric toroidal equilibrium in cylindrical coordinates is

$$R\partial_R\left(\partial_R\Psi/R\right) + \partial_z^2\Psi = -4\pi R^2\partial_\Psi p + F\partial_\Psi F\,. \tag{2.18}$$

An alternative, more convenient form of the Grad-Shafranov operator Δ^*, the left hand side of (2.18), in general coordinates is

$$\Delta^* \equiv R^2\nabla\cdot\frac{\nabla}{R^2}\,. \tag{2.19}$$

In a toroidal coordinate system $(\hat{\mathbf{e}}_\mathbf{r}, \hat{\mathbf{e}}_\theta, \hat{\mathbf{e}}_\varphi)$ defined by

$$\begin{aligned} x &= (r_0 + r\cos\theta)\cos\varphi \\ y &= (r_0 + r\cos\theta)\sin\varphi \\ z &= -r\sin\theta \end{aligned} \tag{2.20}$$

the Grad-Shafranov operator takes the form of

$$\Delta^* = \partial_r^2\Psi + \frac{r_0\partial_r\Psi + \sin\theta\partial_\theta\Psi}{r\left(r_0 + r\cos\theta\right)} + \frac{1}{r^2}\partial_\theta^2\Psi\,. \tag{2.21}$$

To find an equilibrium solution of (2.18) for the asymptotic small inverse aspect ratio limit, $\epsilon \equiv r/r_0 \to 0$, it is assumed that the lowest order of $\Psi(r,\theta,\phi)$ in ϵ is $\Psi_0(r)$ dependent only on r [70, 71, 72]. Using $B_\theta = \hat{\mathbf{e}}_\theta\cdot\nabla\times\mathbf{A} = -\partial_r\Psi/r_0$, the Grad-Shafranov equation in the limit $\epsilon\to 0$ reduces to

$$\begin{aligned} \frac{-r_0}{r}\partial_r\left(rB_\theta\right) &= 4\pi r\partial_r p\partial_{\Psi_0} r - F\partial_r F\partial_{\Psi_0} r \\ &= \frac{4\pi r_0}{B_\theta}\partial_r p + \frac{r_0 B_\varphi}{B_\theta}\partial_r B_\varphi \end{aligned} \tag{2.22}$$

with $\Delta^* \to \partial_r \left(r \partial_r \Psi_0\right)/r$. Thus, after rearranging the terms, the equilibrium condition is

$$\partial_r \left[B_\varphi^2 + B_\theta^2 + 8\pi p\right] = -\frac{2B_\theta^2}{r}\,. \tag{2.23}$$

In case of a vanishing pressure gradient $\partial_r p = 0$, e.g. at the plasma surface, the equation has a solution of the form $f(r) \equiv B_\varphi^2 + B_\theta^2$ with $f(r)$ a generating function that satisfies $\partial_r f \leq 0$ and $f + r\partial_r f/2 \geq 0$. The magnetic field is given by $B_\theta = \sqrt{-r\partial_r f/2}$ and $B_\varphi = \sqrt{f + r\partial_r f/2}$. For the solution $f(r) = B_0^2/\left(1 + r^2/r_0^2\right)$ the magnetic field is

$$\mathbf{B} = \frac{B_0}{1 + r^2/r_0^2}\frac{r}{r_0}\hat{\mathbf{e}}_\theta + \frac{B_0}{1 + r^2/r_0^2}\hat{\mathbf{e}}_\varphi\,. \tag{2.24}$$

This describes a concentric helical field configuration around $(\cos\varphi, \sin\varphi, 0)\, r_0$. with a pitch between the toroidal and poloidal fields $B_\varphi/B_\theta = r_0/r$. The solutions of (2.23) for an arbitrary pressure gradient are nested concentric flux surfaces with a radially changing field line pitch [70, 72, 71]. This simple equilibrium allows studies of the basic plasma turbulence behavior [73, 74] in a curved toroidal field without the higher order effects caused by a more complex geometry and will be used for the turbulence studies in the following chapters. In experimental devices, the toroidal field is generated by poloidal field coils whereas the poloidal field is generated by a toroidal plasma current induced by a central field coil along the symmetry axis. This confinement configuration is called a tokamak and a more detailed introduction is given in [6] (for non axisymmetric magnetic configurations, e.g. stellarators see [75]).
A measure for the field line pitch on a flux surface is the safety factor

$$q \equiv \frac{1}{2\pi}\oint dl \frac{B_\varphi}{R B_p} \tag{2.25}$$

where B_p is the poloidal field and dl is a poloidal path element. For a high aspect-ratio configuration with circular flux-surfaces this formula gives

$$q = \frac{r B_\varphi}{r_0 B_\theta}\,, \tag{2.26}$$

which can be interpreted as the number of toroidal circuits following a field line necessary to execute one poloidal rotation. The magnetohydrodynamic (large scale) stability of a tokamak depends highly on the radial q-profile [14, 15, 16, 6] but it also defines the regions of stationary ZF activity [63]. The global shear –radial change of q– is defined as

$$s \equiv \frac{r}{q}\partial_r q\,. \tag{2.27}$$

The radially changing local field line pitch can be measured by a local shear length which is defined as follows. A path element of length $\mathrm{d}l_\parallel$ along the magnetic field from a point $P_1(r_1)$ to $P_2(r_1)$ on a flux surface at r_1 is $\mathrm{d}\mathbf{v}_1 \equiv \mathrm{d}l_\parallel \hat{\mathbf{b}}$. The connection vector from $P_1(r_1)$ to a field line on a neighboring flux-surface at $r_2 = r_1 + \mathrm{d}r$ is $\mathrm{d}\mathbf{v}_{2,r} \equiv \mathrm{d}r\hat{\mathbf{e}}_\mathbf{r}$ with $P_1(r_2) = P_1(r_1) + \mathrm{d}\mathbf{v}_{2,r}$. The path element of length $\mathrm{d}l_\parallel$ along the magnetic field from

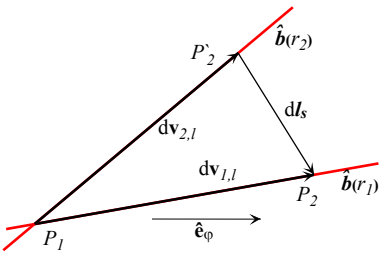

Figure 2.2: Pitched field lines from different flux surfaces. Shown are the parallel path elements that contribute to the measurement of the local shear $\mathrm{d}l_s$.

$P_1(r_2)$ to $P_2(r_2) = P_1(r_2) + \mathrm{d}\mathbf{v}_{2,l}$ is $\mathrm{d}\mathbf{v}_{2,l} = \mathrm{d}l_\parallel(\hat{\mathbf{b}} + \mathrm{d}r\partial_r\hat{\mathbf{b}})$ due to the radially changing field line direction. The radial connection vector from $P_2(r_2)$ to $P_2'(r_1)$ on the flux surface r_1 is $\mathrm{d}\mathbf{v}_{2,-r} \equiv \mathrm{d}r(\hat{\mathbf{e}}_\mathbf{r} + \mathrm{d}l_\parallel\partial_\parallel\hat{\mathbf{e}}_\mathbf{r})$ with $\partial_\parallel = \hat{\mathbf{b}}\cdot\nabla$ due to the radial direction changing along the magnetic field. The measure for the local shear is given by the difference vector between the points $P_2(r_1)$ and $P_2'(r_1)$ (Fig. 2.2):

$$\begin{aligned}\mathrm{d}\mathbf{l}_s &= \mathrm{d}\mathbf{v}_1 - (\mathrm{d}\mathbf{v}_{2,r} + \mathrm{d}\mathbf{v}_{2,l} + \mathrm{d}\mathbf{v}_{2,-r}) \\ &= \mathrm{d}r\mathrm{d}l_\parallel\left(\partial_\parallel\hat{\mathbf{e}}_\mathbf{r} - \partial_r\hat{\mathbf{b}}\right) .\end{aligned} \tag{2.28}$$

The local shear length is thus defined as

$$\begin{aligned}1/L_s &\equiv \hat{\mathbf{e}}_\mathbf{r}\times\hat{\mathbf{b}}\cdot\mathrm{d}\mathbf{l}_s/\mathrm{d}r\mathrm{d}l_\parallel \\ &= \hat{\mathbf{e}}_\mathbf{r}\times\hat{\mathbf{b}}\cdot\left(\partial_\parallel\hat{\mathbf{e}}_\mathbf{r} - \partial_r\hat{\mathbf{b}}\right) ,\end{aligned} \tag{2.29}$$

which corresponds to a radial displacement necessary to have a field line pitch of $\pi/4$. The particle motion in the magnetic field of tokamaks is given by the equation of motion

$$m_s\frac{\mathrm{d}\mathbf{v}}{\mathrm{d}t} = \mathbf{F} + e_s\mathbf{v}\times\mathbf{B}/c\,, \tag{2.30}$$

where $\mathbf{F}$ are any forces acting on the particle other than the Lorenz-force. In strong magnetic fields ($1-10$T in tokamaks) the gyration frequency is very large, $\omega_{ci} = eB/m_i \sim 10^8$/s for protons. Hence, for time scales much larger than $1/\omega_{ci}$ and spatial scales much larger than the gyro radius the lowest order approximation for the particle motion is a gyro ring with a guiding center velocity described by (2.30) [69]. The motion parallel to $\mathbf{B}$ is defined by the parallel component of the equation, $m\mathrm{d}v_\parallel/\mathrm{d}t = F_\parallel$. The perpendicular motion is derived by taking the vector product of $\mathbf{B}$ and Eq. (2.30)

$$\mathbf{v}_D = \frac{c\mathbf{F}\times\mathbf{B}}{e_sB^2} + \frac{cm_s}{e_sB^2}\mathbf{B}\times\frac{\mathrm{d}\mathbf{v}_D}{\mathrm{d}t}\,. \tag{2.31}$$

The second term is the polarization drift $\mathbf{v}_p$ which is usually small ($\sim 1/\omega_{cs}$) and can be approximated by iterating (2.31). The forces that contribute to $\mathbf{F}$ originate from the

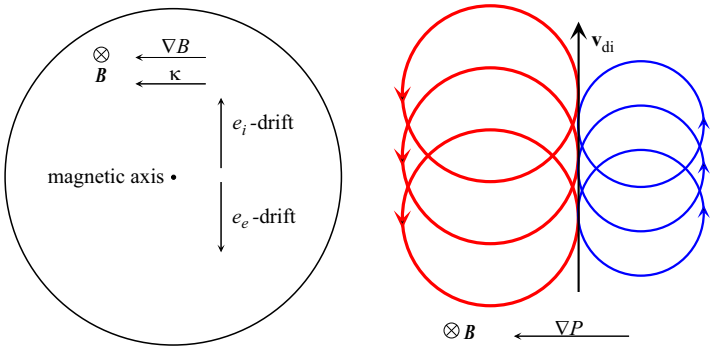

Figure 2.3: (a) Minor cross section of an axisymmetric large aspect ratio confinement device. Due to the charge-dependence of $\mathbf{v}_{\nabla B}$ and $\mathbf{v}_{\boldsymbol{\kappa}}$ the electrons e_e and ions e_i drift in opposite directions. (b) Schematic of the generation of $\mathbf{v}_{di}$ due to a pressure gradient.

electric field $\mathbf{F}_E = e_s\mathbf{E}$, the magnetic moment $\boldsymbol{\mu} = -T\hat{\mathbf{b}}/B$ of the gyrating particle $\mathbf{F}_\mu = \nabla(\boldsymbol{\mu}\cdot\mathbf{B})$ [76], the parallel inertia $\mathbf{F}_i = -m_s\mathrm{d}\mathbf{v}_\parallel/\mathrm{d}t = -m_s v_\parallel(\partial_t\hat{\mathbf{b}} + \mathbf{v}_\perp\cdot\nabla\hat{\mathbf{b}} + v_\parallel\boldsymbol{\kappa})$ and gravitation $\mathbf{F}_g = m_s\mathbf{g}$, which is usually negligible. The resulting drifts of the guiding center are

$$\mathbf{v}_D = \underbrace{\frac{c\mathbf{E}\times\mathbf{B}}{B^2}}_{\equiv\mathbf{v}_E} + \underbrace{\frac{cT\mathbf{B}\times\nabla B}{e_s B^2}}_{\equiv\mathbf{v}_{\nabla B}} + \underbrace{\frac{cT\mathbf{B}\times\boldsymbol{\kappa}}{e_s B^2}}_{\equiv\mathbf{v}_{\boldsymbol{\kappa}}} + \underbrace{\frac{cm_s}{e_s B^2}\mathbf{B}\times\frac{\mathrm{d}\mathbf{v}_D}{\mathrm{d}t}}_{\equiv\mathbf{v}_p}, \tag{2.32}$$

where $\mathbf{v}_E$ is the $\mathbf{E}\times\mathbf{B}$-drift, $\mathbf{v}_{\nabla B}$ the gradient-B drift and $\mathbf{v}_{\boldsymbol{\kappa}}$ the curvature drift, see Fig. 2.3a (the other parallel inertial terms are usually negligible) [69]. The current induced by the drifts is $\mathbf{j}_D = e_s n(\mathbf{v}_D - \mathbf{v}_E)$ and the magnetic moments are accompanied by a plasma magnetization current $\mathbf{j}_\mathbf{M} = c\nabla\times n\boldsymbol{\mu}$. The sum of these currents is

$$\mathbf{j}_D + \mathbf{j}_\mathbf{M} = \underbrace{\frac{c\mathbf{B}\times\nabla p}{B^2}}_{\equiv\mathbf{j}_d} - \frac{4\pi p\mathbf{j}_\parallel}{B^2} + \underbrace{\frac{cnm_s}{B^2}\mathbf{B}\times\frac{\mathrm{d}\mathbf{v}_D}{\mathrm{d}t}}_{\equiv\mathbf{j}_p}, \tag{2.33}$$

where the relation (2.6) and the equilibrium condition $\nabla p = \mathbf{j}\times\mathbf{B}$ were used to eliminate the $\nabla B\times\mathbf{B}$ and $\mathbf{j}_\perp$-terms. The diamagnetic current $\mathbf{j}_d$ is associated with a velocity $\mathbf{v}_{ds} = c\mathbf{B}\times\nabla B/e_s n B^2$. This velocity does not describe a physical drift of guiding centers but originates from the different sizes and/or densities of gyro orbits along ∇p causing a net fluid velocity perpendicular to both pressure gradient and magnetic field (Fig. 2.3b). It is instructive to calculate the divergence of $\mathbf{j}_{ds}$

$$\nabla\cdot\mathbf{j}_{ds} = \nabla\cdot e_s n\left(\mathbf{v}_{\nabla B} + \mathbf{v}_{\boldsymbol{\kappa}}\right) + 4\pi\nabla\cdot\left(p\mathbf{j}_\parallel/cB^2\right) \tag{2.34}$$

since this relates how $\nabla\cdot n\mathbf{v}_{ds}$, which appears in the fluid description of the following section, is connected to physical drifts.

2.2 The Two-fluid Equations

In the case of a strong, almost rigid magnetic confinement the field experienced by a particle changes only little over one gyro period such that $\rho|\nabla B| \ll B$ and $\partial_t B \ll \omega_c B$ with a gyro radius $\rho = \sqrt{2T/m}/eB$ and a gyro frequency $\omega_c = eB/m$ [77]. Hence, the lowest order approximation for a particle trajectory is the drift motion of its gyro center, as the gyro motion itself averages out, where the field particle interaction is evaluated at the gyro center. This removes the fast time scales proportional to ω_c^{-1} from the following plasma description.
The behavior of the confined plasma is described by a reduced set of equations derived from Braginskii's plasma fluid description [78]. The densities n_s, velocities $\mathbf{v}_s$ and temperatures T_s of the two species $s \in \{i, e\}$, electrons and ions, evolve according to the following equations

$$d_t^s n_s + n_s \nabla \cdot \mathbf{v}_s = 0\,, \tag{2.35}$$

$$m_s n_s d_t^s \mathbf{v}_s = -\nabla p_s - \nabla \cdot P_s + e_s n_s \left[\mathbf{E} + \mathbf{v}_s \times \mathbf{B}/c\right] + \mathbf{R}_s\,, \tag{2.36}$$

$$\frac{3}{2} n_s d_t^s T_s + p_s \nabla \cdot \mathbf{v}_s = -\nabla \cdot \mathbf{q}_s - P_s \nabla \mathbf{v}_s + Q_s\,, \tag{2.37}$$

where $e_s, p_s, P_s, \mathbf{R}_s, \mathbf{q}_s, Q_s$ are the respective charges, pressures, stresses, friction forces, heat fluxes and heat sources and $d_t^s = \partial_t + \mathbf{v}_s \cdot \nabla$ the convective time derivative. The focus of the following chapters is on the behavior of ion-temperature-gradient (ITG) driven turbulence where electron temperature fluctuations are neglected. Therefore, explanation of the electron temperature equation and source terms depending on the electron temperature, e.g. Q_e, will be omitted and all terms of the order of $1/\omega_{cs}\tau_s$ neglected.
Assuming ideal gas behavior for the plasma, its pressures are given by $p_s = n_s T_s$. The only retained term of the divergence of the stress is a finite Lamor radius correction $\nabla \cdot P_s = -m_s n_s \mathbf{v}_{ds} \cdot \nabla \mathbf{v}_s \sim O(\omega_{cs}^{-1} \nabla \mathbf{v}_s)$ where $\mathbf{v}_{ds} \equiv c\mathbf{B} \times \nabla p_s / e_s n_s B^2$ is the diamagnetic drift velocity [79, 80, 81, 82]. The friction forces are $\mathbf{R}_e = -\mathbf{R}_i \equiv e n_e j_\parallel \hat{\mathbf{b}}/\sigma_\parallel$ with a parallel conductivity $\sigma_\parallel$. The diffusive contribution to the ion heat flux is $\mathbf{q}_{ih} \equiv -\kappa_i \hat{\mathbf{b}} \nabla_\parallel T_i$ with an ion heat conductivity κ_i. Due to the gyro motion of the particles in the magnetic field there is also a diamagnetic contribution to the heat flux. Figure 2.4 shows the gyro orbits of two ions in a magnetic field with different gyro radii $r_{1,2}$ due to the gradient in temperature. The heat flux through the area $d\Sigma$ by particles gyrating around $x_0 - r_1$ is $\Gamma_1 = -nT_1 v_s$ whereas ions gyrating around $x_0 + r_2$ cause a heat flux of $\Gamma_2 = nT_2 v_2$. With the velocities $v_{1,2} \sim \sqrt{T_{1,2}/m}$ the total diamagnetic heat flux through $d\Sigma$ is $\mathbf{q}_{id} \equiv \Gamma_1 + \Gamma_2 = -5 p_i \hat{\mathbf{b}} \times \nabla T_i / 2 m_i \omega_{ci}$ which is derived by a Taylor expansion of $T(x)$ around x_0. The concrete numerical coefficients for all source terms are derived in a kinetic framework [78].
The cross product of the momentum equation (2.36) with $\mathbf{B}$ yields an equation for the perpendicular drift velocities

$$\mathbf{v}_{s\perp} = \underbrace{c\mathbf{E} \times \mathbf{B}/B^2}_{\equiv \mathbf{v}_E} + \underbrace{c\mathbf{B} \times \nabla p_s / e_s n_s B^2}_{\equiv \mathbf{v}_{ds}} + \underbrace{d_t^s \mathbf{v}_s / \omega_{cs} B}_{\equiv \mathbf{v}_{ps} \sim O(\omega_{cs}^{-1})} + \underbrace{\mathbf{B} \times \nabla \cdot P_s / B^2}_{O(\omega_{cs}^{-1})}\,, \tag{2.38}$$

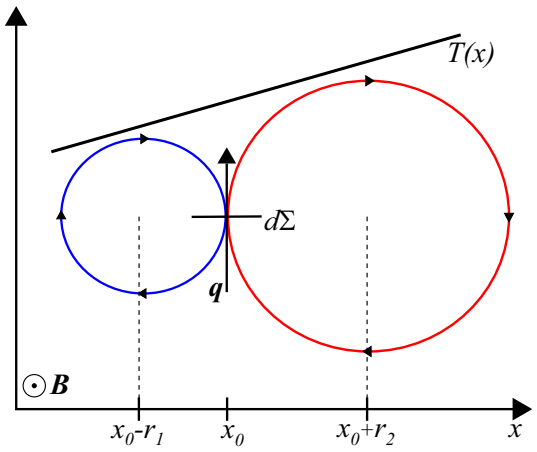

Figure 2.4: Explanation of the diamagnetic heat flux: Particles gyrating around $x_0 - r_1$ and $x_0 + r_2$ are subject to a gradient in temperature which results in a net heat flux through the surface element $d\Sigma$.

where $\mathbf{v}_E$ is the $\mathbf{E} \times \mathbf{B}$ velocity, $\mathbf{v}_{ds}$ the diamagnetic velocity and $\mathbf{v}_{pi}$ the polarization drift which is of higher order in ω_{ci}^{-1} than the first two velocities. Iteration of Eq. (2.38) results in an expression for $\mathbf{v}_{pi}$

$$\mathbf{v}_{pi} = \hat{\mathbf{b}} \times d_t^i \left[c\mathbf{E} \times \mathbf{B}/B^2 + c\mathbf{B} \times \nabla p_i / e_i n_i B^2 \right] / \omega_{ci} - \hat{\mathbf{b}} \times \mathbf{v}_{di} \cdot \nabla \left[\mathbf{v}_E + \mathbf{v}_{di} \right] / \omega_{ci} \,, \quad (2.39)$$

where the last term, originating in $\nabla \cdot P_i$, cancels the diamagnetic convection in d_t^i. Obviously, the main contribution to $\mathbf{v}_{pi}$ comes from the constant part of the magnetic field and Eq. (2.39) can be simplified to

$$\mathbf{v}_{pi} = cD_t \left[\mathbf{E}_\perp - \nabla_\perp p_i / e_i n_i \right] / \omega_{ci} B^2 \,, \quad (2.40)$$

where $D_t \equiv \partial_t + \mathbf{v}_E \cdot \nabla$ is the reduced convective derivative because the $\mathbf{v}_{di} \cdot \nabla$-terms cancel in Eq. (2.39) and parallel gradients are neglected. Since $\omega_{ci}/\omega_{ce} \sim m_e/m_i$ is small the electron polarization drift is negligible and the total velocities for the electrons and ions are

$$\mathbf{v}_i = \mathbf{v}_E + \mathbf{v}_{di} + \mathbf{v}_{pi} + v_{\parallel i} \hat{\mathbf{b}} \quad (2.41)$$

$$\mathbf{v}_e = \mathbf{v}_E + \mathbf{v}_{de} + v_{\parallel e} \hat{\mathbf{b}} \quad (2.42)$$

Assuming quasi-neutrality of the plasma, $n \equiv n_i = n_e$, the difference of the ion and electron continuity equations (2.35) yields

$$\nabla \cdot n \mathbf{v}_{pi} + \nabla \cdot j_\parallel \hat{\mathbf{b}} / \sigma_\parallel e + \nabla \cdot n \left(\mathbf{v}_{di} - \mathbf{v}_{de} \right) = 0 \,, \quad (2.43)$$

where $j_\parallel \equiv en \left(v_{\parallel i} - v_{\parallel e} \right)$. In the case where magnetic field fluctuations are neglected, the

perpendicular electric field is $\mathbf{E}_\perp = -\nabla_\perp \phi$ and inserting (2.40) into equation (2.43) results in the vorticity equation

$$\begin{aligned} &\nabla \cdot ncD_t \left[\nabla_\perp \phi + \nabla_\perp p_i/e_i n\right]/B\omega_{ci} - \nabla \cdot j_\parallel \hat{\mathbf{b}}/\sigma_\parallel e \\ &- \nabla \cdot c\mathbf{B} \times \nabla \left(p_i + p_e\right)/eB^2 = 0\,. \end{aligned} \tag{2.44}$$

An equation for the current $j_\parallel$ can be derived from the component of the electron momentum equation (2.36) parallel to $\hat{\mathbf{b}}$, dropping the small electron inertial term in this case,

$$j_\parallel/\sigma_\parallel = -\nabla_\parallel \left(\phi - p_e/en\right)\,. \tag{2.45}$$

The sum of the components of the ion and electron momentum equations parallel to $\hat{\mathbf{b}}$ on the other hand give an expression for the parallel velocity $v_\parallel$

$$m_i n D_t v_\parallel = -\nabla_\parallel \left(p_i + p_e\right), \tag{2.46}$$

again neglecting the small electron inertia. The convection contribution by the diamagnetic velocity cancels with the finite Lamor radius stress component just as in equation (2.39). The evolution of the density n is given by the electron density equation

$$\partial_t n + \mathbf{v}_E \cdot \nabla n + n\nabla \cdot \left(\mathbf{v}_E + \mathbf{v}_{de} + v_\parallel \hat{\mathbf{b}}\right) - \nabla \cdot j_\parallel \hat{\mathbf{b}}/\sigma_\parallel = 0 \tag{2.47}$$

Inserting the identities $\nabla \cdot cp_i \hat{\mathbf{b}} \times \nabla T_i/eB = -n\mathbf{v}_{di} \cdot \nabla T_i + cp_i \left(\nabla \times \hat{\mathbf{b}}/B\right) \cdot \nabla T_i/e$ and $p_i \nabla \cdot \mathbf{v}_i = -T_i d_t^i n$ and the ion continuity equation (2.35) in (2.37) for the ions results in the ion temperature equation

$$\begin{aligned} &3nD_t T_i/2 - T_i \left[-n\nabla \cdot \left(\mathbf{v}_E + \mathbf{v}_{de} + v_\parallel \hat{\mathbf{b}}\right) + \nabla \cdot j_\parallel \hat{\mathbf{b}}/\sigma_\parallel e\right] \\ &\qquad + 5cp_i \left(\nabla \times \hat{\mathbf{b}}/B\right) \cdot \nabla T_i/2e - \nabla \cdot \kappa_{\parallel i} \hat{\mathbf{b}} \nabla_\parallel T_i = 0 \end{aligned} \tag{2.48}$$

Thus the complete plasma evolution is described by the set of equations (2.44), (2.45), (2.46), (2.47), (2.48) and $p_s = nT_s$.

2.3 The Two-fluid Equations in Toroidal Geometry

The fluid description of the previous section is a subset of the more general two-fluid equations from which the the nonlocal electromagnetic turbulence code (NLET) [64] is derived. This section gives a short overview of the derivation of the dimensionless code equations.

The magnetic geometry is described in a local coordinate system $(\hat{\mathbf{e}}_\mathbf{x}, \hat{\mathbf{e}}_\mathbf{y}, \hat{\mathbf{e}}_\mathbf{z})$ with $\hat{\mathbf{e}}_\mathbf{x} \equiv \nabla\Psi/|\nabla\Psi|$, $\hat{\mathbf{e}}_\mathbf{y} \equiv -\hat{\mathbf{e}}_\varphi$ and $\hat{\mathbf{e}}_\mathbf{z} \equiv \hat{\mathbf{b}}$ on a reference flux surface. Since the field lines curl helically around the flux surface, a displacement along $\hat{\mathbf{b}}$ corresponds to a poloidal one and thus the coordinate in $\hat{\mathbf{e}}_\mathbf{z}$ is the poloidal angle θ. To study the plasma turbulence in a

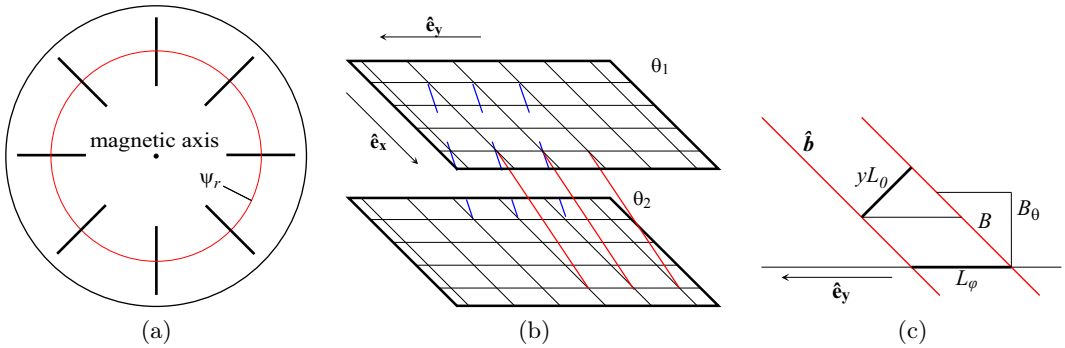

Figure 2.5: (a) Position of the $\hat{\mathbf{e}}_\mathbf{x} \times \hat{\mathbf{e}}_\mathbf{y}$-planes around the reference flux surface Ψ_r. (b) Layout of field lines connecting $\hat{\mathbf{e}}_\mathbf{x} \times \hat{\mathbf{e}}_\mathbf{y}$-planes at different poloidal positions θ. (c) Projection of a perpendicular structure along the field lines onto a $\hat{\mathbf{e}}_\mathbf{x} \times \hat{\mathbf{e}}_\mathbf{y}$-plane which displays the similarity relation $yL_0/L_\varphi = B_\theta/B$.

region around a reference flux surface the domain is represented by multiple planes defined by $\hat{\mathbf{e}}_\mathbf{x} \times \hat{\mathbf{e}}_\mathbf{y}$ at different angles θ (Fig. 2.5) evenly covering one full poloidal rotation. Due to axisymmetry the system is periodic in the $\hat{\mathbf{e}}_\mathbf{y}$-direction. Thus the plasma behavior near the reference flux surface for the entire device is described even though the domain covers only a pie slice of it. The radial coordinate is $x \equiv (\Psi - \Psi_r) / |\nabla \Psi_r| L_0$ with a flux label Ψ_r for the reference surface and a characteristic scale length L_0 perpendicular to $\hat{\mathbf{b}}$. The plasma turbulence phenomena of interest have a large parallel scale length, so it is assumed that a fluctuation on a $\hat{\mathbf{e}}_\mathbf{x} \times \hat{\mathbf{e}}_\mathbf{y}$-plane is the projection of a perpendicular fluctuation along the field lines (Fig. 2.5). A fluctuation of scale L_0 corresponds to one of scale $L_\varphi = L_0 B/B_\theta$ in the toroidal direction and the coordinate is defined by $y \equiv B_\theta L_\varphi / B L_0 = B_\theta \varphi / B L_0$. In these coordinates the average of a quantity W over a flux-surface is simply

$$\langle W \rangle_{y,z} \equiv \iint \mathrm{d}y \mathrm{d}z W \,. \tag{2.49}$$

In this circular geometry the $\hat{\mathbf{e}}_\mathbf{x} \times \hat{\mathbf{e}}_\mathbf{y}$-planes are rectangular and the corresponding gradient is $\nabla_\perp = \partial_x + \partial_y$. The magnetic field and $\hat{\mathbf{e}}_\mathbf{z}$ are parallel only on the reference flux surface. For other radial coordinates the field is $\mathbf{B} \equiv B\,(\hat{\mathbf{e}}_\mathbf{z} - x\hat{\mathbf{e}}_\mathbf{y}/L_s)$ for a local shear length L_s, hence $\hat{\mathbf{b}} \cdot \nabla \equiv \partial_z - x\partial_y/L_s$. The divergences of the drift velocities is always of the form $\nabla \cdot \mathbf{v}_D = \nabla \cdot (\mathbf{B} \times \nabla f / B^2)$ where $f \in \{\phi, p, T_i\}$. Using the relation (2.6), (2.4) and the identities

$$\mathbf{j}_\perp = c\mathbf{B} \times \nabla p / B^2 \tag{2.50}$$

$$\nabla p = B^2 \nabla \beta / 4\pi + \beta B \nabla B / 4\pi \tag{2.51}$$

the operator transforms to

$$\begin{aligned}\nabla\cdot\left(\mathbf{B}\times\nabla f/B^2\right) &\overset{(2.4)}{=} \nabla f\cdot\left[4\pi\mathbf{j}/cB^2 - 2\nabla B\times\mathbf{B}/B^3\right]\\ &\overset{(2.6)}{=} \nabla f\cdot\left[4\pi\mathbf{j}_\parallel/cB^2 - 4\pi\mathbf{j}_\perp/cB^2 - 2\boldsymbol{\kappa}\times\mathbf{B}/B^2\right]\\ &\overset{(2.50)}{=} \nabla f\cdot\left[4\pi\mathbf{j}_\parallel/cB^2 - 4\pi\mathbf{B}\times\nabla p/B^4 - 2\boldsymbol{\kappa}\times\mathbf{B}/B^2\right]\\ &\overset{(2.51)}{=} \nabla f\cdot\left[4\pi\mathbf{j}_\parallel/cB^2 - \mathbf{B}\times\left(\nabla\beta/2+\beta\nabla\ln B - 2\boldsymbol{\kappa}\right)/B^2\right]\\ &\approx \hat{C}f \quad \text{with} \quad \hat{C}\equiv 2\mathbf{B}/B^2\times\boldsymbol{\kappa}\cdot\nabla \end{aligned} \tag{2.52}$$

in the limit of $\beta, \nabla\beta \to 0$ and negligible parallel gradient. The curvature in the large aspect-ratio limit is just the curvature of the toroidal field

$$\boldsymbol{\kappa} = -\hat{\mathbf{e}}_\mathbf{R}/R = \left(\cos\left(2\pi z\right)\hat{\mathbf{e}}_\mathbf{x} - \sin\left(2\pi z\right)\hat{\mathbf{e}}_\mathbf{y}\right)/R\,. \tag{2.53}$$

Assuming that $x_{\max}/L_s \ll 1$, the curvature operator [83] takes the form

$$\hat{C} \equiv \frac{2}{RB}\left(\cos\left(2\pi z\right)\partial_y + \sin\left(2\pi z\right)\partial_x\right)\,. \tag{2.54}$$

To obtain local dimensionless equations the following renormalization of the fluctuation quantities $n, \phi, T_i, v_\parallel$ is made [64, 74]

$$\begin{aligned} &n \equiv n^p\lambda/n_{e0} && T_i \equiv T_i^p\lambda/T_{i0} && \phi \equiv \phi^p ct_0/BL_0^2\\ &v_\parallel \equiv v_\parallel^p\lambda/c_s && J \equiv j_\parallel^p L_z\eta_\parallel ct_0/BL_0^2 && v_{de} \equiv T_{e0}/eBL_0\\ &p_i = n + T_i && p_e = n && p = \left(p_e+\tau p_i\right)/\left(1+\tau\right)\,, \end{aligned} \tag{2.55}$$

where the superscript p denotes a quantity in physical units and the subscript 0 the background value at the reference flux surface. The time, space and velocity scales are given by

$$\begin{aligned} &t_0 \equiv \sqrt{RL_n/2}/c_s && L_0 \equiv 2\pi q\sqrt{n_{e0}e^2\eta_\parallel\rho_s R/m_i\omega_{ci}}\sqrt[4]{2R/L_n} && L_z \equiv 2\pi qR\\ &c_s \equiv \sqrt{\left(T_{e0}+T_{i0}\right)/m_i} && \rho_s \equiv c_s/\omega_{ci} \end{aligned} \tag{2.56}$$

with the dimensionless parameters

$$v_{de}t_0/L_0 \equiv \alpha \qquad \epsilon_n \equiv 2L_n/R \qquad \epsilon_v \equiv c_s t_0/L_z \qquad \tau \equiv T_{i0}/T_{e0} \qquad \lambda \equiv L_n/L_0\,. \tag{2.57}$$

To illustrate how the individual terms of the fluid description transform into the dimensionless ones for the fluctuations, the following equations consist of one original fluid equation in physical units above and the dimensionless equation below where the corresponding terms are indicated by arrows. The dimensionless form of the current equation (2.45) is

$$\begin{aligned} -\nabla_\parallel\left(\phi - p_e/en\right) &= j_\parallel/\sigma_\parallel\\ \downarrow \qquad &\downarrow\\ -\nabla_\parallel\left(\phi - \alpha p_e\right) &= J\,. \end{aligned} \tag{2.58}$$

The vorticity equation (2.44) transforms into

$$\begin{array}{lllll} \nabla_\perp \cdot ncD_t \left[\nabla_\perp \phi + \nabla_\perp p_i/e_i n\right]/B\omega_{ci} & -\nabla\cdot(\mathbf{v}_{di}+\mathbf{v}_{de}) & -\nabla\cdot j_\parallel \hat{\mathbf{b}}/\sigma_\parallel e & = 0 \\ \downarrow & \downarrow & \downarrow & \\ \nabla_\perp \cdot d_t \nabla_\perp (\phi + \tau\alpha p_i) & + \quad \hat{C}p & - \quad \nabla_\parallel J & = 0\,, \end{array} \tag{2.59}$$

and the dimensionless density equation derived from (2.47) is

$$\begin{array}{llll} \partial_t n + \mathbf{v}_E\cdot\nabla n & +n\nabla\cdot(\mathbf{v}_E+\mathbf{v}_{de}) & +n\nabla\cdot v_\parallel \hat{\mathbf{b}} & -\nabla\cdot j_\parallel\hat{\mathbf{b}}/\sigma_\parallel & = 0 \\ \downarrow & \downarrow & \downarrow & \downarrow & \\ d_t n + \partial_y\phi & -\epsilon_n \hat{C}(\phi - \alpha p_e) & +\epsilon_v \nabla_\parallel v_\parallel & -\alpha\epsilon_n(1+\tau)\nabla_\parallel J & = 0\,. \end{array} \tag{2.60}$$

The origin of the term $\partial_y\phi$ is the convection of the linear background gradient with the drift velocity fluctuations retained during the partial linearization. For better readability the transformation of the temperature equation (2.48) is separated into two equations where C is just a variable coupling the equation set. The curvature part of the temperature equation is

$$\begin{array}{lll} T_i n\nabla\cdot(\mathbf{v}_E+\mathbf{v}_{de})+ & 5cp_i\left(\nabla\times\hat{\mathbf{b}}/B\right)\cdot\nabla T_i/2e - C & = 0 \\ \downarrow & \downarrow & \\ -\epsilon_n\hat{C}(\phi-\alpha p_e)- & 5\alpha\tau\epsilon_n\hat{C}T_i/2 - C & = 0\,, \end{array} \tag{2.61}$$

and the time-evolution is described by

$$\begin{array}{llll} 3nD_tT_i/2+ & T_i n\nabla\cdot v_\parallel\hat{\mathbf{b}}- & T_i\nabla\cdot j_\parallel\hat{\mathbf{b}}/\sigma_\parallel e- & \nabla\cdot\kappa_{\parallel i}\hat{\mathbf{b}}\nabla_\parallel T_i + C = 0 \\ \downarrow & \downarrow & \downarrow & \downarrow \\ 3\left(d_tT_i + \eta_i\partial_y\phi\right)/2+ & \epsilon_v\nabla_\parallel v_\parallel - & \alpha\epsilon_n(1+\tau)\nabla_\parallel J- & \kappa_i\Delta_\parallel T_i + C = 0\,. \end{array} \tag{2.62}$$

Therefore, the set of equations describing the ITG-turbulence is:

$$-\nabla_\parallel(\phi-\alpha p_e) = J \tag{2.63}$$

$$\nabla_\perp\cdot d_t\nabla_\perp(\phi+\tau\alpha p_i) + \hat{C}p - \nabla_\parallel J = 0 \tag{2.64}$$

$$d_t n + \partial_y\phi - \left[\epsilon_n\hat{C}(\phi-\alpha p_e) - \epsilon_v\nabla_\parallel v_\parallel + \alpha\epsilon_n(1+\tau)\nabla_\parallel J\right] = 0 \tag{2.65}$$

$$d_tT_i + \eta_i\partial_y\phi - \frac{2}{3}\left[\epsilon_n\hat{C}(\phi-\alpha p_e+5\alpha\tau T_i/2) - \epsilon_v\nabla_\parallel v_\parallel + \alpha\epsilon_n(1+\tau)\nabla_\parallel J\right]$$
$$-2\kappa_i\Delta_\parallel T_i/3 = 0 \tag{2.66}$$

$$d_t v_\parallel + \epsilon_v\nabla_\parallel p = 0 \tag{2.67}$$

with the adiabaticity relation

$$\alpha n = \phi - \langle\phi\rangle_{y,z} \tag{2.68}$$

where $\langle \ldots \rangle_{y,z}$ is the flux surface average. It is easily verified that these equations are invariant under the transformation Λ:

$$\left.\begin{array}{l} x, y, z \\ n, \phi, T_i, v_\parallel \end{array}\right\} \stackrel{\Lambda}{\rightarrow} \left\{\begin{array}{l} -x, y, -z \\ -n, -\phi, -T_i, v_\parallel \end{array}\right. \tag{2.69}$$

Chapter 3

Instabilities

This chapter gives an overview of the ion-temperature-gradient (ITG) driven instability, which generates the turbulence necessary for the ZF formation. To point out the differences of the ITG-ZF system to the often used drift-wave (DW) driven ZF description the DW instability, which can be considered a base-type model for gradient-driven turbulence, is additionally discussed. The dimensionless units used in the NLET-code are used for all figures (Sec. 2.3).

3.1 Drift-Wave Instability

To illustrate the mechanism of the DW instability the behavior of the electric potential and the plasma density in a simple homogenous magnetic field configuration with negligible ion temperature and parallel velocity ($\tau = 0, \epsilon_v = 0$) is examined (a more extensive review is given by [84, 13]). In the case of an infinite parallel conductivity a local fluctuation of the electric potential would immediately be balanced by a parallel current, thus inhibiting the growth of such fluctuations entirely. A finite conductivity, on the other hand, allows for temporary local potential perturbations which are linked to density fluctuations. The accompanying electric field then results in an $\mathbf{E}\times\mathbf{B}$-drift around the local fluctuation (Fig. 3.1). The flow-vortex taps into the density gradient and extends the original fluctuation on the side where the $\mathbf{E}\times\mathbf{B}$-drift is anti-parallel to ∇n whereas on the other side the fluctuation is reduced. This leads to a density pattern traveling perpendicular to ∇n and $\mathbf{B}$, a resistive drift-wave. The growth and damping of a DW is determined by the phase relation of the density and potential perturbations.

The equation system describing the DWs consists of the linearized vorticity and density equations (2.64) and (2.65) where the current is eliminated by (2.63) and σ is a dimensionless parallel conductivity

$$\partial_t \Delta_\perp \phi + \Delta_\parallel (\phi - \alpha n)\, \sigma = 0 \tag{3.1}$$

$$\partial_t n + \partial_y \phi + \alpha \epsilon_n \Delta_\parallel (\phi - \alpha n)\, \sigma = 0\,. \tag{3.2}$$

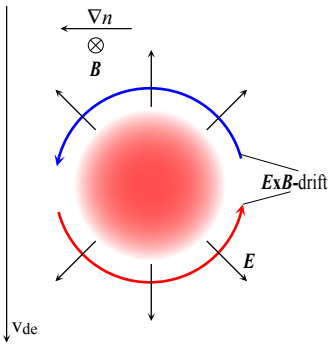

Figure 3.1: Local charge density fluctuation in a homogeneous magnetic field. The induced $\mathbf{E} \times \mathbf{B}$-drift vortex results in an accumulation of density in v_{de}-direction and a reduction in the opposite direction resulting in a motion of the fluctuation in the v_{de}-direction .

Hence, the dispersion relation for the DWs is

$$\omega_{\pm} = \frac{1}{2k_{\perp}^2}\left[-\imath k_{\parallel}^2\left(1+\alpha^2\epsilon_n k_{\perp}^2\right)\sigma \pm \sqrt{4\imath\alpha k_{\parallel}^2 k_y k_{\perp}^2\sigma - k_{\parallel}^2\sigma^2\left(1+\alpha^2\epsilon_n k_{\perp}^2\right)}\right] \tag{3.3}$$

and an expansion in the limit $1/\sigma \to 0$ for the growing branch yields

$$\omega_{+} = \frac{\alpha k_y}{1+\alpha^2\epsilon_n k_{\perp}^2} + \imath\frac{\alpha^2 k_y^2 k_{\perp}^2}{k_{\parallel}^2\left(1+\alpha^2\epsilon_n k_{\perp}^2\right)^3}\frac{1}{\sigma}\,. \tag{3.4}$$

This reflects that a finite conductivity is necessary for an instability. The corresponding group and phase velocities of the DW are

$$v_{gy} = \frac{\alpha}{1+\alpha^2\epsilon_n k_{\perp}^2} - \frac{2\alpha^3\epsilon_n k_y^2}{\left(1+\alpha^2\epsilon_n k_{\perp}^2\right)^2} \tag{3.5}$$

$$v_{py} = \frac{\alpha}{1+\alpha^2\epsilon_n k_{\perp}^2}\frac{k_y^2}{k_{\perp}^2} \tag{3.6}$$

$$v_{gx} = -\frac{2\alpha^3\epsilon_n k_x k_y}{\left(1+\alpha^2\epsilon_n k_{\perp}^2\right)^2} \tag{3.7}$$

$$v_{px} = \frac{\alpha k_y}{1+\alpha^2\epsilon_n k_{\perp}^2}\frac{k_x}{k_{\perp}^2} \tag{3.8}$$

and (3.6) shows that DWs propagate in the electron diamagnetic drift direction (since $v_{de}t_0/L_0 = \alpha$), hence the name DW.
Analysis of DWs in a curved magnetic field with shear yielded that resistive DWs are stabilized by the shear [85] and that a finite conductivity even enhances the shear-stabilization [86]. This somewhat confounds ZF theories for toroidal geometries that are based on this instability alone to generate the turbulence. General linear instability with magnetic shear requires at least a coupling of the DWs to another mode e.g. Shear–Alfvén waves [87, 88], in other words non-adiabaticity.

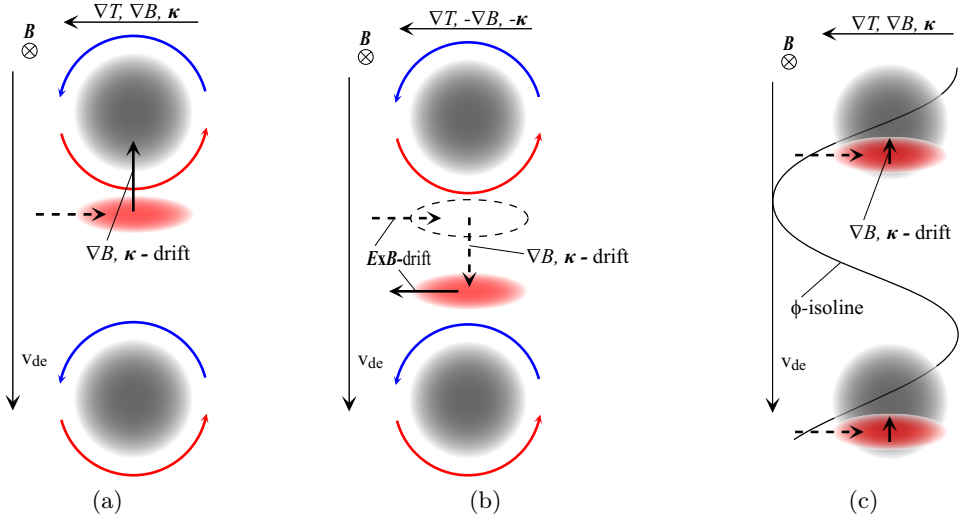

Figure 3.2: **(a)** $\mathbf{E} \times \mathbf{B}$-vortex around initial density perturbation convects plasma from high temperature regions down the temperature gradient which subsequently drifts towards the initial fluctuation resulting in an instability. **(b)** Scenario similar to previous case but with opposite magnetic inhomogeneity drifts leading away from the initial perturbation thus yielding to instability. **(c)** Phase shift between initial density and potential fluctuation leads to a growing instability which is enhanced by the magnetic inhomogeneity drift of convected high temperature plasma.

3.2 Ion-Temperature-Gradient Instability

As discussed in the previous section, a potential perturbation in a magnetized plasma excites an $\mathbf{E} \times \mathbf{B}$-drift vortex around itself. This vortex convects temperature if the perturbation is localized on a temperature gradient (Fig. 3.2a) similar to the density convection in the DW case. In a magnetic field with a field gradient or curvature the corresponding magnetic inhomogeneity drifts (2.31) of the hot plasma, convected to a region of lower temperature by the $\mathbf{E} \times \mathbf{B}$-vortex, are slightly higher than the drifts of the background due to the temperature dependence of $\mathbf{v}_{\nabla B}$ and $\mathbf{v}_{\boldsymbol{\kappa}}$. Thus the hot particles drift towards the density perturbation associated with the initial potential fluctuation if the magnetic inhomogeneity drift is in the ion-diamagnetic drift direction, which leads to an instability, the ITG-instability [20].
For a magnetic inhomogeneity drift in the electron-diamagnetic drift direction the hot plasma would be convected away from the initial fluctuation. In case of an initial periodic fluctuation, the hot plasma would be convected up along the temperature gradient again by the $\mathbf{E} \times \mathbf{B}$-vortex of the "neighboring" fluctuation or cooled by plasma convected from a region of lower temperature (Fig. 3.2b). Thus the convection of temperature does not lead to an instability when the temperature gradient is anti-parallel to the magnetic field gradient and curvature.
If there is also a density gradient besides the temperature gradient the resulting drift-wave type propagation of the fluctuation is slowed by the hot plasma convected by the magnetic-

inhomogeneity drift in the opposite direction for small temperature gradients. For a critical gradient an equilibrium negating the propagation can be reached. But a sufficiently large temperature gradient leads again to a propagating instability.
A phase difference between the density and potential fluctuations (caused by e.g. finite parallel conductivity, landau damping) enhances the instability further (Fig. 3.2c). This curvature driven mode is called the ITG-mode (extensively discussed in [89, 90, 91, 74]).
In the following paragraph the dispersion relation for the ITG-instability is derived from the linearized version of the equations (2.63)-(2.67). Inserting (2.64) into the density equation (2.65) yields

$$\partial_t n + \partial_y \phi - \left[\epsilon_n \hat{C}\left(\phi + \tau\alpha p_i\right) - \epsilon_v \nabla_\parallel v_\parallel + \alpha\epsilon_n\left(1+\tau\right)\partial_t \Delta_\perp\left(\phi + \tau\alpha p_i\right)\right] = 0\,. \tag{3.9}$$

Subtracting the density equation times 2/3 from the temperature equation (2.66) leads to

$$\partial_t T_i + \eta_i \partial_y T_i - \frac{2}{3}\left[5\tau\alpha\epsilon_n \hat{C} T_i/2 + \partial_t n + \partial_y \phi\right] = 0\,. \tag{3.10}$$

With the ansatz $n, T_i, \phi, v_\parallel \sim e^{\imath(k_x x + k_y y - \omega t)}$ one obtains, after elimination of $v_\parallel$ using Eq. (2.67),

$$\omega^2 n - \omega k_y \phi + \omega\omega_{\boldsymbol{\kappa}}\left(\phi + \tau\alpha p_i\right) + \epsilon_v^2 \Delta_\parallel p + \alpha\epsilon_n\left(1+\tau\right)\omega^2 k_\perp^2\left(\phi + \tau\alpha p_i\right) = 0 \tag{3.11}$$

and

$$\omega T_i - k_y\left(\eta_i - 2/3\right)\phi + 5\alpha\tau\omega_{\boldsymbol{\kappa}} T_i/3 - 2\omega n/3 = 0\,, \tag{3.12}$$

where $\omega_{\boldsymbol{\kappa}} \equiv \epsilon_n\left(\cos(2\pi z)k_y + \sin(2\pi z)k_x\right)$ is the curvature frequency. The potential can be eliminated with the adiabaticity relation $\phi = \alpha n$ (assuming the flux-surface-average $\langle\phi\rangle_{y,z} = 0$) and (3.11) transforms into

$$\begin{aligned}\omega\left(\omega - \alpha k_y\right) n + \omega\omega_{\boldsymbol{\kappa}}\alpha\left(n + \tau p_i\right) + \epsilon_v^2 \Delta_\parallel\left(n + \tau p_i\right)/\left(1+\tau\right) \\ + \alpha^2\epsilon_n\left(1+\tau\right)\omega^2 k_\perp^2\left(n + \tau p_i\right) = 0\end{aligned} \tag{3.13}$$

Expanding the first term by

$$\left(\omega + 5\alpha\tau\omega_{\boldsymbol{\kappa}}/3\right)/\left(2\omega/3 + \alpha k_y\left(\eta_i - 2/3\right)\right) + \tau \tag{3.14}$$

and eliminating the new $\omega\left(\omega - \alpha k_y\right)\tau n$-term with (3.12) yields the relation [92]

$$\begin{aligned}\Bigg[&\frac{\omega\left(\omega + 5\alpha\tau\omega_{\boldsymbol{\kappa}}/3\right)\left(\omega - \alpha k_y\right)}{\omega\left(1 + 5\tau/3\right) + 5\alpha\tau\omega_{\boldsymbol{\kappa}}\left(1+\tau\right)/3 + \alpha\tau k_y\left(\eta_i - 2/3\right)} + \omega\omega_{\boldsymbol{\kappa}}\alpha \\ &+ \alpha^2\epsilon_n\left(1+\tau\right)\omega^2 k_\perp^2 + \frac{\epsilon_v^2}{1+\tau}\Delta_\parallel\Bigg]\left(n + \tau p_i\right) = 0\,,\end{aligned} \tag{3.15}$$

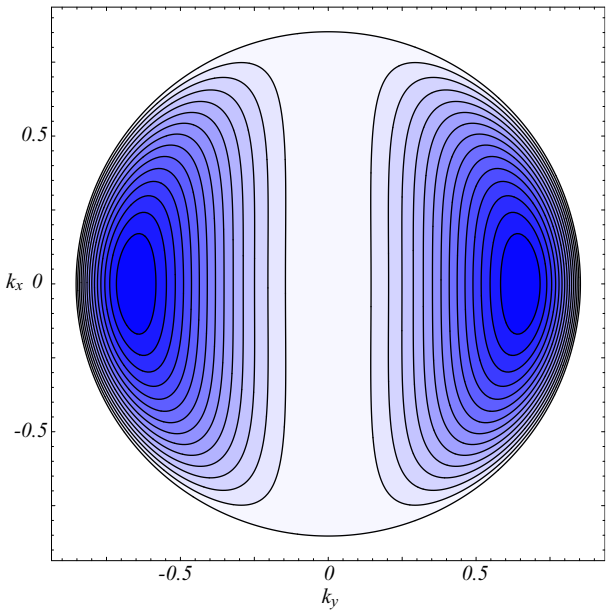

Figure 3.3: Contour plot of the radicand $b^2 - 4ac < 0$ for parameter values $\alpha = 0.5, \epsilon_n = 1, \tau = 1, \eta_i = 2.4$. Color code white denotes no growth whereas the regions of growth are shaded in blue.

where the $\Delta_\parallel$-term describes the coupling of the ITG-mode with the sound-wave. If this coupling is neglected different locations along the magnetic field do not interact and the eigenmodes are localized with a dispersion relation for $\omega \neq 0$

$$\begin{aligned}
&\omega^2 \underbrace{\left[1 + \alpha^2 \epsilon_n (1+\tau) \left(1 + \frac{5}{3}\tau\right) k_\perp^2\right]}_{\equiv a} - \\
&\underbrace{\omega \left[\alpha k_y - \alpha \omega_{\boldsymbol{\kappa}} \left(1 + \frac{10}{3}\tau\right) - \alpha^2 \epsilon_n (1+\tau) k_\perp^2 \left(\frac{5}{3}\alpha\tau\omega_{\boldsymbol{\kappa}} (1+\tau) + \alpha\tau k_y \left(\eta_i - \frac{2}{3}\right)\right)\right]}_{\equiv -b} + \\
&\underbrace{\alpha\omega_{\boldsymbol{\kappa}} \left[\frac{5}{3}\tau\alpha\omega_{\boldsymbol{\kappa}} [1+\tau] + \tau\alpha k_y \left(\eta_i - \frac{7}{3}\right)\right]}_{\equiv c} = 0\,,
\end{aligned} \tag{3.16}$$

which has the obvious solutions $\omega_\pm = (-b \pm \sqrt{b^2 - 4ac})/2a$. The condition for growth is a negative radicand $b^2 - 4ac < 0$. In cases of a negligible polarization-drift contribution $\alpha^2 \epsilon_n (1+\tau) k_\perp^2 \to 0$ on obtains a condition for η_i for ITG growth on the outside of the torus, where $\omega_{\boldsymbol{\kappa}} = \epsilon_n k_y$,

$$\eta_i > \frac{2}{3} + \frac{(\epsilon_n - 1)^2}{4\epsilon_n \tau} + \frac{10\epsilon_n \tau}{9}\,. \tag{3.17}$$

For the parameter set $\alpha = 0.5, \epsilon_n = 1, \tau = 1, \eta_i = 2.4$, which will be mostly used for the ZF studies in the following chapters, the region of growth is shown in figure (3.3). The mode

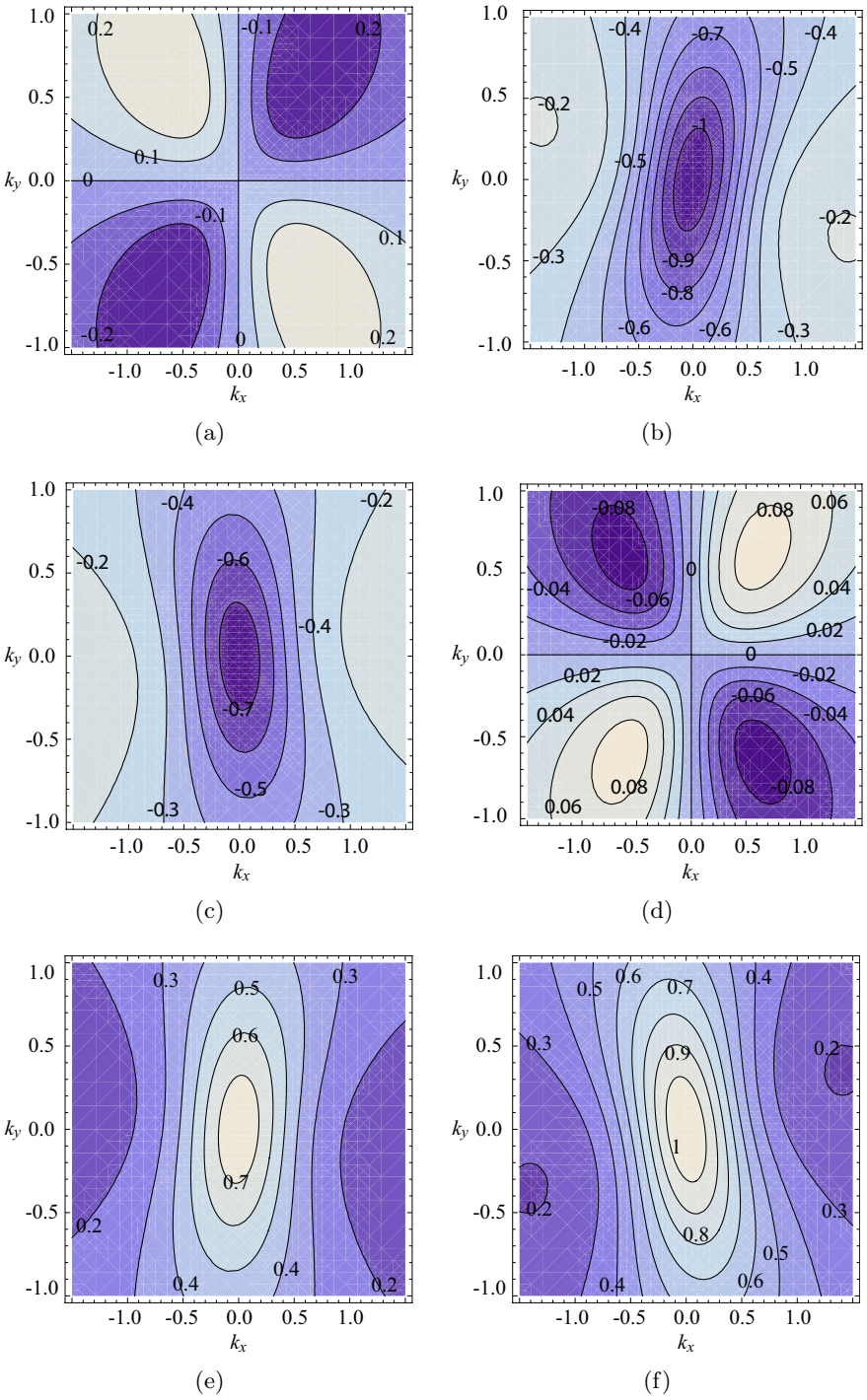

Figure 3.4: Contour plot of the perpendicular wave-number dependence of the radial group velocity v_{gx} for the ITG instability at the inside $\omega_{\boldsymbol{\kappa}} = -\epsilon_n k_y$ **(a)**, top side $\omega_{\boldsymbol{\kappa}} = \epsilon_n k_x$ **(b)**, top-outside $\omega_{\boldsymbol{\kappa}} = \epsilon_n \left(k_x + ky\right)/\sqrt{2}$ **(c)**, outside $\omega_{\boldsymbol{\kappa}} = \epsilon_n k_y$ **(d)**, bottom-outside $\omega_{\boldsymbol{\kappa}} = \epsilon_n \left(-kx + ky\right)/\sqrt{2}$ **(e)** and bottom side $\omega_{\boldsymbol{\kappa}} = -\epsilon_n k_x$ **(f)**.

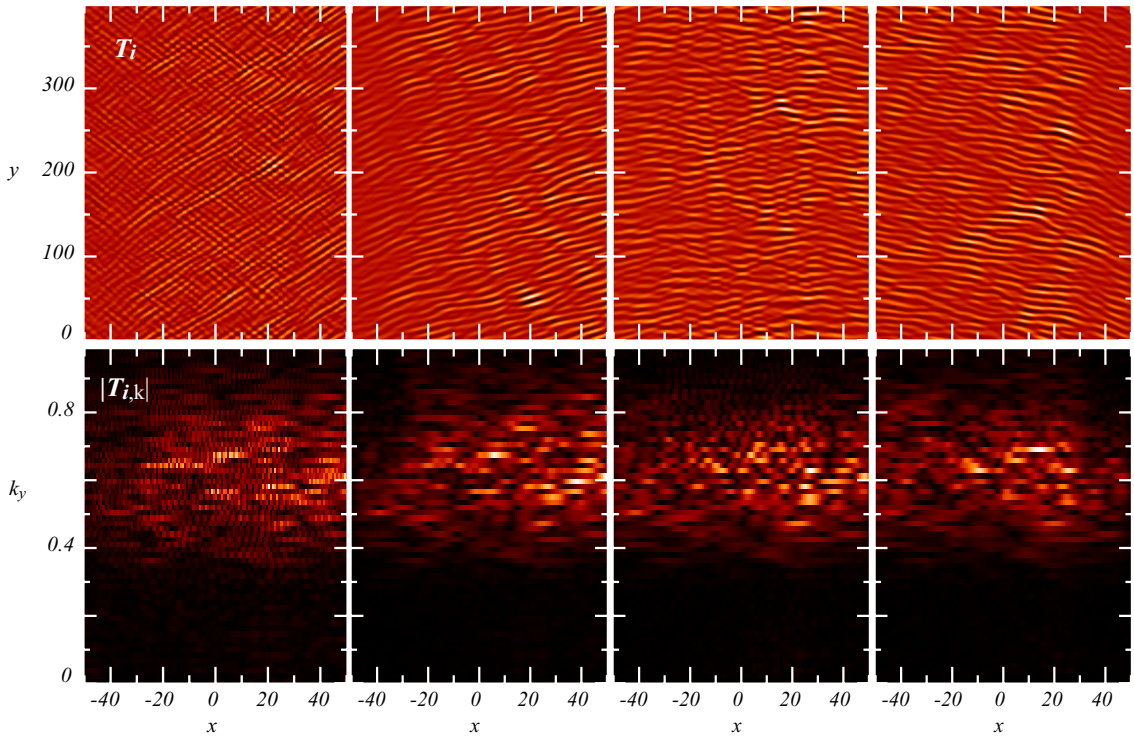

Figure 3.5: Snapshots of the temperature fluctuations (top row) and k_y-spectra (bottom row) of a growing ITG instability with artificially suppressed ZFs at **(a)** high-field side, **(b)** top side, **(c)** low-field side and bottom side **(d)**.

with the maximal growth rate is $k_x = 0, k_y = \frac{1}{19}\left(\frac{2}{3}\left(35 + \sqrt{39130}\right)\right)^{1/2} \approx 0.656$. However, due to the here neglected coupling along the field lines small deviations may be observed in the simulations.
Due to the dependence on the curvature frequency $\omega_{\boldsymbol{\kappa}}$ of the dispersion relation (3.16) the radial group velocity v_{gx} changes with the poloidal coordinate z. Figure 3.4 shows the changes in symmetry for different poloidal positions of the group velocity with respect to the perpendicular wave-numbers. This is pointed out here as the symmetry of v_{gx} plays a major role in analytical estimates of ZFs discussed in chapter 5.
Figure 3.5 shows snapshots of a growing ITG instability during the linear phase in a turbulence study with the parameters

$$L_x = 100 \quad L_y = 400 \quad \alpha = 0.5 \quad \epsilon_n = 1 \quad \tau = 1 \quad s = 1 \quad q = 1.5 \quad \eta_i = 2.4\,. \tag{3.18}$$

The dominant mode numbers on the outboard-midplane (low-field side, Fig. 3.5c) are within range of the analytical expectations (Fig. 3.3). The relative slant of the modes on the top and bottom side (Figs. 3.5b, 3.5d) compared the the structure on the outboard-midplane illustrates how the magnetic shear influences parallel extended modes.

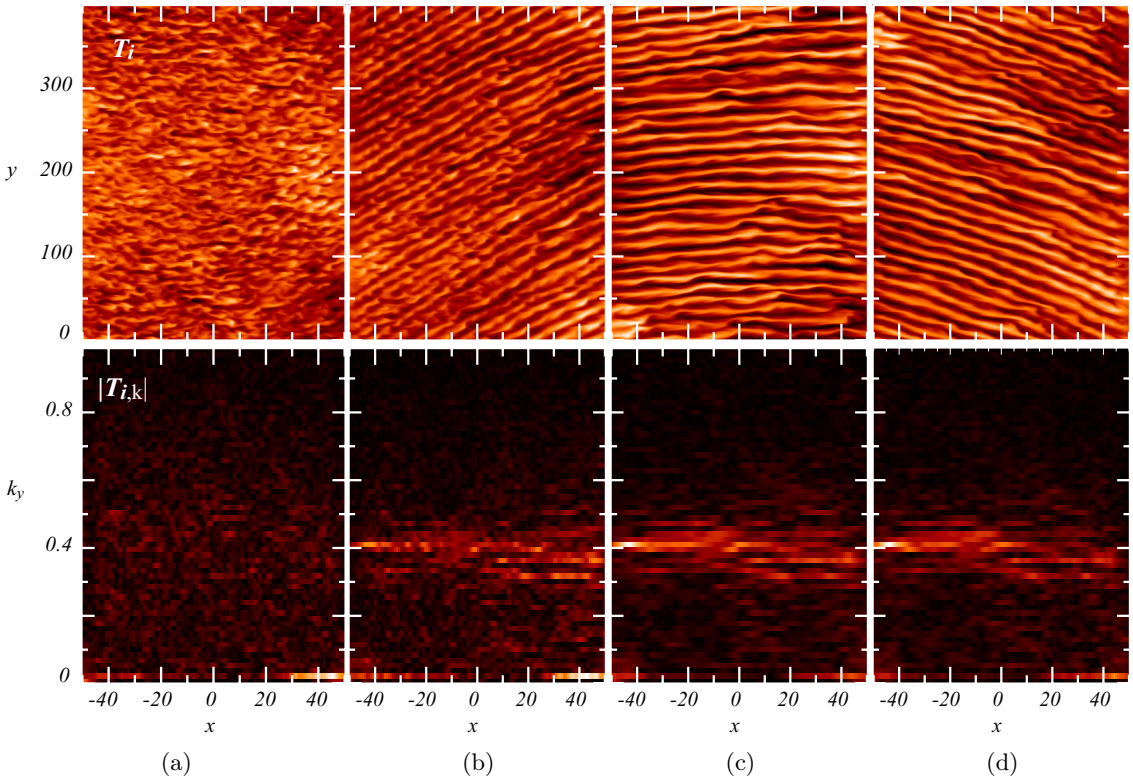

Figure 3.6: Snapshots of the temperature fluctuations (top row) and k_y-spectra (bottom row) of a fully developed ITG-turbulence with artificially suppressed ZFs at the **(a)** high-field side, **(b)** top side, **(c)** low-field side and bottom side **(d)**.

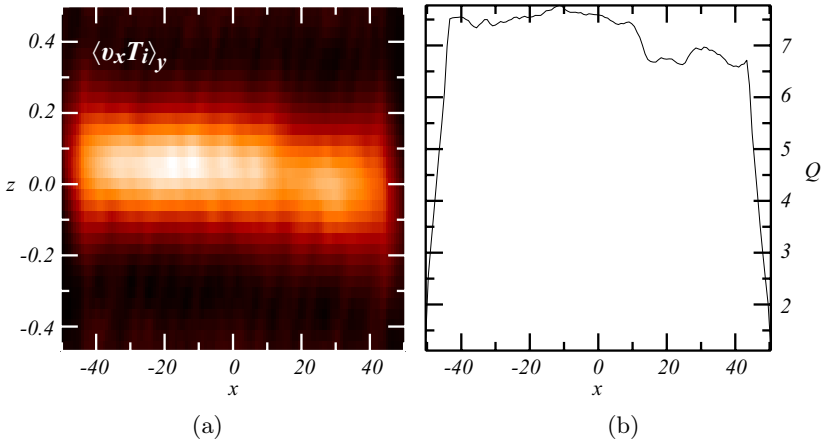

Figure 3.7: **(a)** Radial heat-flux averaged over y of the ITG-turbulence shown in figure 3.6. **(b)** Flux-surface-averaged radial heat-flux Q.

The ITG-instability is prone to a secondary instability that leads to a nonlinear saturation in a state of radial streamers with $k_x \approx 0$ and $k_y \approx 0.4$ (Fig. 3.6) [42, 93, 94]. Even though this turbulent pattern may, at first glance, appear to be similar to a $k_x = 0$ linear mode, just with a different wave-number k_y, it is a state of strong turbulence [63] and the linear dispersion relation is therefore no applicable. As will be shown in Chap. 4, the nonlinear state with streamers (Fig. 3.6c) is the initial state from which the ZFs grow [95, 40]. The streamers appear to have Kelvin-Helmholtz like corrugations due to small velocity fluctuations in the y-direction. Together with the radial velocity fluctuations the turbulence anisotropy amounts to a perpendicular Reynolds stress which drives ZFs (see Chap. 4).
Figure 3.7 shows the distribution of the radial heat-flux caused by the streamers which indicates that the turbulence is located primarily on the low-field side around $z = 0$. The radial distribution of the flux-surface averaged heat-flux $Q \equiv \langle v_x T_i \rangle_{y,z}$ is almost constant but at a rather high level compared to self-consistent cases where ZFs are not suppressed (the steep drops in Q at the domain edges are artificial due to fixed gradients at the edges and the drop inside is due to an unstable large scale k_y-mode caused by the boundaries in this case).

3.3 Small-scale Large-scale Interaction

Since the scale length along the magnetic field is rather long compared to the perpendicular scale, it is instructive to compare the behavior of the plasma turbulence with results from 2D Navier-Stokes (NS) turbulence theories to gain an insight into the inverse energy transfer mechanism. The following excerpt of [65] describes the excitation of large scale structures from small scale turbulence.
The 2D-NS equation for the vorticity ω is

$$\partial_t \omega + \mathbf{v} \cdot \nabla \omega = \nu \Delta \omega \tag{3.19}$$

with a kinematic viscosity ν. This equation also describes the propagation of DWs if one interprets $(1 - \Delta_\perp)\phi$, or in case of ZFs $-\Delta_\perp \phi$, as a vorticity. Thus, the results obtained in the following are also relevant for ZFs. Assuming the large scales K are separated from the small scales k by a large spectral gap $[K_L, k_s]$, hence $K \leq K_L \ll k_s \leq k$, the respective contributions to vorticity and velocity are

$$\omega = \int_{-\infty}^{K_L} \mathrm{d}K^2 \omega_L(\mathbf{K}, t)\, e^{\imath \mathbf{K}\cdot\mathbf{x}} + \int_{k_s}^{\infty} \mathrm{d}k^2 \omega_s(\mathbf{k}, t)\, e^{\imath \mathbf{k}\cdot\mathbf{x}} \tag{3.20}$$

$$\mathbf{v} = \int_{-\infty}^{K_L} \mathrm{d}K^2 \mathbf{v}_L(\mathbf{K}, t)\, e^{\imath \mathbf{K}\cdot\mathbf{x}} + \int_{k_s}^{\infty} \mathrm{d}k^2 \mathbf{v}_s(\mathbf{k}, t)\, e^{\imath \mathbf{k}\cdot\mathbf{x}} \tag{3.21}$$

$$\mathbf{v}_L = \imath \mathbf{K} \times \hat{\mathbf{e}}_\mathbf{z} \omega_L / K^2 \tag{3.22}$$

$$\mathbf{v}_s = \imath \mathbf{k} \times \hat{\mathbf{e}}_\mathbf{z} \omega_s / k^2 \,. \tag{3.23}$$

After linearization in ω_s the time-evolution for small scale fluctuations is defined by

$$\partial_t \omega_s = -\nu k^2 \omega_s - \int \mathrm{d}Q^2 \left[\frac{1}{(\mathbf{k}-\mathbf{Q})^2} - \frac{1}{\mathbf{Q}^2}\right] \mathbf{k}\cdot\mathbf{Q} \times \hat{\mathbf{e}}_\mathbf{z} \omega_L(\mathbf{Q})\, \omega_s(\mathbf{k}-\mathbf{Q}) \;, \tag{3.24}$$

where capital letters $(\mathbf{K}, \mathbf{Q})$ are wave vectors of the large scales and lower cases $(\mathbf{k}, \mathbf{q})$ those of small scales. The magnitude relation between the first term on the right-hand-side (RHS) of the equation and the other ones is $1 : 1/kK\nu$ suggesting a perturbative treatment of the convective terms. Assuming, for simplicity, a generation of initial turbulence from a white noise source $f_s(\mathbf{k}, t)$ with a vanishing average $\langle f_s(\mathbf{k}, t)\rangle = 0$ and a correlation $\langle f_s(\mathbf{k}_1, t_1) f_s(\mathbf{k}_2, t_2)\rangle = \langle |f_s(\mathbf{k}_1)|^2\rangle \delta(\mathbf{k}_1 + \mathbf{k}_2)\delta(t_1 - t_2)$, the lowest order in $\omega_s = \omega_s^{(0)} + \omega_s^{(1)} + \ldots$ of (3.24) is

$$\left(\partial_t + \nu k^2\right) \omega_s^{(0)} = f_s(\mathbf{k}, t) \tag{3.25}$$

which has the solution

$$\omega_s^{(0)}(\mathbf{k}, t) = \int_{-\infty}^{t} \mathrm{d}t_1 f_s(\mathbf{k}, t_1)\, e^{-k^2\nu(t-t_1)} \,. \tag{3.26}$$

With the assumption that the large scales evolve slowly in time the first order solution of (3.24) is

$$\begin{aligned} \omega_s^{(1)}(\mathbf{k}, t) = &\int \mathrm{d}Q^2 \left[\frac{1}{\mathbf{Q}^2} - \frac{1}{(\mathbf{k}-\mathbf{Q})^2}\right] \mathbf{K}\cdot\mathbf{Q} \times \hat{\mathbf{e}}_\mathbf{z} \omega_L(\mathbf{Q}) \\ &\times \int_{-\infty}^{t} \mathrm{d}t_1 \omega_s^{(0)}(\mathbf{k}-\mathbf{Q}, t_1)\, e^{-\nu k^2 (t-t_1)} \,. \end{aligned} \tag{3.27}$$

The averages over nonlinearities in ω_s can now be calculated. The average over two zero order terms is

$$\langle \omega_s^{(0)}(\mathbf{k}_1, t)\, \omega_s^{(0)}\left(\mathbf{k}_2, t'\right)\rangle = \frac{\langle |f_s(\mathbf{k}_1)|^2\rangle}{\left(\mathbf{k}_1^2 + \mathbf{k}_2^2\right)\nu} \delta(\mathbf{k}_1 + \mathbf{k}_2)\, e^{-\nu k_1^2 (t-t')} \tag{3.28}$$

using (3.26) and the δ relation of the time for $\langle f_s(t_1) f_s(t_2)\rangle$ to integrate the first occurring time integral, whereas the second integral over the exponential is explicitly integrated for $t > t'$. Analogously the average over the product of a zero order with a first order vorticity term is

$$\begin{aligned} \langle \omega_s^{(0)}(\mathbf{k}_1, t)\, \omega_s^{(1)}\left(\mathbf{k}_2, t'\right)\rangle = &\frac{\mathbf{k}_2 \cdot \mathbf{k}_2 \times \hat{\mathbf{e}}_\mathbf{z}}{\nu\left(\mathbf{k}_1^2 + \mathbf{k}_2^2\right)} \left[\frac{1}{\left(\mathbf{k}_1 + \mathbf{k}^2\right)^2} - \frac{1}{\mathbf{k}_1^2}\right] \\ &\times \omega_L(\mathbf{k}_1 + \mathbf{k}_2) \left\langle \left|\omega_s^{(0)}(\mathbf{k}_1)\right|^2 \right\rangle e^{-\nu k_1^2 (t-t')} \end{aligned} \tag{3.29}$$

with $\left\langle \left|\omega_s^{(0)}(\mathbf{k}_1)\right|^2 \right\rangle \equiv \langle |f_s(\mathbf{k}_1)|^2\rangle / 2\mathbf{k}_1^2 \nu$. The equation governing the evolution of the large scales is given by averaging (3.19) over the small scales $\partial_t \omega_L + \mathbf{v}_L \cdot \nabla \omega_L = -\langle \mathbf{v}_s \cdot \nabla \omega_s\rangle =$

$\gamma_L \omega_L$. The excitation of the large scales by small scales is defined by the source term remaining after the average

$$-\langle \mathbf{v}_s \cdot \nabla \omega_s \rangle = \mathbf{K} \cdot \int \mathrm{d}q^2 \frac{(\mathbf{K}-\mathbf{q}) \times \hat{\mathbf{e}}_\mathbf{z}}{(\mathbf{K}-\mathbf{q})^2} \langle \omega_s (\mathbf{K}-\mathbf{q}) \, \omega_s (\mathbf{q}) \rangle \, . \tag{3.30}$$

The averages over two zero order terms of ω_s do not contribute due to the occurring $\delta(\mathbf{K})$. The contribution from the mixed order terms is

$$\begin{aligned} &\langle \omega_s^{(0)} (\mathbf{q}, t) \, \omega_s^{(1)} (\mathbf{K}-\mathbf{q}, t) + \omega_s^{(1)} (\mathbf{q}, t) \, \omega_s^{(0)} (\mathbf{K}-\mathbf{q}, t) \rangle \\ &= \frac{\mathbf{K} \times \mathbf{q} \cdot \hat{\mathbf{e}}_\mathbf{z}}{\nu \left((\mathbf{K}-\mathbf{q})^2 + \mathbf{q}^2 \right)} \left[\frac{1}{(\mathbf{K}-\mathbf{q})^2} - \frac{1}{\mathbf{q}^2} \right] \omega_L (\mathbf{K}) \, \langle \left| \omega_s^{(0)} (\mathbf{k}_1) \right|^2 \rangle \end{aligned} \tag{3.31}$$

yielding a growth rate for the large scale flows of

$$\gamma_L \equiv \int \mathrm{d}q^2 \frac{(\mathbf{K} \times \mathbf{q} \cdot \hat{\mathbf{e}}_\mathbf{z})^2}{(\mathbf{K}-\mathbf{q})^2} \left[\frac{1}{\mathbf{q}^2} - \frac{1}{(\mathbf{K}-\mathbf{q})^2} \right] \frac{\langle \left| \omega_s^{(0)} (\mathbf{q}) \right|^2 \rangle}{\nu \left((\mathbf{K}-\mathbf{q})^2 + \mathbf{q}^2 \right)} \, . \tag{3.32}$$

In polar coordinates with $\mathbf{K} \cdot \mathbf{q} / qK = \cos\theta$ the equation transforms into

$$\gamma_L = \int_{k_s}^{\infty} \mathrm{d}q q \int_0^{2\pi} \mathrm{d}\theta \frac{K^2 \sin^2\theta (K^2 - 2Kq\cos\theta)}{(K^2 + q^2 - 2Kq\cos\theta)^2} \frac{\langle \left| \omega_s^{(0)} (\mathbf{q}) \right|^2 \rangle}{K^2 + 2q^2 - 2qK\cos\theta} \, . \tag{3.33}$$

Due to the scale separation $K/q \ll 1$ and an expansion yields the two lowest order terms

$$\gamma_L^{(0)} = -\int_{k_s}^{\infty} \mathrm{d}q \int_0^{2\pi} \mathrm{d}\theta \frac{K^3}{q^4} \sin^2\theta \cos\theta \langle \left| \omega_s^{(0)} (\mathbf{q}) \right|^2 \rangle \tag{3.34}$$

$$\gamma_L^{(1)} = -\int_{k_s}^{\infty} \mathrm{d}q \int_0^{2\pi} \mathrm{d}\theta \frac{K^4 \sin^2\theta}{2q^5} \left[10\cos^2\theta - 1 \right] \langle \left| \omega_s^{(0)} (\mathbf{q}) \right|^2 \rangle \, . \tag{3.35}$$

The first order term $\gamma_L^{(0)}$ always vanishes as $\langle \left| \omega_s^{(0)} (\mathbf{q}) \right|^2 \rangle$ is symmetric with respect to $\mathbf{q} \to -\mathbf{q}$. The second order term $\gamma_L^{(1)}$ vanishes for an isotropic spectrum $\langle \left| \omega_s^{(0)} (q) \right|^2 \rangle$ but can be positive depending on the θ-dependence of the small scale spectrum and hence can lead to a growth of large scales.
This illustrates an inverse energy transfer mechanism from the small scale turbulence to the large scale flows. The ITG-turbulence is certainly anisotropic but any initial spectral gaps in a turbulent system are quickly closed [65] by the bidirectional feedback of the large and small scales. Similar methods of a direct calculation of the self-organization process appear therefore unsuited for a description of the time-evolution of ZFs since the prerequisites for their application do not persist after the initial phase of excitation.

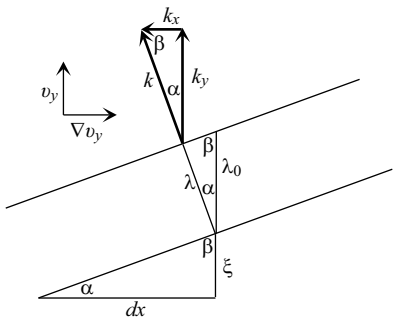

Figure 3.8: Wavefronts of a plane wave with the initial wavelength λ_0 after being subjected to a shear flow v_y for a time dt. The angles α, β indicate the similarities of the depicted triangles.

The effect of large scale flows on the turbulence is most intuitively understood when examining the shear action on a plane wave front (Fig. 3.8). A wave front that is initially perpendicular to the flow and parallel to the flow gradient is sheared after a time dt. The displacement of one of two points on the wavefront, initially apart by a length dx, in the flow direction is $\xi = \partial_x v_y x dt$. This changes the initial wavelength λ_0 to $\lambda = x/\sqrt{x^2+\xi^2} = 1/\sqrt{1+(\partial_x v_y)^2 dt^2}$ as the triangle similarity in the figure shows. The wave vector thus changes to $k = k_{y0}\sqrt{1+(\partial_x v_y)^2 dt^2}$ where k_{y0} is the wave vector of the initial wavefront. The change of the wave vector components (triangle similarity) is $k_x/k = -\xi/\sqrt{x^2+\xi^2}$ and $k_y/k = x/\sqrt{x^2+\xi^2}$ from which follows

$$\frac{\mathrm{d}k_x}{\mathrm{d}t} = -k_y \partial_x v_y \tag{3.36}$$

$$\frac{\mathrm{d}k_y}{\mathrm{d}t} = 0 \tag{3.37}$$

if the background flow v_y is constant over time. This shows how the shear flow changes the spectrum of the turbulence by slicing the eddies apart. One has to keep in mind though that this is a rather crude explanation as the ZFs and the turbulence vary on the same radial scales – see Chap. 4 – and the displacement ξ can no longer be estimated this crudely by an expansion of the shear flow velocity nor do well defined wave fronts exist.

Chapter 4

Zonal Flow Evolution

ZFs are radially nested layers of flux-surface averaged radial electric fields causing poloidal $\mathbf{E} \times \mathbf{B}$-flows with zero poloidal and toroidal mode numbers. Section 4.1 describes the derivation of the ZF momentum equation from the turbulence equations (2.63)-(2.67). The observations of the ZF behavior in the turbulence studies using the NLET code [64] are discussed in section 4.2. The interaction of the ZFs with the turbulence and the observed influence on the heat transport is addressed in section 4.3. All figures use the dimensionless units of NLET (discussed in Chap. 2). The conversion from the perpendicular length unit L_0 into the ion-gyro radius is $\rho_i/L_0 = \alpha\left(\epsilon_n(1+\tau)\right)^{1/2}$.

4.1 Derivation of the ZF Equations

Stationary ZFs require a parallel return flow along the field lines to cancel the compression due to the poloidal motion and the conserved magnetic flux. The divergence $\epsilon_n \sin(2\pi z)\,\partial_x \bar{\phi}$ of the flux-surface-averaged poloidal $\mathbf{E}\times\mathbf{B}$-flow must, therefore, equal the divergence $\epsilon_v \nabla_\parallel v_\parallel$ of the parallel flow which defines the return-flow

$$v_\parallel = -\frac{\epsilon_n}{2\pi\epsilon_v}\cos(2\pi z)\,\bar{v}_y\,, \tag{4.1}$$

where the overbar denotes the flux surface average $\langle \ldots \rangle_{y,z}$ and $v_y = \partial_x \phi$. The flux-surface-average of this equation multiplied by $\cos(2\pi z)$ yields the balance of the flow-averages

$$\bar{v}_y = -\frac{4\pi\epsilon_v}{\epsilon_n}\langle \cos(2\pi z)\, v_\parallel \rangle_{y,z} + \langle \cos(4\pi z)\, v_y \rangle_{y,z} \tag{4.2}$$

Taking the flux-surface average of the vorticity equation (2.64) and integrating over x yields the equation for the ZF time-evolution

$$\langle D_t \partial_x \left(\phi + \tau\alpha p_i\right) + \sin(2\pi z)\, p \rangle_{y,z} = 0\,. \tag{4.3}$$

A simple algebraic transformation, using the identity $\partial_y v_y = -\partial_x v_x$, $v_x \equiv -\partial_y \phi$, and the fact that all quantities are periodic in y, z, transforms the average $\langle D_t \partial_x \phi \rangle_{y,z}$ into

$$\begin{aligned} \langle D_t \partial_x \phi \rangle_{y,z} &= \langle \partial_t v_y + v_x \partial_x v_y + v_y \partial_y v_y \rangle_{y,z} \\ &= \langle \partial_t v_y + \partial_x \left(v_x v_y\right) \rangle_{y,z} \end{aligned} \tag{4.4}$$

whereas the average $\langle D_t \partial_x p_i \rangle_{y,z}$ leads to

$$\begin{aligned}\langle D_t \partial_x p_i \rangle_{y,z} &= \langle \partial_t \partial_x \; p_i + v_x \partial_x^2 p_i + v_y \partial_y \partial_x p_i \rangle_{y,z} \\ &= \langle \partial_t \partial_x p_i + \partial_x \left(v_x \partial_x p_i \right) \rangle_{y,z} \,. \end{aligned} \tag{4.5}$$

The sum of the equations (4.4) and $\tau\alpha$ times (4.5) yields

$$\begin{aligned}&\langle \partial_t \partial_x \phi + \tau\alpha \partial_t \partial_x p_i + \partial_x \left(v_x v_y + \tau\alpha v_x \partial_x p_i \right) \rangle_{y,z} \\ =&\langle \partial_t v_y + \tau\alpha \partial_t \partial_x p_i + \partial_x \left(\left(v_x + v_{dx} \right) v_y \right) + \tau\alpha \partial_x \left(v_y \partial_y p_i + v_x \partial_x p_i \right) \rangle_{y,z} \\ =&\langle \partial_t v_y \rangle_{y,z} + \partial_x \langle \left(v_x + v_{dx} \right) v_y \rangle_{y,z} + \partial_x \langle D_t p_i \rangle_{y,z} \end{aligned} \tag{4.6}$$

with $v_{dx} \equiv -\tau\alpha \partial_y p_i$. Subtracting this equation from (4.3) results in

$$\langle \partial_t v_y + \partial_x \left(\left(v_x + v_{dx} \right) v_y \right) + \tau\alpha \partial_x D_t p_i + \sin\left(2\pi z\right) p \rangle_{y,z} = 0 \,. \tag{4.7}$$

The last term can be eliminated using the flux-surface-average of the parallel velocity equation (2.67) times $\cos\left(2\pi z\right)$ and partial integration of the RHS

$$\begin{aligned}\langle \cos\left(2\pi z\right) D_t v_\parallel \rangle_{y,z} &= \langle \cos\left(2\pi z\right) \partial_t v_\parallel \rangle_{y,z} + \partial_x \langle \cos\left(2\pi z\right) v_x v_\parallel \rangle_{y,z} \\ &= -\epsilon_v \langle \sin\left(2\pi z\right) p \rangle_{y,z} \,. \end{aligned} \tag{4.8}$$

The third term of (4.7), $D_t p_i = D_t n + D_t T_i$ can be eliminated with the flux surface average of the density and temperature equations (2.65), (2.66)

$$\begin{aligned}\langle D_t n \rangle_{y,z} &= \underbrace{\langle \epsilon_n \sin\left(2\pi z\right) \partial_x \left(\phi - \alpha n \right) \rangle_{y,z}}_{= \langle \epsilon_n \sin(2\pi z) \partial_x \bar{\phi} \rangle_{y,z} = 0} - \underbrace{\langle \epsilon_v \nabla_\parallel v_\parallel \rangle_{y,z}}_{=0} + \underbrace{\alpha \epsilon_n \left(1 + \tau\right) \langle \nabla_\parallel J \rangle_{y,z}}_{=0} \\ &= 0 \end{aligned} \tag{4.9}$$

$$\begin{aligned}\langle D_t T_i \rangle_{y,z} &= \frac{2}{3} \langle \frac{5}{2} \tau\alpha \epsilon_n \sin\left(2\pi z\right) \partial_x T_i + D_t n \rangle_{y,z} \\ &= \frac{5}{3} \tau\alpha \epsilon_n \langle \sin\left(2\pi z\right) \partial_x T_i \rangle_{y,z} \\ &\Rightarrow \end{aligned} \tag{4.10}$$

$$\langle D_t p_i \rangle_{y,z} = \frac{5}{3} \tau\alpha \epsilon_n \langle \sin\left(2\pi z\right) \partial_x T_i \rangle_{y,z} \,, \tag{4.11}$$

which leads to

$$\begin{aligned}\langle \partial_t (v_y - \frac{1}{2\pi\epsilon_v} \cos\left(2\pi z\right) v_\parallel) \rangle_{y,z} = &- \partial_x \langle \left(v_x + v_{dx} \right) v_y - \frac{1}{2\pi\epsilon_v} \cos\left(2\pi z\right) v_x v_\parallel \rangle_{y,z} \\ &- \tau^2 \alpha^2 \epsilon_n \frac{5}{3} \partial_x^2 \langle \sin\left(2\pi z\right) T_i \rangle_{y,z} \,. \end{aligned} \tag{4.12}$$

Eliminating the parallel flow with the return flow relation (4.1) for the stationary branch of ZFs results in the momentum equation for the ZFs

$$\begin{aligned}\langle (1 + \frac{\epsilon_n}{(4\pi\epsilon_v)^2} \cos\left(2\pi z\right)^2) \partial_t v_y \rangle_{y,z} = &- \partial_x \langle \left(v_x + v_{dx} \right) v_y - \frac{1}{2\pi\epsilon_v} \cos\left(2\pi z\right) v_x v_\parallel \rangle_{y,z} \\ &- \tau^2 \alpha^2 \epsilon_n \frac{5}{3} \partial_x^2 \langle \sin\left(2\pi z\right) T_i \rangle_{y,z} \,. \end{aligned} \tag{4.13}$$

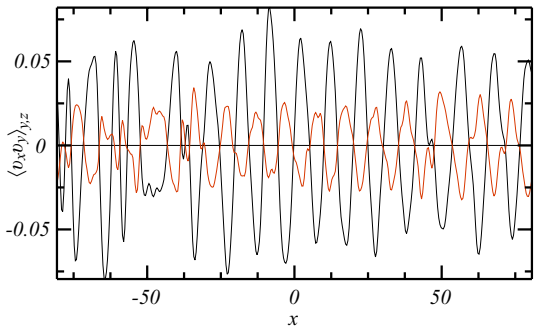

Figure 4.1: Perpendicular $\mathbf{E} \times \mathbf{B}$ stress $\langle v_x v_y \rangle_{y,z}$ (black) and temperature component $-\tau\alpha\langle \partial_y T_i v_y \rangle_{y,z}$ of the diamagnetic contribution (red) for the self-consistent ZF study shown in figure 4.3a at $t = 1800$.

The first term on the RHS of the equation is the divergence of the perpendicular Reynolds stress, the second term the divergence of the corresponding parallel stress component

$$R_\perp \equiv \langle (v_x + v_{dx})\, v_y \rangle_{y,z} \tag{4.14}$$

$$R_\parallel \equiv \frac{1}{2\pi\epsilon_v} \langle \cos(2\pi z)\, v_x v_\parallel \rangle_{y,z} = \frac{2q}{\sqrt{\epsilon_n}} \langle \cos(2\pi z)\, v_x v_\parallel \rangle_{y,z} \tag{4.15}$$

and the third term is a finite Larmor radius contribution $\sim \alpha^2 \epsilon_n k_x^2 = \rho_s^2 k_x^2/(1+\tau)^2$. This elucidates that ZFs are primarily Reynolds stress driven [32, 49, 63] and a good understanding of the stresses is imperative to predict the ZF evolution. In addition the dependence of the parallel stress contribution on the safety factor q reveals that dominant stationary ZFs are a core phenomenon and it was found that ZFs are completely suppressed for safety factors above 3 [49].
The diamagnetic part of the perpendicular stress consists of contributions by both density and temperature. The density contribution is equal to the $\mathbf{E} \times \mathbf{B}$-flow induced stress $\langle v_x v_y \rangle_{y,z}$ in the adiabatic case. The stress caused by the temperature fluctuations $-\tau\alpha\langle \partial_y T_i v_y \rangle_{y,z}$ is similar in structure to the $\mathbf{E} \times \mathbf{B}$ generated one but of opposite phase in the parameter regime examined within this thesis (Fig. 4.1). Here, the perpendicular stress is therefore proportional to its $\mathbf{E} \times \mathbf{B}$-flow induced part. This is not necessarily the general case but is pointed out here since it allows a direct comparison of the stress descriptions for $\langle v_x v_y \rangle_{y,z}$ discussed in chap. 6 with those obtained for $R_\perp$ in chap. 5.

4.2 Zonal Flow Evolution

To illustrate the different stages in ZF evolution the transition from a state showing a linear ITG-instability to a ZF-turbulence equilibrium is examined in a self-consistent study with the following parameters

$$L_x = 200 \quad L_y = 800 \quad \alpha = 0.5 \quad \epsilon_n = 1 \quad \tau = 1 \quad s = 1 \quad q = 1.5 \quad \eta_i = 2.4\,. \tag{4.16}$$

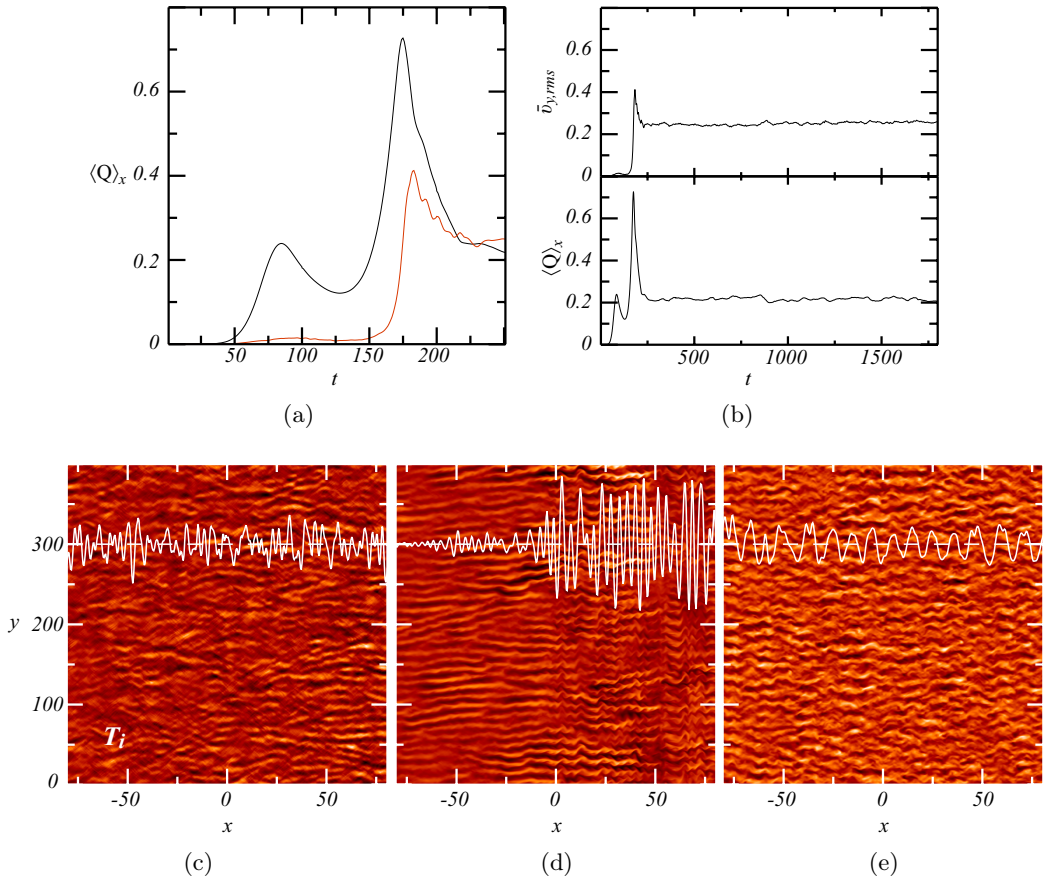

Figure 4.2: **(a)** Initial period of the time-evolution of the mean radial heat-flux $\langle Q \rangle_x$ (black) and the poloidal RMS $\mathbf{E}\times\mathbf{B}$-flow $\bar{v}_{y,rms}$ (red). **(b)** Long time-evolution of $\langle Q \rangle_x$ and $\bar{v}_{y,rms}$. Temperature fluctuations on the outboard midplane with the overlayed ZF velocities (rescaled by a factor f_s and shifted to $y = 300$) at $t = 120, f_s = 1000$ **(c)**, $t = 180, f_s = 50$ **(d)** and $t = 1800, f_s = 50$ **(e)**.

Figure 4.2a shows the radial average of the time-evolution of the radial heat flux $Q \equiv \langle v_x T_i \rangle_{y,z}$ and the corresponding flux-surface-averaged root-mean-square (RMS) $\mathbf{E}\times\mathbf{B}$-flow $\bar{v}_{y,rms}$. After a short phase of linear ITG-instability growth, the radial heat flux increases at $t = 50$ with the onset of weak turbulence and a marginal ZF is excited, which is followed by a delayed reduction of the heat flux. The temperature fluctuations during this stage (Fig. 4.2c) exhibit a structure similar to the linear ITG behavior with a subdominant turbulent contribution (Fig. 3.5c). When the system crosses over into a state of radial streamers at $t = 180$ (Fig. 4.2d) the corresponding radial heat transport increases significantly but the turbulence simultaneously excites a strong ZF (Fig. 4.2a) that tears the streamers apart and acts as a reduction mechanism for the transport [36, 37, 35]. Both, ZF and heat flux, saturate into a stable equilibrium state that is nearly stationary over long time scales (Figs. 4.2b,4.2e).

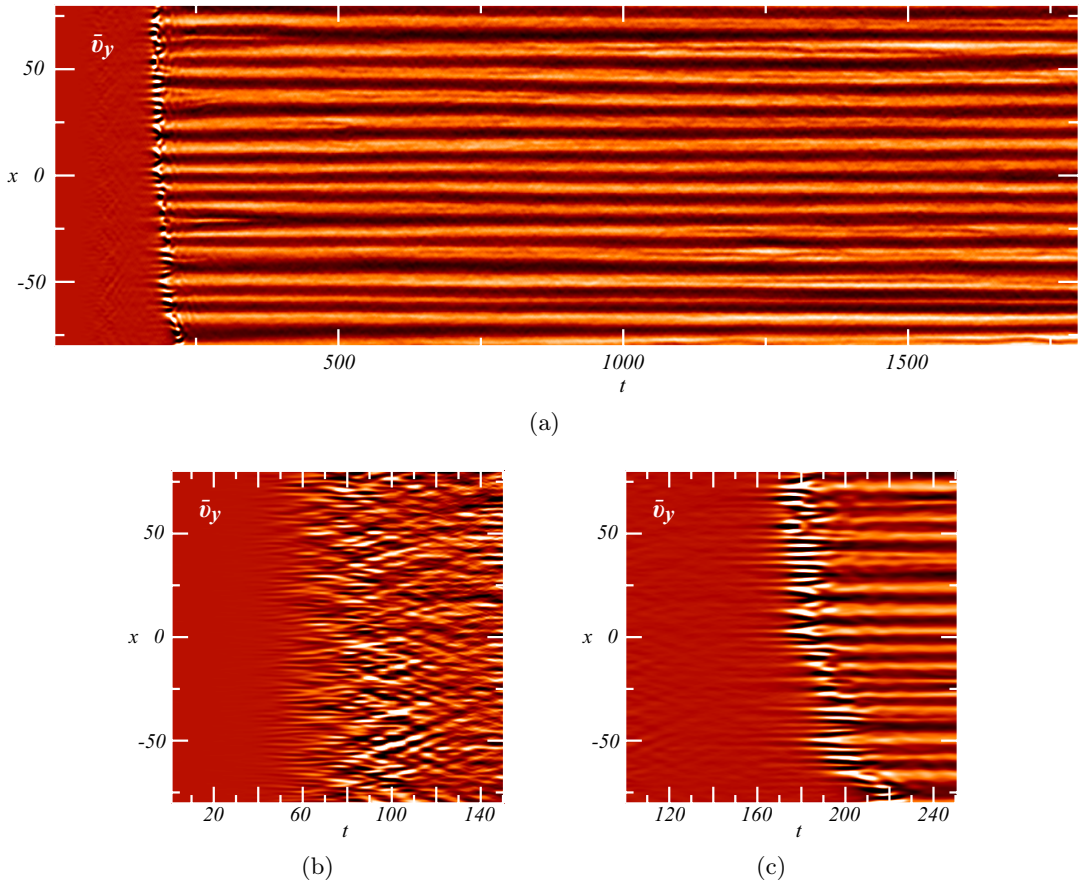

Figure 4.3: **(a)** Time-evolution of the poloidal ZF-profile $\bar{v}_y$. **(b)** Initial section of (a) from $t = 0$ to $t = 150$ showing marginal ZFs . **(c)** Section from $t = 100$ to $t = 250$ showing the transition to strong ZFs in the streamer regime.

Comparison of the instantaneous ZF velocities overlayed in the figures 4.2c-4.2e shows that the radial wave-number changes with the turbulence regime. In the early state of marginal ZF activity flows of small scale lengths are excited with wave-numbers that are higher in comparison to the equilibrium and the time-evolution (Fig. 4.3b) reveals that the ZFs are also non-stationary in this case. The state of radial streamers, on the other hand, excites a characteristic ZF mode (Fig. 4.2d) that appears to be stationary but only for the short time period between $t = 180$ and $t = 200$ during which the turbulence intensity adjusts to the ZF (Fig. 4.2a). Afterwards, the ZF scale increases and then appears to be almost completely stationary for long time periods (often over time scales several orders of magnitude larger than the sound transit time, Figs. 4.3a,4.2e).

This elucidates that a simple analysis of ZF growth rates, e.g. using the inverse energy transfer model summarized in Chapter 3.3, is unsuitable to describe the turbulence level and ZF-evolution of the equilibrium state since both turbulence and ZFs change after the initial growth phase.

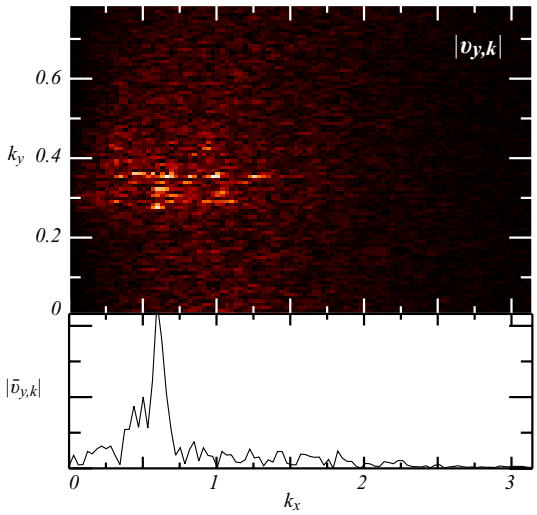

Figure 4.4: Top: Spectrum of the poloidal velocity fluctuations $|v_{y,k}|$ on the out-board-midplane at $t = 1800$. Bottom: Spectrum of the ZF.

During the initial growth phase of non-marginal ZFs the spectrum of the turbulence is dominated by $k_x = 0$ of the streamers whereas the initial radial wave-number of strong ZFs is much higher, $k_x > 0.5$. In this phase a separation of scales is satisfied as the wave-numbers in the y-direction are always disparate. Comparison of the spectrum of the turbulent poloidal velocity fluctuations with the ZF spectrum of the equilibrium state reveals though that in this case the radial wave-numbers are quite similar (Fig. 4.4). This somewhat confounds theories that assume a scale separation.
A turbulence study with a domain $L_x \times L_y = 100 \times 800$ where the background gradients near the simulation boundaries are not flattened and otherwise parameters equal to (4.16) allows the ZFs to "drift" radially out of the simulation domain (Fig. 4.5a). This drift changes the radial scale length of the ZFs. But, whenever an intrinsic lower threshold for the radial scale length is reached a new flow grows to maintain the characteristic scale length. Modification of a turbulent state at $t = 5500$ by stretching the poloidal- and corresponding return-flow and continuing the turbulence study from this state shows (Fig. 4.5b) that an intrinsic mechanism quickly restores the radial scale length. A further study, initialized with a flow having a hat-structure that was artificially maintained for a time long enough for the turbulence to adjust itself to the flow, revealed (Fig. 4.5c) that, self-consistently, such a flow also decays into the same pattern as produced by self-consistently excited ZFs. This illustrates the robustness of the ZF scale length which is entirely intrinsic and indifferent to the initial conditions. The conclusion is, arbitrary flows always decay into a pattern with the same radial scale length for one set of parameters.
Comparison of the flow with the corresponding stress pattern (Fig. 4.6a) reveals that the stress has a dominant deterministic part, which means a significant portion of the stress response can be clearly attributed to the flow structure and amplitude. Similar features observable in stress and flow appear to be closely correlated, the most obvious being the

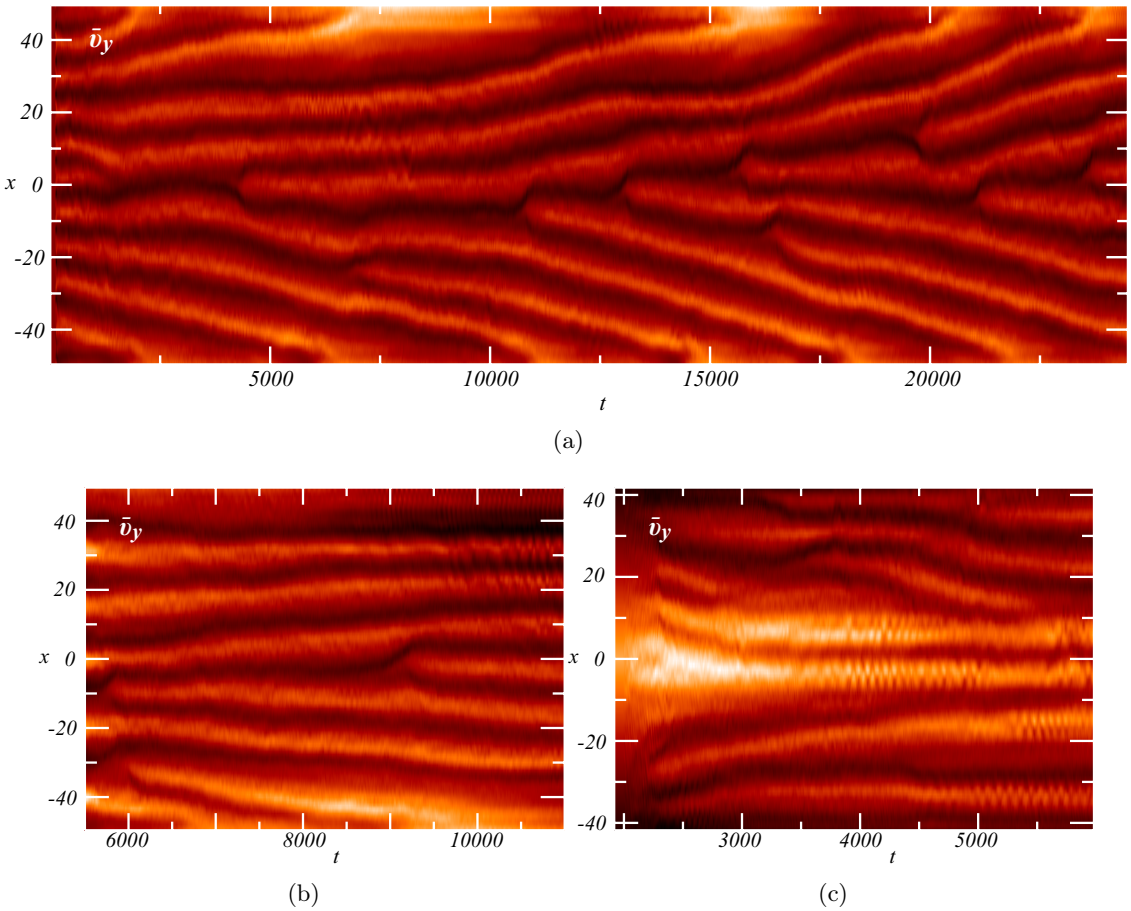

Figure 4.5: **(a)** ZF time-evolution where boundary conditions allow the flows to "drift" outside the domain. **(b)** Self-consistent evolution of an artificially stretched flow profile taken from (a) at $t = 5500$. **(c)** Decay of a hat flow-profile into the self-consistent ZF pattern.

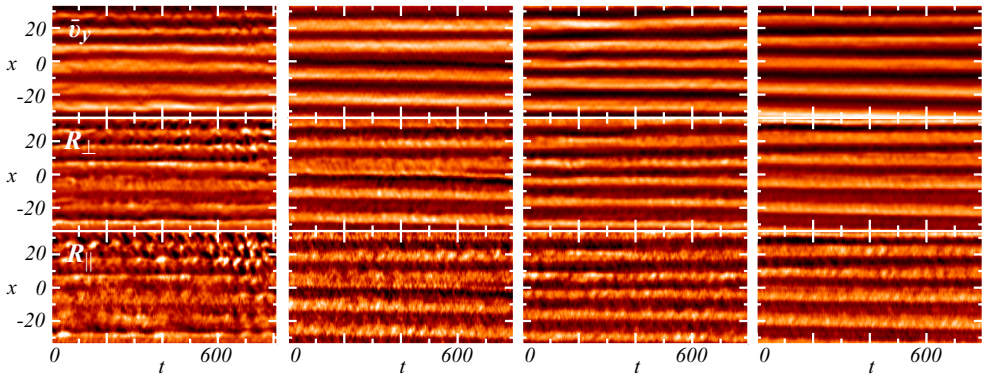

Figure 4.6: Time-evolution of: poloidal flow (top), perpendicular stress (middle plot) and parallel stress component (bottom). The domain sizes in the y-direction are **(a)** $L_y = 400$, **(b)** $L_y = 800$, **(c)** $L_y = 1600$, **(d)** $L_y = 3200$

radial scale length. An increase of the domain in the y-direction leads to a flux-surface average over a larger number of turbulent eddies and, therefore, the stress patterns become more deterministic the larger the computational domain is (Figs. 4.6a-4.6d).

The relatively persistent characteristic structure of the ZFs and the dominant deterministic part of the stress patterns suggests that a functional describing the stress can be constructed. This would greatly simplify the study of ZF-turbulence interaction as ZFs are primarily governed by the stresses, recall Eq. (4.13). Furthermore, a prediction of the ZF evolution will then be possible which is a requirement for a prognosis of the turbulence level.

A comparison of the instantaneous flow and return-flow profiles (Fig. 4.7a) in the equilibrium state with the aforementioned parameters (4.16) (at $t = 1000$ of Fig. 4.3a) shows that the balance (4.2) of the poloidal and parallel return-flow is well satisfied by $\bar{v}_y = -4\pi\epsilon_v \langle \cos(2\pi z)\, v_\parallel \rangle_{y,z} / \epsilon_n$ [49, 63]. The higher harmonic contributions of the return-flow proportional to $\cos(4\pi z)$ are negligibly small. The parallel flow contains the major part of the ZF energy in fact [49], such that it is imperative to treat the parallel stress component with the same thoroughness as the perpendicular one. A point which all contemporary ZF theories do not take into account adequately. They either neglected the parallel stress component entirely or just attributed a viscous damping effect to it.

A time-average of the corresponding stresses over a short time interval around $t = 1000$ yields the mostly deterministic stress profiles (Fig. 4.7b) with a structure similar to the flow. This suggests that the instantaneous flow profile is one degree of freedom for a stress approximation. Both stresses nearly balance out and the total stress $R_\perp - R_\parallel$ is one magnitude smaller than its individual constituents. Examination of its time-evolution (Fig. 4.7c top) reveals that the total stress consists mostly of random fluctuations. That is not surprising since a significant deterministic part would change the flow pattern which is stationary in this case though. The time-evolution and profile of the last contributor

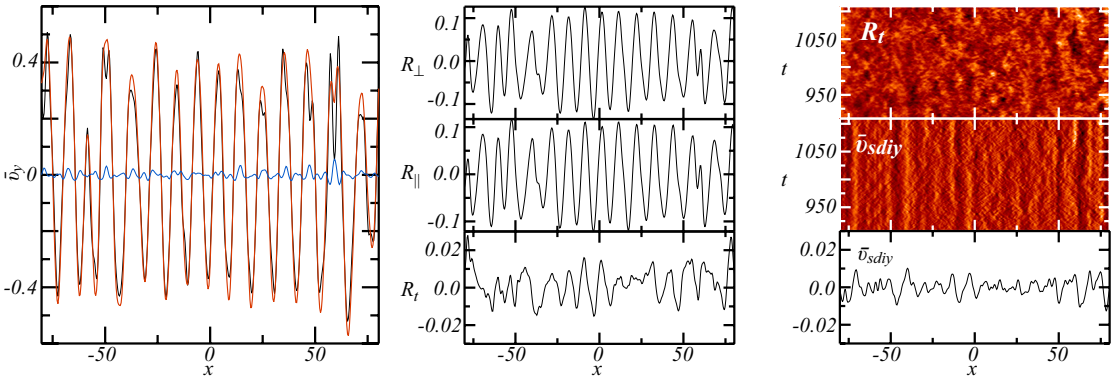

(a) (b) (c)

Figure 4.7: **(a)** Equilibrium flow-balance of poloidal flow $\bar{v}_y$ (black) and return flow $\langle \cos(2\pi z)\, v_\parallel \rangle_{y,z}$ (red) with the higher order contribution $\langle \cos(4\pi z)\, v_y \rangle_{y,z}$ (blue) at $t = 1000$ of Fig. 4.3a. **(b)** Time-averaged stress profiles of $R_\perp$ (top), $R_\parallel$ (middle) and $R_\perp - R_\parallel$ (bottom) over $t = 900$ to $t = 1100$. **(c)** Time-evolution of the total stress profile (top), time-evolution (middle) and profile (bottom) of $v_{sdiy} \equiv \langle \sin(2\pi z)\, \partial_x T_i \rangle_{y,z}$.

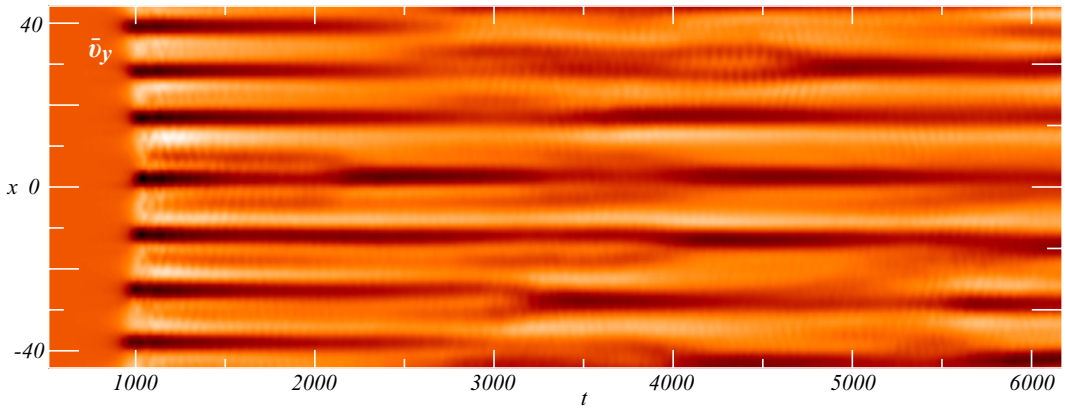

Figure 4.8: Time-evolution of the ZF profile obtained using the GYRO code [66] with parameters equivalent to 4.16 and NLET scales.

$\langle \sin(2\pi z)\, \partial_x T_i \rangle_{y,z}$ on the RHS of (4.13) is shown in middle and bottom figures 4.7c. Although some persistent structures appear in the time-evolution, they are of the order of the random fluctuations as comparison with the total stress profile (Fig. 4.7b bottom) indicates. This contribution caused by the ion-diamagnetic heat flux will not be further considered in the following but cases in other parameter regions may exist where it becomes important.
A gyro-kinetic study using the GYRO code [66], with parameters equivalent to the ones used for the discussed fluid studies, is shown in figure 4.8. Compared to the figures 4.3a or 4.6a-4.6d the ZFs of the two-fluid and the gyro-kinetic studies show a qualitatively equal behavior. The ZF in the gyro-kinetic case also appears to be nearly stationary with a distinct radial scale. This verifies that the fluid framework describes the ZF evolution sufficiently such that the construction of a stress functional derived in the fluid framework is justified. Moreover, the lower computational expenses of fluid studies over gyro-kinetic ones are in this case essential since a large number of simulations are required to stake out the requirements for the stress functional.

4.3 Zonal Flow Turbulence Interaction

The heat-flux pattern of the self-consistent ZF-equilibrium corresponding to the parameters (4.16) shows instantaneous random fluctuations (Fig. 4.9a), which can locally have the same order of magnitude as the time-average of the mean radial heat-flux. These strong fluctuations are countered by a slight, temporary increase in ZF activity (Fig. 4.9b), as the deviation of the instantaneous flow profile from its time-average indicates. This shows that the ZFs, self-consistently, respond to larger fluctuations in the heat-flux and that a feedback mechanism exists which maintains the ZF-turbulence equilibrium. This self-consistent equilibrium state is characterized by an average heat flux $\langle Q \rangle_{xt} = 0.2$, a root-mean-square (RMS) flow-level of $\langle \bar{v}_y^2 \rangle_{xt}^{1/2} = 0.28$ and a RMS shearing-rate $\sqrt{\langle u^2 \rangle_{xt}} = 0.16$ for the examined parameter set.
There are cases, though, where the heat-flux shows pronounced deterministic features caused by a shear-flow. A turbulence study with an artificial flow pattern of wave-number $k_x = 0.19$, RMS shearing-rate of $\sqrt{\langle u^2 \rangle_{xt}} = 0.1$ and a turbulence level close to the self-consistent equilibrium state reveals corrugations in the heat-flux near the extrema of the flow (Fig. 4.10a). The flow direction appears to be relevant for the shape of the corrugation peaks. The peaks around flows in the electron-diamagnetic-drift direction (positive flows) appear broad with a flat top almost a double peak. The peaks around flows in the opposite, ion-diamagnetic, direction (negative flows) have a thinner shape and a higher amplitude than the other peaks. An analysis of the ZF-turbulence interaction in [57] indicated that a heat-flux amplification at flow maxima is due to a transient wave-kinetic concentration of fluctuation energy and not caused by an increased drive of turbulence as suggested by [96]. But this does not explain the peaks in the negative flow direction. Efforts to explain the heat-flux modulations with a trapping of turbulent wave-packets [97] do not describe the observations of peaks at both the positive and negative flow extrema. The idea of wave trapping is that the radial wave-number of a small wave packet in a large scale shear

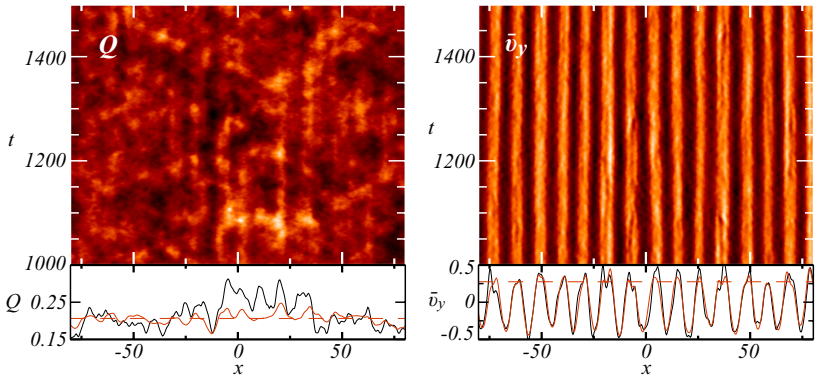

(a) (b)

Figure 4.9: **(a)** Radial heat-flux time-evolution (top) and radial profiles (bottom) with instantaneous profile at $t = 1100$ (black), time-averaged profile (red) and mean profile (dashed). **(b)** Corresponding poloidal flow pattern (top) and radial profile (bottom) with instantaneous profile at $t = 1100$ (black), time-averaged profile (red) and RMS flow (dashed).

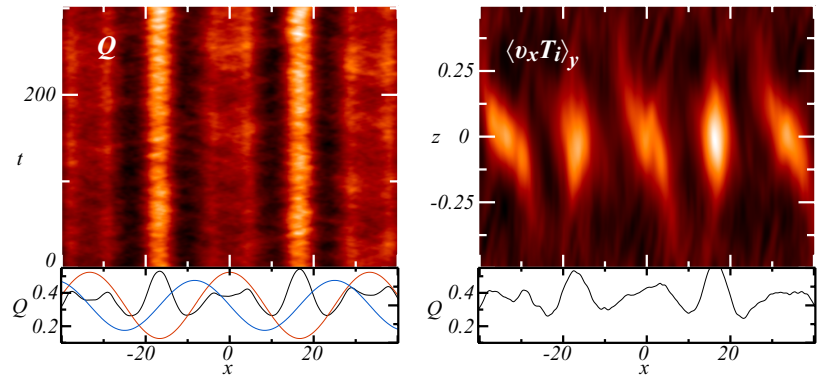

(a) (b)

Figure 4.10: **(a)** Time-evolution of the radial heat-flux for an artificial flow with $k_x = 0.19$ (top) and heat-flux profile (black), $0.25\bar{v}_y + 0.325$ profile (red) and shearing-rate profile $u + 0.325$ (blue) (bottom). **(b)** Instantaneous parallel heat-flux distribution $\langle v_x T_i \rangle_y$ (top) and corresponding radial profile (bottom).

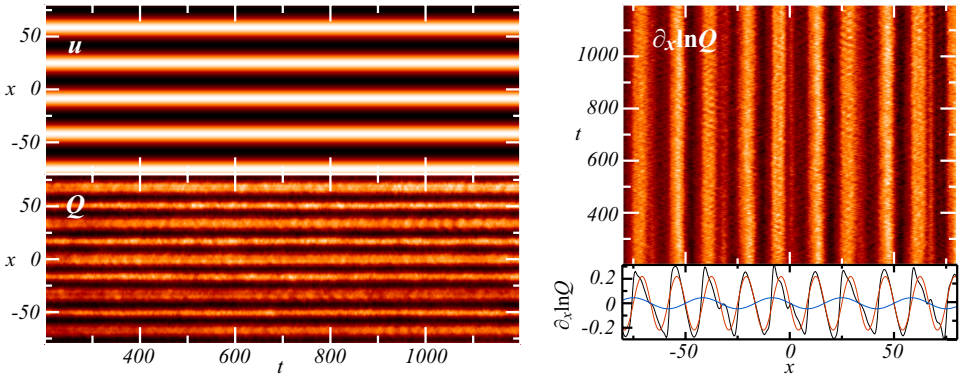

Figure 4.11: **(a)** Time-evolution of an artificial shearing-rate $u = 0.45 \sin(12\pi x/L_x)$ (top) in a turbulence study and the corresponding radial heat-flux Q (bottom). **(b)** Time-evolution of the corresponding heat-flux gradient $\partial_x \ln Q$ (top) and radial profile of its time-average (black) with a least-squares fit by $\partial_x u^2$ (red) and $0.1u$ (blue) (bottom).

flow is influenced by the local shearing-rate, $\mathrm{d}k_x/\mathrm{d}t = -|k_y|\,u$. The radial propagation velocity of the wave packet then becomes space time dependent $\mathrm{d}x/\mathrm{d}t = v_{gx}(k_x(x,t),k_y)$ [$v_{gx} = -2\alpha^3\epsilon_n k_x k_y/\left(1+\alpha^2\epsilon_n k_\perp^2\right)$ for DWs analyzed in [97]]. This describes an oscillation of the wave packet around the positive flow but not around the negative one. Any excited wave-packet propagates towards the nearest positive flow and oscillates if the initial radial velocity is large enough to cross the flow maximum. For an insufficient initial velocity the radial propagation is stopped after a time, $v_{gx} \to 0$, and the flow shear eventually annihilates the wave-packet, $|k_x| \to \infty$.

Comparison of the instantaneous heat-flux profile at $t = 0$ and the parallel heat flux distribution $\langle v_x T_i \rangle_y$ shows (Fig. 4.10b) that the heat-flux modulations are localized around the outboard-midplane at $z = 0$ but extend anti-symmetrically along the field lines for the positive flows and symmetrically for the negative flows. This illustrates why the peaks around the positive flows are broad, featuring a double peak. The descriptions for the influence of shear flows on the turbulence do not incorporate this three-dimensional effect and do not fully explain the observed turbulence repose.

A turbulence study with the parameters

$$L_x = 200 \quad L_y = 400 \quad \alpha = 0.5 \quad \epsilon_n = 1 \quad \tau = 1 \quad s = 1 \quad q = 1.5 \quad \eta_i = 3.4 \qquad (4.17)$$

and an artificial shearing-rate $u = 0.45 \sin(12\pi x/L_x)$ with a large amplitude shows a highly corrugated heat-flux pattern (Fig. 4.11a). In this case, the heat-flux corrugations do not show such a pronouncedly different behavior for positive and negative flows which is due to a higher shearing-rate amplitude, as studies with lower amplitudes have confirmed. The only difference that can still be observed is the width of the corrugations which are slightly broader for positive flows. The higher the shearing-rate amplitude is the more pronounced the corrugations become.

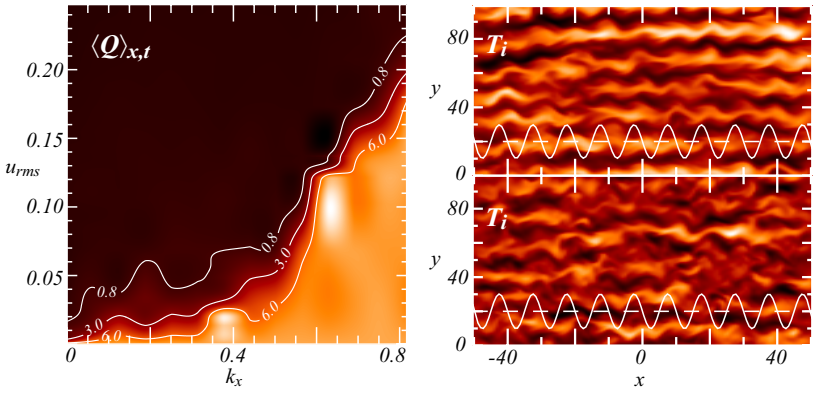

Figure 4.12: **(a)** Contour plot of the time and space averaged heat-flux $\langle Q \rangle_{x,t}$ observed in artificial flow studies with different wave-numbers k_x and amplitudes $u_{rms} = \langle \bar{v}_y^2 \rangle_{xt}^{1/2}$. The average heat-flux level appears to be dependent on both quantities. **(b)** Instantaneous temperature fluctuation pattern on the outboard-midplane in a study with artificial flows of $k_x = 0.63$, $\sqrt{\langle u^2 \rangle_{xt}} = 0.137$ (top) and $k_x = 0.63$, $\sqrt{\langle u^2 \rangle_{xt}} = 0.142$ (bottom). Overlayed are the ZF shearing-rates (white) rescaled by a factor 50 and the zero mean shearing-rate line (dashed). Comparison indicates a threshold for the turbulence reduction mechanism.

Since the heat-flux appears to be nearly stationary a time-average can be used to separate the random remnants from the deterministic response to shear flow. Examination of the time-averaged heat-flux gradient profile $\partial_x \ln Q$ reveals that it is proportional to $\partial_x u^2$ (Fig. 4.11b).

An ensemble of turbulence studies with artificial flows, held constant over time, of different radial wave-numbers and shearing-rates reveals that the amount of radial heat-flux is dependent on both quantities (Fig. 4.12a). As the flows are constant, an average of the heat-flux over radius and time eliminates most of the random fluctuations. Large scale shear flows appear to have an immediate effect on the turbulence even for small shearing-rates. On the contrary, the turbulence appears to be unaffected by small scale flows at low shearing-rates. This suggests that for small scale flows with small amplitudes the radial velocity of the turbulent eddies is large enough such that the flow cannot change the radial wave-number significantly before a transition to a region with a shearing-rate of opposite sign occurs. This is supported by comparison of the temperature fluctuations on the outboard-midplanes for a flow with $k_x = 0.63$, $\sqrt{\langle u^2 \rangle_{xt}} = 0.137$ and $\langle Q \rangle_x = 2.6$ against a flow with $k_x = 0.63$, $\sqrt{\langle u^2 \rangle_{xt}} = 0.142$ and $\langle Q \rangle_x = 0.57$ (Fig. 4.12b). The shearing-rate of the former flow is not yet high enough to tear the radial streamers apart entirely and only minor corrugations of the streamers due to the flow are already visible. In the latter case the shearing-rate is only slightly higher but strong enough to distort the eddies significantly such that the streamers disappear, accompanied by a large reduction of the heat-flux.

Figure 4.13a shows the time-averaged mean radial heat-flux dependence on the shearing-rate for three different radial scales $k_x = 0, k_x = 0.13$ and $k_x = 0.38$ (note that the maximal

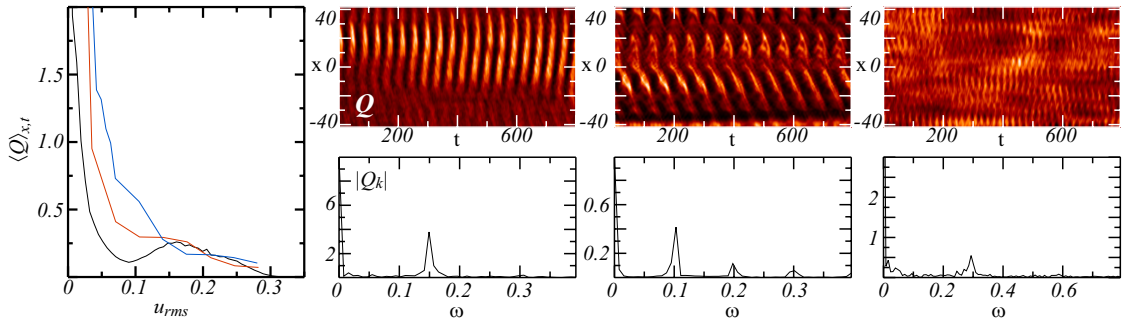

Figure 4.13: (a) Dependence of the time-averaged mean heat-flux of figure 4.12a for three radial wave-numbers $k_x = 0$ (black), $k_x = 0.13$ (red) and $k_x = 0.38$ (blue) on the shearing-rate amplitude u_{rms}. **(b)-(d)** Heat-flux time-evolution profiles (top) and frequency spectra (bottom) in studies with a shearing-rate $k_x = 0, u = 0.15$ for magnetic shears $s = 1$, $s = 1.5$ and $s = 0.5$ respectively. The frequency of the prominent heat-flux oscillation depends on shearing-rate $u = s\omega_m$.

heat-flux without ZFs is $Q \approx 8$ for the parameter set used here). When the shearing-rate reaches the critical threshold where the streamers are torn apart the heat-flux decreases rapidly to a range slightly above the self-consistent value. For any further increase of the shearing-rate one would expect a decrease of the heat-flux until the flows become strong enough to quench the turbulence entirely. However, the increase of the mean heat-flux with the shearing-rate for the wave-number $k_x = 0$ after the initial large decrease is unexpected. Since averages over larger time scales, different initial states or different domain resolutions did not impact the heat-flux increase with the shearing-rate, this cannot be attributed to statistics. Examination of the time-evolution of the heat-flux for the $k_x = 0$ case with a shearing-rate of $u = 0.15$ reveals deterministic oscillations (Fig. 4.13b) with a frequency $\omega = 0.15$.

The explanation for the oscillation is a wave moving along the magnetic field with a velocity v_{gz}. The parallel propagation generally results in a change of the the radial wave-number due to the magnetic shear. Analog to the change of the wave-number due to a shear flow (recall Fig. 3.8), the poloidal shift after a time interval dt of two points initially separated by a distance ∂_x in the radial direction is $\xi = 2\pi s z dx = 2\pi s v_{gz} dt dx$. This leads to an effective shearing-rate due to magnetic shear of $\partial_x v_s = 2\pi s v_{gz}$. The total rate of change for the radial wave-number is

$$\frac{\mathrm{d}k_x}{\mathrm{d}t} = -k_y \partial_x \left(v_y + v_s\right) . \tag{4.18}$$

In case of $\partial_x v_y = -\partial_x v_s$ the radial wave-number stays constant over time as the shear flow negates the shear effect of the magnetic field. This way a propagating mode with $k_x \approx 0$ on the outboard-midplane can survive the destructive influence of the magnetic shear that otherwise results in a decay on the high field side. The frequency of one complete poloidal propagation is $\omega_m = 2\pi v_{gz}/L_z$ and thus

$$\partial_x v_y = s\omega_m \tag{4.19}$$

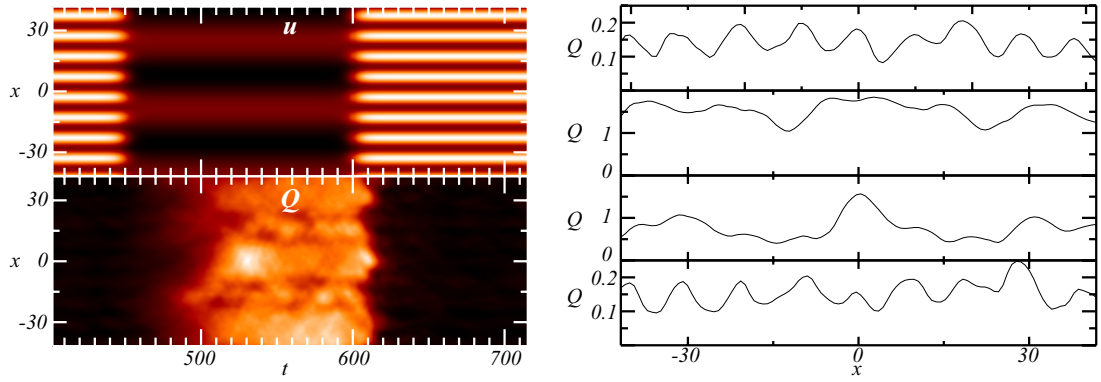

(a) (b)

Figure 4.14: **(a)** Time-evolution of a sharing rate pattern u alternating between $u_1 = 0.05\sin(6\pi/L_x)$ and $u_2 = 0.1\sin(20\pi/L_x)$ (top) and corresponding heat-flux pattern Q (bottom). **(b)** Instantaneous heat-flux profiles at times $t = 420$, $t = 600$, $t = 610$ and $t = 710$ from top to bottom. Comparison reveals that Q does not adjust instantaneously to u.

since $L_z = 1$. The heat-flux increases whenever the dominant wave-number on the low-field side reaches $k_x = 0$ resulting in the observed oscillations with the frequency ω_m. Turbulence studies with different magnetic shears (Figs. (4.13c),(4.13d)) corroborate this finding, as the occurring heat-flux oscillations have exactly the frequencies predicted by (4.19) and higher harmonics thereof.
The intensity of the heat-flux oscillations decreases with the radial scale length of the flows since a strong local gradient of the shearing-rate inhibits the compensation of the magnetic shear effect. Additionally, self-consistent flows also react to the changes in heat-flux such that the effect becomes a subdominant feature but can nevertheless sometimes be observed (e.g. Fig. 4.5c at $x = -35$ between $t = 5000$ ant $t = 6000$). One should note that this feature is also highly influenced by the magnetic field configuration such that it may turn out to be unobservable in a shaped geometry.
A turbulence study with the parameters

$$L_x = 100 \quad L_y = 400 \quad \alpha = 0.5 \quad \epsilon_n = 1 \quad \tau = 1 \quad s = 1 \quad q = 1.5 \quad \eta_i = 2.4\,. \tag{4.20}$$

and a shearing-rate pattern alternating in time between $u_1 = 0.05\sin(6\pi/L_x)$ and $u_2 = 0.1\sin(20\pi/L_x)$ shows how the heat-flux reacts to sudden changes of the ZFs (Fig. 4.14a). The shearing-rates are disparate enough such that their equilibrium heat-fluxes are quite different. This leads to a significant change of the heat-flux level whenever the shear flow pattern alternates. The time-frame after a flow pattern transition in which the heat-flux adjusts to the changed flow depends on the effectiveness of the shearing action on the turbulence. In this case, the large scale shearing-rate takes a time $\Delta t = 75$ to readjust the turbulence to its associated equilibrium level. The small scale shearing-rate appears to be more effective such that the equilibrium level appears to be reached at a time $t = 20$ after the transition. Comparison of the instantaneous heat-fluxes at times $t = 420$, $t = 600$, $t = 610$ and $t = 710$ reveals (Fig. 4.14b) that not only the mean radial heat-flux level

but also the corrugations require some time to adjust to the changed shearing-rate. The conclusion is, that the turbulence has a memory of both scale and amplitude of the shearing-rates it was recently influenced by.
Overall, the discussed observations indicate that the instantaneous heat-flux depends not only on the properties of the primary instability that generates it but also depends non-trivially on the history of the ZF-turbulence interaction. The radial scale as well as the amplitude of the shearing-rate effect both, the radial mean heat-flux and the corrugations. Any description of the turbulence must therefore be accompanied by a description of the ZF evolution as both are inseparable and interacting strongly in this regime.

Chapter 5

Derivation of the Reynolds Stress Functional

Due to the complexity of the plasma turbulence equations (2.63)-(2.67) and the fact that ZFs are a result of nonlinear interactions, the behavior of ZFs does not become obvious when examining the equations, opposite to the more easily calculated behavior of linear instabilities. As was discussed in Chapter 4, ZFs are a crucial ingredient to limit the radial transport, which should preferably be as low as possible in a fusion device. As the perpendicular and parallel Reynolds stresses have a dominant deterministic contribution (recall Fig. 4.6) that changes only slowly over time (usually over many parallel sound transit times), the construction of a response functional seems possible. This functional will allow the prediction of ZFs and permit a reliable mapping of ZF-turbulence equilibrium states. All figures use the dimensionless units of NLET (discussed in Chap. 2). The conversion from the perpendicular length unit L_0 into the ion-gyro radius is $\rho_i/L_0 = \alpha\,(\epsilon_n(1+\tau))^{1/2}$.

5.1 Stress Response Behavior

The initial observations in Chapter 4 point towards the flow as one degree of freedom for the stress functional. All terms in the functional must comply with the turbulence equations symmetries (2.69) though, such that the shearing-rate and not the flow itself is the adequate quantity to use in the functional. The intent is to identify the major contributions in turbulence studies and construct a functional that describes the most important ZF features, in particular growth, radial scale length and finite saturation.
Comparison of the shearing-rate u (Fig. 5.1a) and the stress pattern (Fig. 5.1b) for the self-consistent flow pattern shown in Figure 4.3a and the parameters

$$L_x = 200 \quad L_y = 800 \quad \alpha = 0.5 \quad \epsilon_n = 1 \quad \tau = 1 \quad s = 1 \quad q = 1.5 \quad \eta_i = 2.4 \tag{5.1}$$

indicates that both stresses, perpendicular as well as parallel, are correlated with the shearing-rate. As all three patterns are nearly constant over time one can take their time-average to remove random fluctuations (Fig. 5.2).

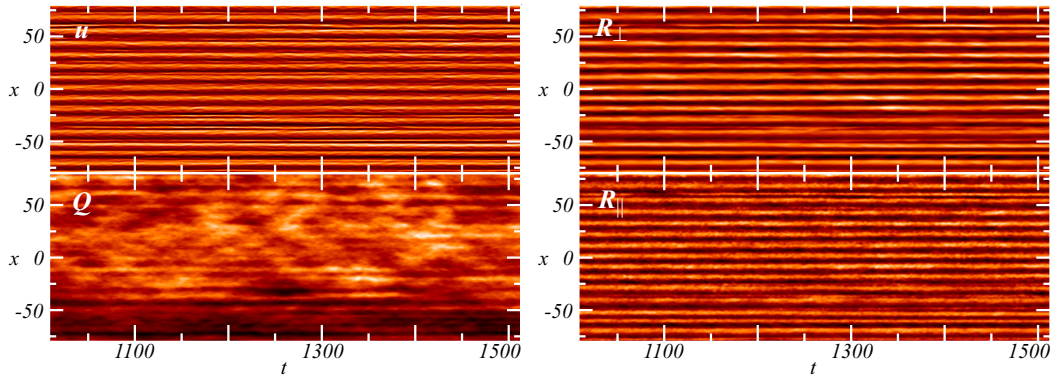

Figure 5.1: (a) Time-evolution of the shearing-rate u (top) and the radial heat-flux Q (bottom). (b) Corresponding perpendicular $R_\perp$ (top) and parallel $R_\parallel$ (bottom) stresses. Comparison shows that $R_\perp, R_\parallel$ and u are correlated.

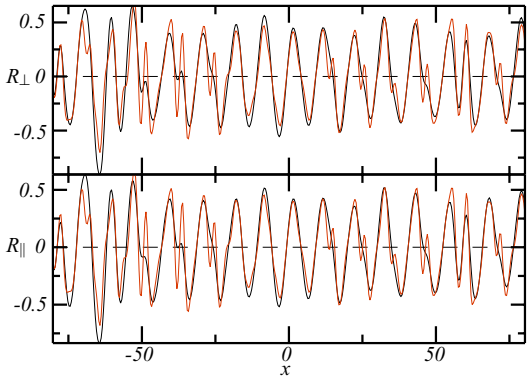

Figure 5.2: (top) Radial profile of the time-average of the perpendicular stress $R_\perp$ (black) of Fig. 5.1b and corresponding rescaled shearing-rate u (red). (bottom) Radial profile of the time-average of the parallel stress $R_\parallel$ (black) of Fig. 5.1b and corresponding rescaled shearing-rate u (red). Comparison reveals that $R_\perp, R_\parallel \sim u$.

Both stresses are proportional to the shearing-rate. The most dominant contributor to the stresses is accordingly the shearing-rate. To identify the other stress contributions it is necessary to examine the ZF stress relation slightly away from the equilibrium employing artificial flows. The first challenge is to define adequate flows that lead to a deterministic stress response uniquely assignable to a specific term in the functional, while also yielding a turbulence level close to the equilibrium. This required a large amount of turbulence studies to identify adequate parameter sets. A simple least-squares fit of the stresses by several terms obeying the turbulence equations symmetries (2.69) in general cases is simply inadequate to distinguish different sets of terms.

A turbulence study with the parameters

$$L_x = 2000 \quad L_y = 4000 \quad \alpha = 11.58 \quad \epsilon_n = 1 \quad \tau = 1 \quad s = 0.8 \quad q = 1.4 \quad \eta_i = 3.114 \quad (5.2)$$

and an artificial shearing-rate $u = 0.2 \sin(2\pi x/L_x) \sin(2\pi t/1200)$, which slowly changes over time, reveals (Fig. 5.3a) that the heat-flux stays constant as long as the shearing-rate is not close to zero. The stress patterns (Fig. 5.3b) reflect the alternating pattern of the shearing-rate. At times where the local shearing-rate changes its sign the mean radial heat-flux Q increases by orders of magnitude, accompanied by stress fluctuations not proportional to the shearing-rate, as a time trace at $x = -500$ of the heat-flux and stresses (Fig. 5.4a) reveals. Rescaling the stresses with Q , however, restores the intensity of the stress fluctuations to a level constant over the entire oscillation such that the rescaled stresses are proportional to the shearing-rate everywhere. This suggests that Q (or another turbulence intensity measure) is a second degree of freedom required to construct an adequate stress response functional.

A time-average over several flow oscillations yields stress profiles where the contributions caused by u are removed (Fig. 5.4b). The residual of the perpendicular stress average is proportional to the gradient of the heat-flux $\partial_x \ln Q$. This indicates that the ZFs not only respond to changes of the radial mean turbulence level but also to local radial heat-flux corrugations. The residual of the parallel stress average also exhibits a feature where the heat-flux gradient is located but the proportionality to $\partial_x \ln Q$ is not nearly as good as for the perpendicular stress. One reason is that the parallel stress is much more dominated by random fluctuations in regions of small shearing-rates, which is here the case in the region where the heat-flux gradient is located.

For the purpose of rescaling one can also use other turbulence intensity measures like the square of the density fluctuations because it also increases in regions of small shearing-rates. But to approximate the stress residual of the time-average this quantity proved inadequate and therefore the heat-flux is the better choice for the second degree of freedom (Fig. 5.4b). These two degrees of freedom, the shearing-rate and the heat-flux, proved to be sufficient to construct a stress response functional describing all observed deterministic ZF features. This is a huge improvement because it makes the ZF evolution much more comprehensible than a description with a large number of degrees of freedom, e.g. the full turbulence equations.

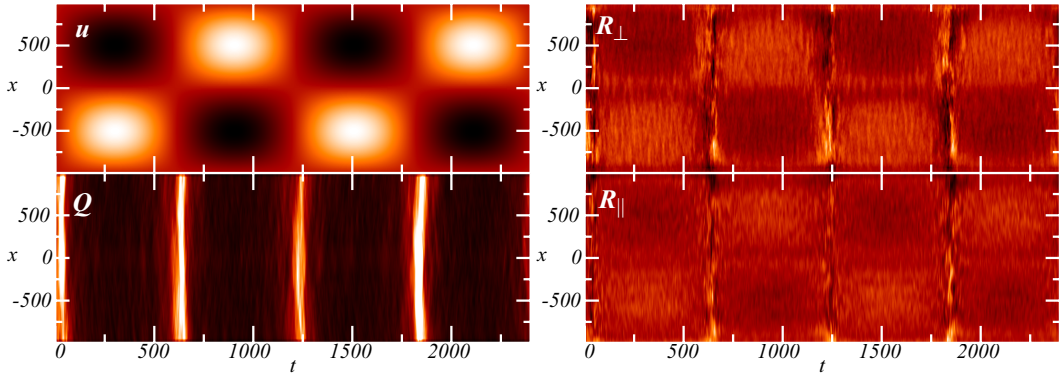

(a) (b)

Figure 5.3: (a) Time-evolution of the artificial shearing-rate $u = 0.2 \sin(2\pi x/L_x) \sin(2\pi t/1200)$ (top) and the radial heat-flux Q (bottom). (b) Corresponding perpendicular $R_\perp$ (top) and parallel $R_\parallel$ (bottom) stress. Comparison shows that Q,$R_\perp$,$R_\parallel$ increase where u becomes small.

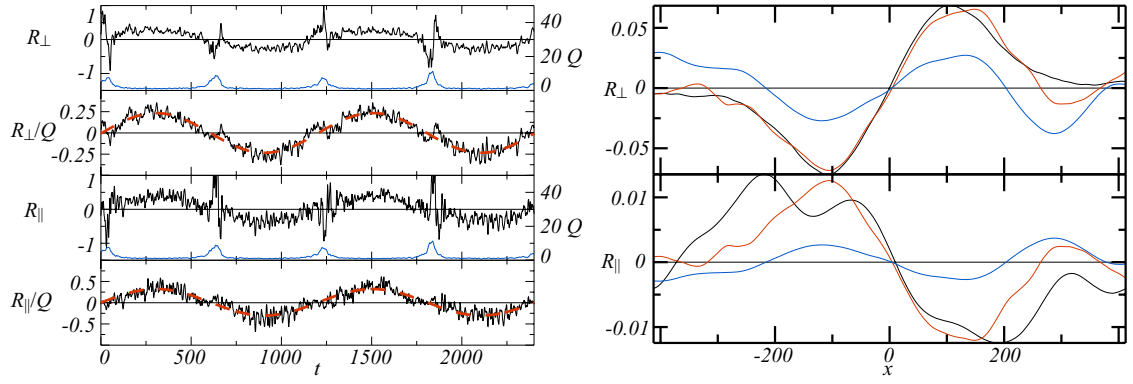

(a) (b)

Figure 5.4: (a) Time traces at $x = -500$ of the perpendicular stress $R_\perp$ (black) and the heat-flux (blue) (top), rescaled perpendicular stress $R_\perp/Q$ (black) and shearing-rate $\alpha_{0,\perp} u$ (red) (upper middle), parallel stress $R_\parallel$ (black) and the heat-flux (blue) (lower middle) and rescaled parallel stress $R_\parallel/Q$ (black) and shearing-rate $\alpha_{0,\parallel} u$ (red) (bottom). Comparison of the stresses rescaled by the heat-flux with the shearing-rate reveals that the rescaling is necessary to restore proportionality to the shearing-rate with coefficients $\alpha_{0,\perp}, \alpha_{0,\parallel}$ constant over time. (b) Radial profile of the average of $R_\perp/Q$ over two oscillations of u (black) and corresponding profile of $-\alpha_{4,\perp} \partial_x \ln Q$ (red) (top). Radial profile of the average of $R_\parallel/Q$ over two oscillations of u (black) and corresponding profile of $-\alpha_{4,\parallel} \partial_x \ln Q$ (red) (top) with coefficients $\alpha_{4,\perp}, \alpha_{4,\parallel} > 0$. In blue an approximation by the density fluctuation square gradient $\partial_x n^2$.

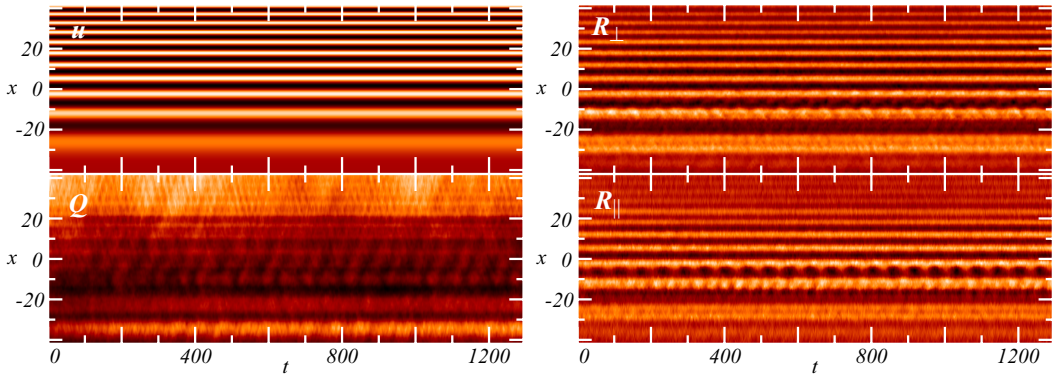

(a) (b)

Figure 5.5: (a) Time-evolution of the artificial shearing-rate $u = 0.125 \sin\left(2\pi(5 + 15(x + L_x/2)/L_x)x/L_x\right)$ (top) and the radial heat-flux Q (bottom). (b) Corresponding perpendicular $R_\perp/Q$ (top) and parallel $R_\parallel/Q$ (bottom) stress.

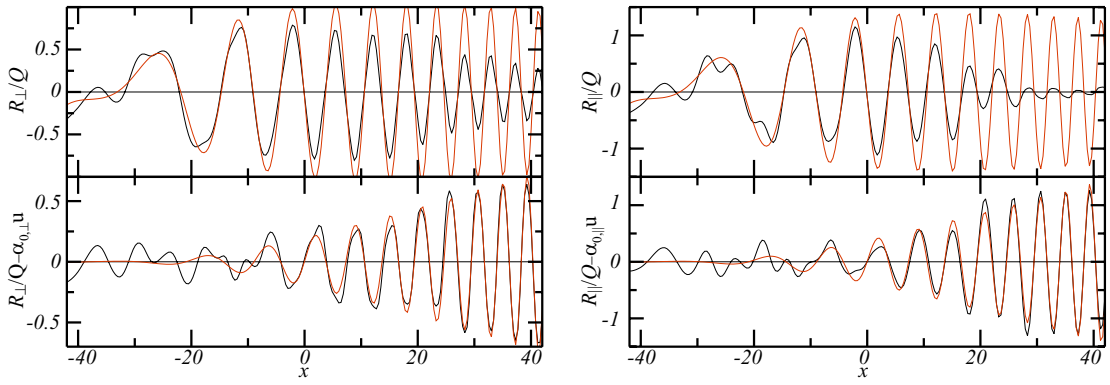

(a) (b)

Figure 5.6: (a) Perpendicular stress response $R_\perp/Q$ (black) and approximation by the shearing-rate u (red) (top), difference $R_\perp - \alpha_{0,\perp}u$ (black) and approximation by $\alpha_{2,\perp}\partial_x^2 u$ (red) (bottom). (b) Parallel stress response $R_\parallel/Q$ (black) and approximation by the shearing-rate u (red) (top), difference $R_\parallel - \alpha_{0,\parallel}u$ (black) and approximation by $\alpha_{2,\parallel}\partial_x^2 u$ (red) (bottom).

The robust characteristic radial scale length of the ZFs (recall Fig. 4.3a) suggests a radial wave-length dependence for the stress functional. A turbulence study with the parameters

$$L_x = 100 \quad L_y = 400 \quad \alpha = 0.5 \quad \epsilon_n = 1 \quad \tau = 1 \quad s = 1 \quad q = 1.5 \quad \eta_i = 2.4 \tag{5.3}$$

and a radially changing artificial shearing-rate $u = 0.125 \sin\left(2\pi(5 + 15(x + L_x/2)/L_x)x/L_x\right)$ shows the wave-length dependence of the heat-flux (Fig. 5.5a). In the region of high wave-numbers between $x = 20$ and $x = 40$ the heat-flux is much higher and seems less affected by the shear-flow, whereas for $x < 20$ the heat-flux is highly corrugated by the local shearing-rate although the amplitude does not change significantly. This illustrates again the dependence of the heat-flux on both shearing-rate amplitude and radial scale as discussed in chap. 4.
The pattern of the stresses (Fig. 5.5b) is still similar to the shearing-rate but the time-averaged radial profiles show (Figs. 5.6a and 5.6b) that the linear stress responses to u decrease with the wave-length. The profiles of the differences $R_\perp - \alpha_{0,\perp} u$ and $R_\parallel - \alpha_{0,\parallel} u$ clearly point towards a wave-number dependent coefficient for the shearing-rate. And it is identified that these differences are proportional to $\partial_x^2 u$, which is the lowest order derivative of the shearing-rate allowed by the symmetries of the turbulence equations (2.69).
The finite amplitude of ZFs observed in the self-consistent studies indicate a nonlinear saturation term for the stress functional. A turbulence study with the parameters

$$L_x = 200 \quad L_y = 400 \quad \alpha = 0.5 \quad \epsilon_n = 1 \quad \tau = 1 \quad s = 1 \quad q = 1.5 \quad \eta_i = 2.4 \tag{5.4}$$

and an artificial shearing-rate $u = 0.5 \sin\left(12\pi x/L_x\right)$ shows pronounced patterns in the stresses (Figs. 5.7a and 5.7b) that are very similar to the shearing-rate but have indentions near the extrema. The high amplitude of u also leads to strong corrugations in the heat-flux. For high enough amplitudes of u the shearing effect can even be strong enough to quench the turbulence locally such that only the peaks of the heat-flux corrugations remain. In the standard, self-consistent cases, however, it was observed that the ZFs saturate long before this effect can occur.
The radial time-averaged stress profiles (Figs. 5.8a and 5.8b), where the contribution from the heat-flux gradient is already subtracted, reveal a saturation of the stresses for both positive and negative shearing-rates. This points towards a saturation caused by a nonlinearity of u which is in phase with the shearing-rate. The term u^3 is the lowest order nonlinearity compliant with the turbulence equations symmetries (2.69) and it allows indeed a very good reconstruction of the differences $R_\perp/Q + \alpha_{4,\perp}\partial_x \ln Q - \alpha_{0,\perp} u$ and $R_\parallel/Q + \alpha_{4,\parallel}\partial_x \ln Q - \alpha_{0,\parallel} u$. The contributions to a total stress functional $R_t = R_\perp - R_\parallel$ identified so far yield

$$R_t = Q\left(\alpha_0 u - \alpha_1 u^3 + \alpha_2 \partial_x^2 u - \alpha_4 \partial_x \ln Q\right) \tag{5.5}$$

which leads to a ZF momentum balance of

$$\begin{aligned} \partial_t \bar{v}_y &= -\partial_x R_t / \left(1 + 2q^2\right) \\ &= -\partial_x \left[Q\left(\alpha_0 u - \alpha_1 u^3 + \alpha_2 \partial_x^2 u - \alpha_4 \partial_x \ln Q\right)\right] / \left(1 + 2q^2\right) . \end{aligned} \tag{5.6}$$

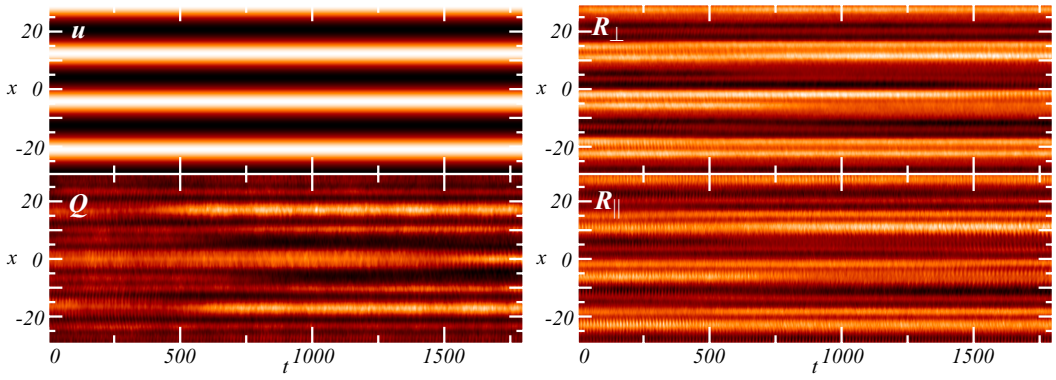

(a) (b)

Figure 5.7: (a) Time-evolution of the artificial shearing-rate $u = 0.5 \sin(12\pi x/lx)$ (top) and the radial heat-flux Q (bottom). (b) Corresponding perpendicular $R_\perp/Q$ (top) and parallel $R_\parallel/Q$ (bottom) stress.

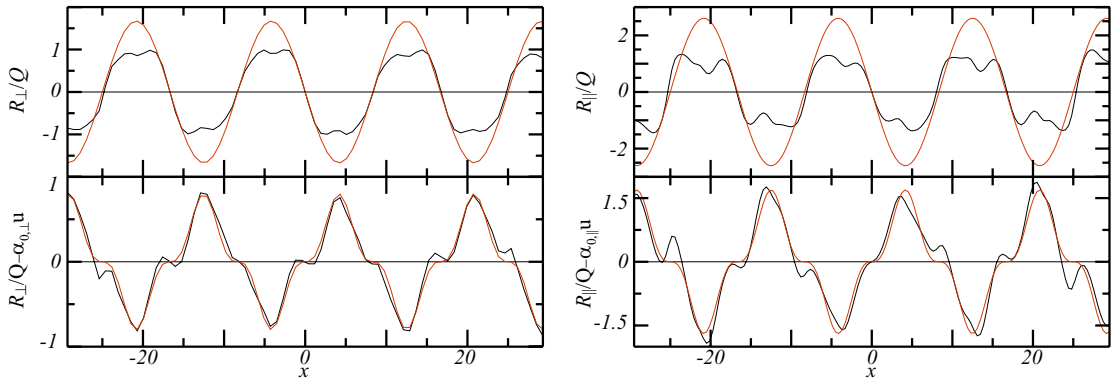

(a) (b)

Figure 5.8: (a) Profile of $R_\perp/Q + \alpha_{4,\perp}\partial_x \ln Q$ (black) and approximation by the shearing-rate $\alpha_{0,\perp}u$ (red) (top), $R_\perp/Q + \alpha_{4,\perp}\partial_x \ln Q - \alpha_{0,\perp}u$ (black) and approximation by $\alpha_{1,\perp}u^3$ (red) (bottom). (b) Profile of $R_\parallel/Q + \alpha_{4,\parallel}\partial_x \ln Q$ (black) and approximation by the shearing-rate $\alpha_{0,\parallel}u$ (red) (top), $R_\parallel/Q + \alpha_{4,\parallel}\partial_x \ln Q - \alpha_{0,\parallel}u$ (black) and approximation by $\alpha_{1,\parallel}u^3$ (red) (bottom).

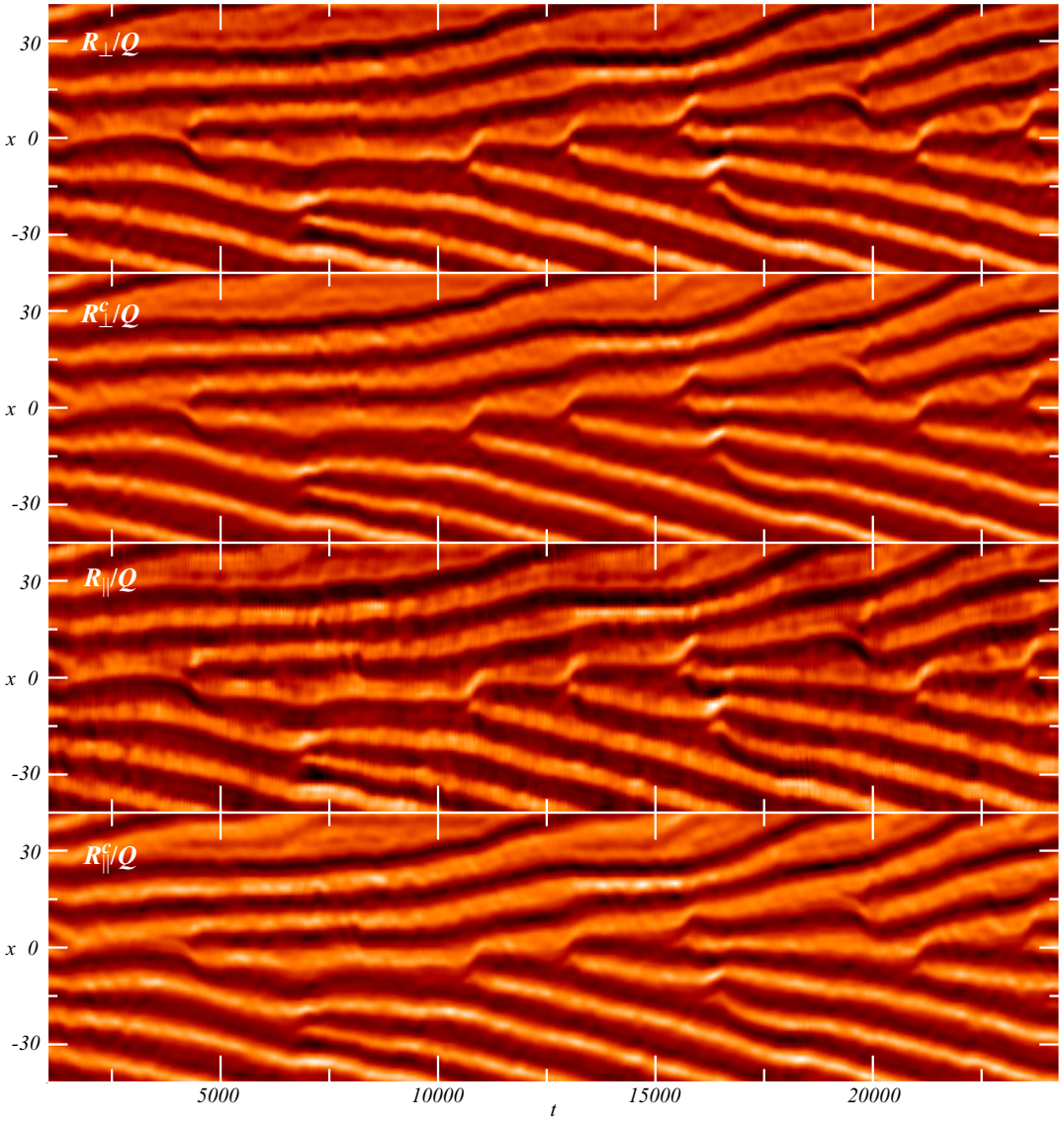

Figure 5.9: Time-evolution of the rescaled perpendicular stress $R_\perp/Q$ (top) and corresponding reconstruction $R^c_\perp/Q$ by Eq. (5.5) (upper middle), and time-evolution of the rescaled parallel stress $R_\parallel/Q$ (bottom middle) and corresponding reconstruction $R^c_\parallel/Q$ by Eq. (5.5) that accompany the flow pattern in Fig. 4.5a.

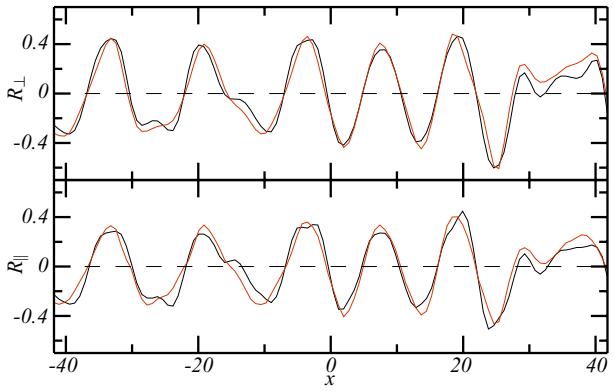

Figure 5.10: Top: Rescaled perpendicular stress $R_\perp/Q$ (black) at $t = 5000$ of Fig. 5.9 and reconstruction according to Eq. (5.5) (red). Bottom: Rescaled parallel stress $R_\parallel/Q$ (black) at $t = 5000$ of Fig. 5.9 and reconstruction according to Eq. (5.5) (red).

Figure 5.9 shows the perpendicular and parallel stresses, which accompany the flow pattern of figure 4.5a, and the reconstruction by Eq. (5.5) of the stresses using the corresponding shearing-rate and heat-flux patterns. Comparison of the patterns yields a very good match between the stresses and their reconstruction as all major features observable in the stresses are reproduced. The comparison of the instantaneous stresses at $t = 5000$ with their reconstruction (Fig. 5.10) exemplifies how well the functional (5.5) approximates the stresses for an appropriate set of coefficients.

In self-consistent studies with almost completely stationary flows (e.g. Fig. 4.3a) the heat-flux fluctuates randomly around some mean value but does not exhibit significant deterministic changes in the ZF-turbulence equilibrium state. A flow that is slightly artificially changed is restored to the self-consistent pattern much faster than the turbulence can adjust to changes of the ZF. This suggests that the intrinsic mechanism that restores the radial ZF scale is contained in the stresses dependence on the shearing-rate. A numerical solution of (5.6), while assuming a constant Q, should therefore yield a ZF pattern with a characteristic scale length.

Figure 5.11 shows the stable stationary solutions of the ZF momentum (5.6) with an initial state $\bar{v}_y = e^{\cos(x)} \sin(x)$ for different values of α_2 and periodic boundary conditions. The initial state always decays into the largest mode that fits into the domain. Intermediate states of the time-evolution may appear stationary and stable to perturbations for some time but eventually decay into the largest mode. The largest mode is stable unless a perturbation shifts the flow such that it becomes either positive or negative over the entire domain in which case the final state is a constant. Changing α_1 results in different final amplitudes, changing the relation between α_0 and α_2 yields different curvatures of the flow profiles and a change of the domain size just leads to a different scale length for the largest mode. This indicates that the functional (5.5) is still missing the necessary ingredient to describe the robust, characteristic ZF scale length.

The reason for the decay can be understood using a mean-field theory approximation of

the nonlinear term, $\partial_x u^3 \approx 3\left\langle u^2\right\rangle_x$, where $\langle\ldots\rangle_x$ denotes the radial average over several full flow oscillations, and assuming a constant heat-flux. This allows an estimate of the corresponding ZF growth rate

$$\Gamma_o = \langle Q\rangle_x K_x^2\left(\alpha_0 - 3\alpha_1\left\langle u^2\right\rangle_x - \alpha_2 K_x^2\right) . \tag{5.7}$$

The region where $\Gamma_o > 0$ is $0 < K_x < K_{x,h}$ with the largest wave-number $K_{x,h} = \sqrt{\alpha_0 - 3\alpha_1\left\langle u^2\right\rangle_x}/\sqrt{\alpha_2}$. The schematic 5.12a shows the evolution of Γ_o with respect to $\left\langle u^2\right\rangle_x$. Initially, $\left\langle u^2\right\rangle_x = 0$, all modes between $0 < K_x < K_{x,h} = K_{x,i} \equiv \sqrt{\alpha_0/\alpha_2}$ grow. When $\left\langle u^2\right\rangle_x$ increases $K_{x,h}$ decreases, confining the region of growth from the large K_x side until it reaches zero, explaining the eventual ZF decay except for the largest possible scale length shown in figure 5.11. For values $\left\langle u^2\right\rangle_x > \alpha_0/3\alpha_1$ all modes except $K_x = 0$ are damped since $\Gamma_o/K_x^2 < 0$ everywhere (Fig. 5.12a).
The self-consistent ZF behavior (Fig. 4.3a) suggests though that small and large K_x are damped while intermediate K_x continue to grow until the system saturates at a finite K_x and a finite amplitude. Hence, at least one additional wave-number dependent term is required for the growth rate:

$$\Gamma = \langle Q\rangle_x K_x^2\left(\alpha_0 - 3\alpha_1\left\langle u^2\right\rangle_x + \alpha_2 K_x^2 - \alpha_3 K_x^4\right) \tag{5.8}$$

Now, for $\left\langle u^2\right\rangle_x < 1/3\alpha_1$ all modes up to $K_{x,h}$ grow but in contrast to the growth rate (5.7) this formula confines the region of growth to $0 < K_{x,l} < K_x < K_{x,h}$ for shearing-rates $\left\langle u^2\right\rangle_x > 1/3\alpha_1$ with

$$K_{x,l} = \left[\left(\alpha_2 - \sqrt{\alpha_2^2 + 4\alpha_0\alpha_3\left(1 - 3\alpha_1\left\langle u^2\right\rangle_x\right)}\right)/2\alpha_3\right]^{1/2} \tag{5.9}$$

$$K_{x,h} = \left[\left(\alpha_2 + \sqrt{\alpha_2^2 + 4\alpha_0\alpha_3\left(1 - 3\alpha_1\left\langle u^2\right\rangle_x\right)}\right)/2\alpha_3\right]^{1/2} . \tag{5.10}$$

Since $K_{x,l}$ increases and $K_{x,h}$ decreases with the shearing-rate, the system saturates at $K_{x,s} \equiv K_{x,l} = K_{x,h} = \sqrt{\alpha_2/2\alpha_3}$ for $\left\langle u_s^2\right\rangle_x = \left(\alpha_2^2 + 4\alpha_0\alpha_3\right)/12\alpha_0\alpha_1\alpha_3$. The schematic 5.12b illustrates how the growth rate for large scales "dips" below zero for sufficiently high shearing-rates while intermediate scales continue to grow until saturation with a characteristic scale length is achieved. Any further increase of the shearing-rate results in a damping over all scales until $\left\langle u^2\right\rangle_x$ is again small enough such that $\Gamma(K_{x,s}) = 0$ is restored. Hence, this growth rate formula describes a robust scale formation mechanism with a scale length dependent on the relation of α_2/α_3 in contrast to 5.12a which accommodated only the largest possible scale length as a final state. The corresponding ZF momentum equation is

$$\begin{aligned}\partial_t \bar{v}_y &= -\partial_x R_t/\left(1 + 2q^2\right)\\ &= -\partial_x\left[Q\left(\alpha_0 u - \alpha_1 u^3 - \alpha_2\partial_x^2 u - \alpha_3\partial_x^4 u - \alpha_4\partial_x \ln Q\right)\right]/\left(1 + 2q^2\right) .\end{aligned} \tag{5.11}$$

Numerical solutions of (5.11) prove (Fig. 5.13) that the scale length of the final state is now dependent on the parameter relations which can always be adjusted to describe ZFs of arbitrary intrinsic radial scale lengths.

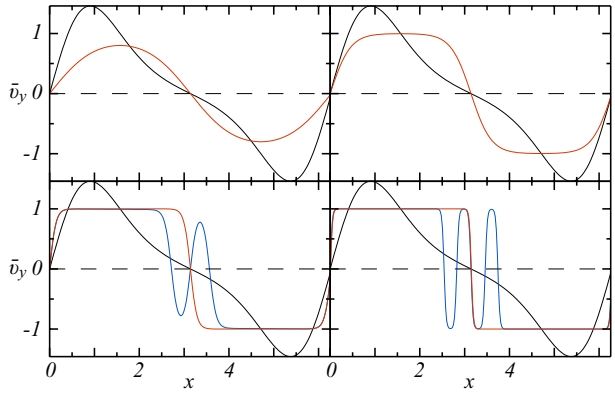

Figure 5.11: Numerical solution of Eq. (5.6) for $Q = 1, \alpha_0 = 1, \alpha_1 = 1, L_x = 2\pi$ and $\alpha_2 = 0.5$ (top left), $\alpha_2 = 0.1$ (top right), $\alpha_2 = 0.01$ (bottom left), $\alpha_2 = 0.001$ (bottom right). The initial states (black) decay into the stable final states (red) while some intermediate states (blue) may appear stable but are unstable to perturbations.

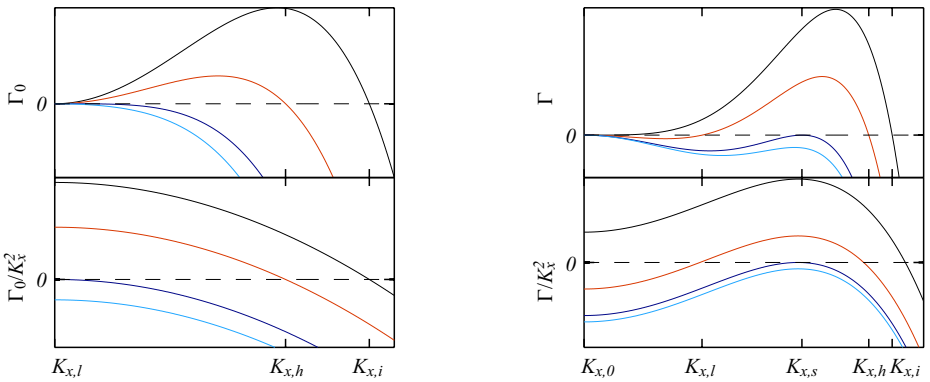

Figure 5.12: (a) Schematic behavior of Γ_o (top) and Γ_o/K_x^2 (bottom) for different values of $\langle u^2 \rangle_x = 0$ (black), $0 < \langle u^2 \rangle_x < \alpha_0/3\alpha_1$ (red), $\langle u^2 \rangle_x = \alpha_0/3\alpha_1$ (dark blue) and $\langle u^2 \rangle_x > \alpha_0/3\alpha_1$ (light blue) with region of $\Gamma_o > 0$ is $[0, K_{x,h}]$. (b) Schematic behavior of Γ (top) and Γ/K_x^2 (bottom) for different values of $\langle u^2 \rangle_x = 0$ (black), $0 < \langle u^2 \rangle_x < \langle u_s^2 \rangle_x$ (red), $\langle u_s^2 \rangle_x = \left(\alpha_2^2 + 4\alpha_0\alpha_3\right)/12\alpha_0\alpha_1\alpha_3$ (dark blue) and $\langle u^2 \rangle_x > \langle u_s^2 \rangle_x$ (light blue) with region of $\Gamma > 0$ is $[K_{x,l}, K_{x,h}]$.

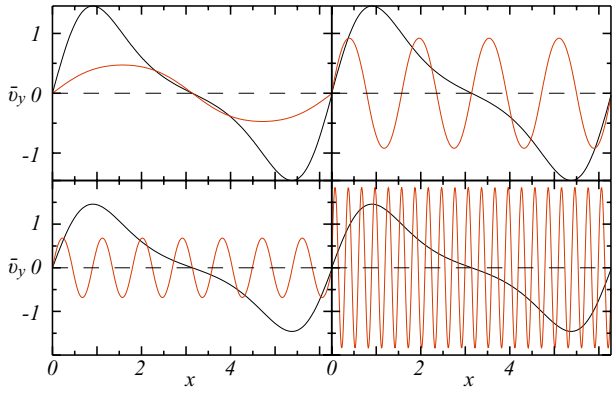

Figure 5.13: Numerical solution of Eq. (5.11) for $Q = 1, \alpha_0 = 1, \alpha_1 = 10, L_x = 2\pi$ and $\alpha_2 = -1, \alpha_3 = 0.25$ (top left), $\alpha_2 = -0.1, \alpha_3 = 0.01$ (top right), $\alpha_2 = -0.1, \alpha_3 = 10^{-3}$ (bottom left), $\alpha_2 = -0.1, \alpha_3 = 10^{-4}$ (bottom right). The initial states (black) decay into the stable final states (red).

To validate whether the $\partial_x^4 u$-term is indeed an adequate one for the stress functional it must be verified also by the turbulence studies. Constructing a case where the effect is dominant enough to be measured with a least-squares fit was not feasible since the method cannot robustly extract all the coefficients for the polynomial K_x-dependence of the shearing-rate coefficient.
Therefore, turbulence studies with artificial flows are used to verify that the behavior of Γ/K_x^2 (Fig. 5.12b) can be observed for the ZFs. A flow with a shearing-rate u_p is used to set up an initial state with a turbulence level close to the self-consistent equilibrium. This state is further modified by superimposing flows with shearing-rates u_s of different radial scale lengths, such that the total shearing-rate $u = u_p + u_s$. The amplitudes are chosen such that $u_s \ll u_p$ because the nonlinear term in Γ then evaluates to

$$\langle u^2 \rangle_x = \left\langle (u_p + u_s)^2 \right\rangle_x \approx \langle u_p^2 \rangle_x \ . \tag{5.12}$$

To validate the functional the stress response $\alpha_{0,s}$ caused by u_s, which represents the growth rate modulo K_x^2 for the small perturbation u_s, has to be measured and compared with the growth rate estimate

$$\Gamma(u_s) = \langle Q \rangle_x K_x^2 \left(\alpha_0 - 3\alpha_1 \langle u_p^2 \rangle_x + \alpha_2 K_x^2 - \alpha_3 K_x^4 \right) \ . \tag{5.13}$$

5.2 Verification of the Extended Stress Response Functional

To robustly extract the deterministic stress contributions of small perturbatory flows a new analysis procedure is discussed in the following.
Let the stress response in the turbulence studies with n_x radial grid points be represented by a vector $\mathbf{Z} \in \mathbb{R}^{n_x}$. In general $\mathbf{Z}$ is a linear combination of the n_x unit base vectors $\hat{e}_i$ ($\hat{e}_i \in \mathbb{R}^{n_x}$ with the value 1 at the index i and zero otherwise). The observations in the

previous chapter show that large deterministic parts of the response are caused by terms corresponding to a few specific linear combinations $\mathbf{P}_i$ of the unit vectors, e.g. $\mathbf{P}_0 \equiv u$. This suggests that a decomposition of $\mathbf{Z}$ exists

$$\mathbf{Z} = \sum_i \alpha_i \mathbf{P}_i + \sum_j \beta_j \mathbf{N}_j + \mathbf{n}\,. \tag{5.14}$$

where the coefficients α_i correspond to those of the constructed stress functional. The vectors $\mathbf{N}_j$ represent other deterministic stress contributions (e.g. boundary or resonant surface effects) and their structure must be determined individually from observations in turbulence studies. The remaining random fluctuations are represented by the noise vector $\mathbf{n}$, which is assumed to be white noise in the following. The coefficients $\alpha_i, \beta_i \in \mathbb{R}$ are the deterministic contributions one is interested in. Let $\mathbf{P}_0$ be the contribution of interest, e.g. u_s, then a test vector $\mathbf{d}$ satisfying

$$\mathbf{d} \cdot \mathbf{P}_0 = 1 \tag{5.15}$$

and zero otherwise would yield the coefficient $\mathbf{d} \cdot \mathbf{Z} = \alpha_0$. However, orthogonality of all contributions is generally not the case and distinguishing two vectors which are almost collinear is difficult, due to the finite support n_x and distortion by random fluctuations. Hence, a test vector with the aforementioned properties cannot always be constructed. A solution $\mathbf{d}$ that minimizes the variance with respect to $\mathbf{Z}$ under the constraint (5.15), however, is always possible

$$\mathrm{var}(\mathbf{d} \cdot \mathbf{Z}) = \mathbf{d}^T \cdot C(\mathbf{Z}) \cdot \mathbf{d} \to \min\,, \tag{5.16}$$

where C is the covariance matrix. The solution is (derived by application of the Lagrange multiplier method)

$$\mathbf{d} \equiv \frac{C^{-1} \cdot \mathbf{P}_0}{\mathbf{P}_0^T \cdot C \cdot \mathbf{P}_0} \tag{5.17}$$

and the variance is $\mathrm{var}(\mathbf{d} \cdot \mathbf{Z}) = 1/(\mathbf{P}_0^T \cdot C \cdot \mathbf{P}_0)$. To find the covariance matrix an initial estimate is made

$$C = v_{bg}\mathbb{I} + \sum_i v_{i,P} \hat{\mathbf{P}}_i \hat{\mathbf{P}}_i^T + \sum_j v_{j,N} \hat{\mathbf{N}}_j \hat{\mathbf{N}}_j^T \tag{5.18}$$

where v_{bg} is the background variance estimated from the random fluctuations observed in turbulence studies and $v_{i,P}$ and $v_{j,N}$ are "a priori" variance estimates for the contributions by $\hat{\mathbf{P}}_i = \mathbf{P}_i/|\mathbf{P}_i|$ and $\hat{\mathbf{N}}_j = \mathbf{N}_j/|\mathbf{N}_j|$, estimated from the square amplitudes of stress responses in a large ensemble of turbulence studies employing artificial flows. The values of $v_{i,P}$ and $v_{j,N}$ are then iteratively refined using the variances $\mathrm{var}(\mathbf{d}_i \cdot \mathbf{Z}) = 1/(\mathbf{P}_i^T \cdot C \cdot \mathbf{P}_i)$ and $\mathrm{var}(\mathbf{d}_j \cdot \mathbf{Z}) = 1/(\mathbf{N}_j^T \cdot C \cdot \mathbf{N}_j)$ to obtain a better estimate for C. The iteration is finished when the difference between the variance estimates and calculated variances in one iteration step becomes small.

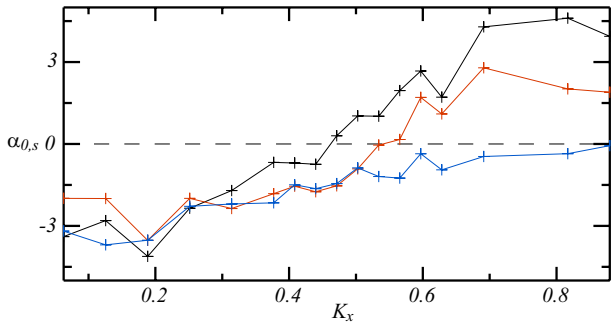

Figure 5.14: K_x-dependence of the stress response contribution $\alpha_{0,s}$ by the perturbatory shearing-rate u_s in a turbulence study with an artificial flow shear of $u = u_p + u_s$ where $u_p = 0.1$ (black), $u_p = 0.12$ (red) and $u_p = 0.15$ (blue) and $u_s = 0.01 \sin(K_x x)$. Response is qualitatively equal to the prediction (5.8) thus verifying the $\partial_x^4 u$ term.

To limit the number of contributions $\mathbf{P}_i$, a shearing-rate $u_p = \text{const}$ was chosen for the setup to measure the growth rate of a perturbatory flow, described in the previous section. Otherwise the nonlinear stress response would also contain linear combinations of the wave-numbers of u_p and u_s, complicating the measurements, as one such combination might be close or equal to the wave-number of $\mathbf{P}_0 \equiv u_s$ itself, resulting in a large undesired variance. To measure its linear growth rate using $\mathbf{d}$ the shearing-rate u_s should be small compared to u_p but it must still yield a stress response that is larger than the standard deviation calculated using $\mathbf{d}$. This confounds measurements for small values of u_p as the measured contribution of u_s is then smaller than the deviation. Since very large shearing-rates are damped over the entire K_x range, only a small range of shearing-rate amplitudes remains where the "dip" of the growth rate for u_s is detectable. In addition, the shearing-rate u_p should also be in a regime where the influence of $\partial_x \ln Q$ is a minor effect, otherwise the contribution measurements of u_s in the scale range where $\partial_x \ln Q$ is dominant will have a high variance.
Fortunately the parameter set (5.1) has a range of shearing-rates $|u_p| \in [0.1, 0.15]$ where the K_x-dependence of the growth rate of u_s can be adequately measured. The measured K_x-dependence of the contributions from u_s are shown in figure 5.14 for primary shearing-rates $u_p = 0.1$, $u_p = 0.12$ and $u_p = 0.15$. In this regime u_p itself is already damped as are the largest scales of u_s. The value of the wave-number $K_{x,l}$ that separates the growing from the damped scales increases when u_p is increased until all scales are damped. This is the same behavior as predicted by (5.8) and verifies that

$$R_t = Q\left(\alpha_0 u - \alpha_1 u^3 - \alpha_2 \partial_x^2 u - \alpha_3 \partial_x^4 u - \alpha_4 \partial_x \ln Q\right) , \tag{5.19}$$

indeed describes the stress response behavior, including and reproducing the major features observed in the ZF-turbulence studies, in particular excitation, characteristic radial scale length and finite saturation.

Chapter 6

Wave-kinetic Analogies

This chapter is dedicated to the derivation of a Reynolds-stress functional for ITG-turbulence within a wave-kinetic framework (Sec. 6.1), even though the prerequisite of a scale separation between ZFs and turbulence is not strictly fulfilled (see chap. 4). This allows a comparison of the properties of the wave-kinetically derived stress description with the functional constructed in chapter 5 which points out a crucial ingredient missing in previous, wave-kinetics based ZF theories (Sec. 6.2).

6.1 A Wave-kinetic Stress Functional Derivation

To describe the interaction of turbulence with large scale shear-flows, the small scale fluctuations are thought of as wave-packets within a wave-kinetic framework with a wave-action $N_{\mathbf{k}} \equiv n\left(k\right)\left|\phi_{\mathbf{k}}\right|^2$ which is proportional to the square of the wave amplitude [98, 99, 100], where $n\left(k\right) > 0$ is a coefficient that is symmetric with respect to $\mathbf{k}$. In terms of quantum mechanics $N_{\mathbf{k}}$ can be interpreted as the occupation number for an energy state $\omega_{\mathbf{k}}$. The wave-packet is localized at $\mathbf{x}$ and has a wave-number $\mathbf{k}$, hence the wave-action is a function of both, $N_{\mathbf{k}}\left(\mathbf{x},\mathbf{k}\right)$. The frequency of the wave-packet is

$$\omega = \omega_{\mathbf{k}}(\mathbf{k}) + \mathbf{k}\cdot\bar{\mathbf{v}}\left(\mathbf{x}\right) \tag{6.1}$$

where $\bar{\mathbf{v}}$ is the convecting flow, in this case the ZF, and $\omega_{\mathbf{k}}$ is the frequency of the wave in the convected frame. It is assumed that the convecting flow is changing only very slowly over time compared to changes in the wave-action such that $\mathrm{d}\omega/\mathrm{d}t = 0$. The wave-action can change in time either due to convection by the shear-flow $\nabla_{\mathbf{x}}\cdot\left(\mathbf{V}N_{\mathbf{k}}\right)$, where $\mathbf{V} \equiv \nabla_{\mathbf{k}}\omega$, or due to a change in the wave-number caused by a convection in phase space $\nabla_{\mathbf{k}}\cdot\left(N_{\mathbf{k}}\mathrm{d}\mathbf{k}/\mathrm{d}t\right)$ or by collisions of wave-packets $C\left(N_{\mathbf{k}}\right)$. The time-evolution of the wave-action is [34, 52]

$$\partial_t N_{\mathbf{k}} + \nabla_{\mathbf{x}}\cdot\left(\mathbf{V}N_{\mathbf{k}}\right) + \nabla_{\mathbf{k}}\cdot\left(N_{\mathbf{k}}\mathrm{d}\mathbf{k}/\mathrm{d}t\right) = C\left(N_{\mathbf{k}}\right)\,. \tag{6.2}$$

The change of the wave-number in a shear-flow according to (3.36) is $\mathrm{d}\mathbf{k}/\mathrm{d}t = -\nabla_{\mathbf{x}}\omega$ resulting in the wave-kinetic equation

$$\partial_t N_{\mathbf{k}} + \nabla_{\mathbf{k}}\omega\cdot\nabla_{\mathbf{x}}N_{\mathbf{k}} - \nabla_{\mathbf{x}}\omega\cdot\nabla_{\mathbf{k}}N_{\mathbf{k}} = C\left(N_{\mathbf{k}}\right)\,. \tag{6.3}$$

Let $N_{\mathbf{k},0}$ be the ZF-turbulence equilibrium state of the wave-action, then the Krook-type "collisional"-term $C(N_{\mathbf{k}}) = \Delta\omega(N_{\mathbf{k},0} - N_{\mathbf{k}})$ (others also readily available e.g. Focker-Planck) describes the tendency of $N_{\mathbf{k}}$ to evolve into the equilibrium with a decorrelation rate $\Delta\omega > 0$.
Neglecting, for simplicity, the diamagnetic contribution (which is in the examined parameters regime proportional to $\langle v_x v_y \rangle_{y,z}$ (see Chap. 4)) the perpendicular stress defined by (4.14) yields

$$R_\perp \approx \langle v_x v_y \rangle_{y,z} = -\langle \partial_y \phi \partial_x \phi \rangle_{y,z} . \tag{6.4}$$

Applying a Fourier transform in the y and z directions to each fluctuation gives

$$R_\perp = \langle \int \mathrm{d}k_1^2 \int \mathrm{d}k_2^2 k_{1,x} k_{2,y} \phi_{1,k_1} \phi_{2,k_2} e^{\imath(\mathbf{k}_1+\mathbf{k}_2)\cdot\mathbf{x}} \rangle_{y,z} \tag{6.5}$$

which results in

$$\begin{aligned} R_\perp &= -\langle \int \mathrm{d}k^2 k_x k_y |\phi_{\mathbf{k}}|^2 \rangle_{y,z} \\ &= -\langle \int \mathrm{d}k^2 \pi_k N_{\mathbf{k}} \rangle_{y,z} \end{aligned} \tag{6.6}$$

[for DWs $n(k) = \left(1 + \alpha^2 \epsilon_n k_\perp^2\right)^2$ [53, 52, 34, 95]; for ITGs $n(k) = 4\gamma_k^2 / \left(\Delta_k^2 + \gamma_k^2\right)$ with $\gamma_k = \sqrt{k_y \alpha \omega_{\boldsymbol{\kappa}} \tau (\eta_i - \eta_{ic})}$ and $\Delta_k = (10 - 3\tau)\omega_{\boldsymbol{\kappa}}/6 + \tau\alpha k_y/2$ where η_{ic} is the linear ITG-instability threshold [67, 68]] and $\pi_k \equiv k_x k_y / n(k)$. Assuming that the wave-action is proportional to the turbulence intensity $N_{\mathbf{k}} \propto Q$ and $\partial_x N_{\mathbf{k},0} \approx N_{\mathbf{k},0} \partial_x Q / Q$, one can apply a perturbative expansion to $N_{\mathbf{k}} = N_{\mathbf{k},0} + N_{\mathbf{k}}^1 + N_{\mathbf{k}}^2 + \ldots$ in terms of powers of the shearing rate $u^m \equiv (\partial_x \bar{\mathbf{v}})^m$, derivatives of the shearing rate $K_x^n u \equiv \partial_x^n u$ $(m, n \in \mathbb{N})$, $\partial_x \ln Q$ and further higher order terms obeying the turbulence equation symmetries to approximate a solution of (6.3) required for a stress estimation using (6.6). It is further assumed that $\partial_t \ll \Delta\omega$ and $\Delta\omega$ is symmetric with respect to k.
The lowest order $(m, n) = (1, 0)$ deviation of $N_{\mathbf{k}}$ from $N_{\mathbf{k},0}$ is thus given by

$$\begin{aligned} N_{\mathbf{k}}^1 &= \frac{-1}{\Delta\omega} \left[\upsilon_{gx} \partial_x N_{\mathbf{k},0} - k_y u \partial_{k_x} N_{\mathbf{k},0} \right] \\ &= \frac{-1}{\Delta\omega} \left[\upsilon_{gx} N_{\mathbf{k},0} \partial_x \ln Q - k_y u \partial_{k_x} N_{\mathbf{k},0} \right] \end{aligned} \tag{6.7}$$

for a group velocity $\upsilon_{gx} \equiv \partial_{k_x} \omega$ and a flow $\mathbf{k} \cdot \bar{\mathbf{v}} = k_y \bar{v}_y$. Inserted into (6.6) and partially integrated, the coefficients α_0^{wk} and α_4^{wk} for the terms u and $\partial_x \ln Q$ in the perpendicular stress are

$$\alpha_0^{\mathrm{wk}} = \langle \partial_{k_x} \left[\pi_k k_y / \Delta\omega \right] \rangle_k \tag{6.8}$$

$$\alpha_4^{\mathrm{wk}} = -\langle \pi_k \upsilon_{gx} / \Delta\omega \rangle_k \tag{6.9}$$

where the superscript wk denotes their wave-kinetic origin. The subscripts are chosen such that they correspond with the numbering in the functional

$$R_t = Q \left(\alpha_0 u - \alpha_1 u^3 - \alpha_2 \partial_x^2 u - \alpha_3 \partial_x^4 u - \alpha_4 \partial_x \ln Q \right) \tag{6.10}$$

that was constructed and verified in chapter 5. The average operator for a quantity A is defined as

$$\langle A \rangle_k \equiv \int \mathrm{d}k^2 A \langle N_{\mathbf{k},0} \rangle_{y,z} / Q \,. \tag{6.11}$$

The coefficient α_0^{wk} describes the linear ZF growth and is generally not vanishing if $\partial_{k_x} \pi_k k_y$ and $N_{\mathbf{k},0}$ are symmetric functions with respect to k_x. $\pi_k v_{gx}$ on the other hand may be asymmetric with respect to k_x depending on the wave-number behavior of v_{gx} and thus may vanish. The perpendicular stress in the lowest order is

$$R_\perp^1 = Q \left[\alpha_0^{\mathrm{wk}} u + \alpha_4^{\mathrm{wk}} \partial_x \ln Q \right] . \tag{6.12}$$

Higher order terms of $N_{\mathbf{k}}$ are easily obtained iteratively from the wave-kinetic equation (6.3)

$$N_{\mathbf{k}}^j = \frac{-1}{\Delta\omega} \left[v_{gx} \partial_x N_{\mathbf{k}}^{j-1} - k_y u \partial_{k_x} N_{\mathbf{k}}^{j-1} \right] . \tag{6.13}$$

It is important to note though that the coefficients including an $N_{\mathbf{k}}^j$ with an even j are zero [54] which is consistent with the invariance (2.69) of the turbulence equations as terms like $\partial_x u$ are prohibited. Iteration up to $j = 5$ and insertion into (6.6) reproduces, among others, all the terms observed in chapter 5. The coefficients corresponding to the terms $\partial_x^2 u$ and $\partial_x^4 u$ are

$$\alpha_2^{\mathrm{wk}} = \left\langle \partial_{k_x} \left[\pi_k k_y v_{gx}^2 / \Delta\omega^3 \right] \right\rangle_k \tag{6.14}$$

$$\alpha_3^{\mathrm{wk}} = \left\langle \partial_{k_x} \left[\pi_k k_y v_{gx}^4 / \Delta\omega^5 \right] \right\rangle_k \tag{6.15}$$

which are generally non-vanishing. The coefficient for the nonlinear term u^3 is

$$\alpha_1^{\mathrm{wk}} = - \left\langle k_y^3 \partial_{k_x}^3 \pi_k / \Delta\omega^3 \right\rangle_k \tag{6.16}$$

which is finite if $k_y^3 \partial_{k_x}^3 \pi_k$ is a symmetric function with respect to k_x. The coefficient of u^2 vanishes due to the turbulence equation symmetries and u^3 is therefore the lowest order non-vanishing nonlinearity with $m = 0$. The signs of α_2^{wk} and α_1^{wk} concur with the measurements for the perpendicular stress (Figs. 5.6a and 5.8a) if the $\langle \ldots \rangle_k$ operation yields a non negative value, which will be addressed section 6.2. The first generally non-vanishing term quadratic in u is $\partial_x u^2$ with a coefficient

$$\alpha_5^{\mathrm{wk}} = \frac{1}{4} \left\langle \partial_{k_x} \left[\frac{1}{\Delta\omega} \left(3 \partial_{k_x} \left(k_y^2 \pi_k v_{gx} / \Delta\omega^2 \right) + k_y^2 \pi_k \partial_{k_x} v_{gx} / \Delta\omega^2 \right) \right] \right\rangle_k . \tag{6.17}$$

Overall this yields a perpendicular stress functional

$$R_\perp^{\mathrm{wk}} = Q \left[\alpha_0^{\mathrm{wk}} u + \alpha_1^{\mathrm{wk}} u^3 + \alpha_2^{\mathrm{wk}} \partial_x^2 u + \alpha_3^{\mathrm{wk}} \partial_x^4 u + \alpha_4^{\mathrm{wk}} \partial_x \ln Q + \alpha_5^{\mathrm{wk}} \partial_x u^2 \right] . \tag{6.18}$$

The formula contains the three lowest order linear terms and the lowest order quadratic and cubic terms that do not vanish in general. The other terms obtained by evaluating (6.13) up to $N_{\mathbf{k}}^5$ either vanish or are of even higher order.

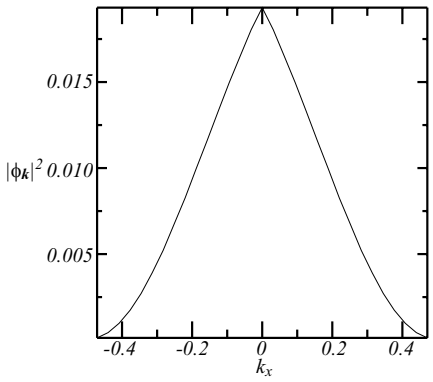

Figure 6.1: Spectrum of $|\phi_{\mathbf{k}}|^2$ on the outboard midplane for the dominant fluctuation at $k_y = 0.33$ in a self-consistent ZF-turbulence equilibrium state shown in figure 4.3a at $t = 1800$.

6.2 Comparison with the Constructed Functional

The wave-kinetic approach was used frequently in e.g. [52, 53, 54] to discuss the properties of the DW-driven ZFs with the functional (6.18) for the perpendicular stress without the terms $\alpha_3^{\mathrm{wk}}, \alpha_4^{\mathrm{wk}}$ and α_5^{wk}. Even though the parallel flow component carries the major part of the ZF energy [49], the parallel stress component was not really discussed in detail and the only retained influence of the parallel stress was a viscous parallel damping term $\mu_{\parallel}\left(1+2q^2\right)u$. This lead to a total stress functional of

$$\begin{aligned} R_t^{\mathrm{wk}} &= Q\left[\alpha_0^{\mathrm{wk}}u + \alpha_1^{\mathrm{wk}}u^3 + \alpha_2^{\mathrm{wk}}\partial_x^2 u - \mu_{\parallel}\left(1+2q^2\right)u\right] \\ &= Q\left[\alpha_{0,t}^{\mathrm{wk}}u + \alpha_1^{\mathrm{wk}}u^3 + \alpha_2^{\mathrm{wk}}\partial_x^2 u\right] \end{aligned} \tag{6.19}$$

where the retained parallel contribution results in a modification of the linear growth rate $\alpha_{0,t}^{\mathrm{wk}} \equiv \alpha_0^{\mathrm{wk}} - \mu_{\parallel}\left(1+2q^2\right)$. The mathematical structure of this functional is equal to that of (5.5). It was shown previously (Fig. 5.12a) that the only stable state described by this functional has the largest possible radial scale length. Hence, the functional (6.19) does not describe the characteristic radial scale length of ZFs. However, the wave-kinetic theory does provide the additional terms required for a stress description with a characteristic scale length as comparison of (6.18) and (6.10) shows. This is unsurprising as equation (6.13) can produce terms of arbitrary order in u^m and K_x^n. The question remains whether the wave-kinetic theory predicts the appropriate coefficient characteristics, most importantly the proper signs necessary for a saturation with a characteristic scale length.

The sign of α_0^{wk} (Eq. (6.8)) is positive if the integrand $k_x\partial_{k_x}N_{\mathbf{k},0} < 0$, which is the case for typical DW action [54]. In the case of ITG-turbulence the spectrum of $|\phi_{\mathbf{k}}|^2$ is centered around $k_x = 0$ (Fig. 6.1) and monotonically decreasing for $|k_x| \neq 0$, thus $k_x\partial_{k_x}N_{\mathbf{k},0} < 0$ yielding a positive coefficient α_0^{wk}.

The sign of the coefficient α_4^{wk} depends on the symmetries of the group velocity v_{gx}. In the case of DWs v_{gx} is asymmetric with respect to both perpendicular wave-numbers and

hence the coefficient is negative as $\pi_k v_{gx} > 0$. For ITGs the group velocity depends on the curvature frequency $\omega_{\boldsymbol{\kappa}}$ (see chap. 3) which changes the symmetries of the group velocity depending on the poloidal angle. In the examined case, though, $\pi_k v_{gx} > 0$ where the turbulence is located (see Fig. 3.4) – on the low-field side – such that $\alpha_4^{\mathrm{wk}} < 0$ (Eq. (6.9)). This matches the observations for the perpendicular stress in chapter 6.
The higher order terms in K_x^n linear in u differ from α_0^{wk} only in the even powers of the radial group velocity v_{gx} (Eq. (3.7)) and odd powers of the decorrelation rate $\Delta\omega$ (Eqs. (6.14) and (6.15)). Since $\Delta\omega$ is symmetric with respect to $\mathbf{k}$, the coefficients have the same condition for a positive sign as α_0^{wk} namely $k_x \partial_{k_x} N_{\mathbf{k},0} < 0$. Hence, the wave-kinetic theory predicts these coefficients to be positive. The positive sign of α_2^{wk} coincides with the measurements for the perpendicular stress in the turbulence studies (Fig. 5.6a). The theory does not, however, yield a proper sign prediction of the coefficient for the total stress which should be negative to reflect to early damping of large scale observed in the turbulence studies (see Eq. (5.11)). Furthermore, a positive coefficient α_3^{wk} for the total stress would predict a rapid growth of smallest scales also contrary to the observations. The observations of the stresses made in chapter 5 yielded that the parallel stress contributes significantly to the coefficients of all terms. This illustrates that a major ingredient missing in current wave-kinetic ZF descriptions is an adequate treatment of parallel dynamics.
The wave-kinetic coefficient α_1^{wk} for the third order nonlinear term is negative if $k_x \partial_{k_x}^3 N_{\mathbf{k},0}/n\,(k) < 0$. This is similar to the condition for the linear coefficient and is satisfied for DWs [54]. In the case of the ITG turbulence, however, the sign of α_1^{wk} is highly dependent on the structure of $n\,(k)$ and the poloidal location of the turbulence. A general statement on the sign is beyond the scope of this thesis. However, a non-negative sign would lead to indefinitely growing ZFs, which have not been observed.
The wave-kinetic approach for a stress functional also derives the quadratic term $\partial_x u^2$, which is not included in the functional (6.10) constructed from observations in turbulence studies because it could not be satisfyingly verified, since the corrugations of the heat-flux are proportional to it, $\partial_x \ln Q \sim \partial_x u^2$ (see Sec. 4.3).
Overall, the discussed wave-kinetic approach, which is the basis for contemporary ZF theories [52, 53, 54], can not predict the evolution of ZFs as most contributions of the parallel stress are not included in the derived functional leading to inadequate coefficients. Additionally, the derived coefficients should not be taken literally because the prerequisite of a separation of scales between ZFs and driving turbulence is not fulfilled (see Fig. 4.4).

Chapter 7

Conclusions

Zonal Flows (ZF) [7, 8, 9] are global structures self-excited by the turbulence in magnetized plasmas. Since their shearing effect on turbulent eddies [10] leads to a reduction in the radial transport of particles and heat in toroidally confined fusion plasmas, which can improve the confinement by several orders of magnitude [35, 36, 37], it is imperative to have a good understanding of the evolution of ZF-turbulence equilibrium states. The two-fluid code NLET [64] (briefly discussed in chapter 2) was used to examine the excitation and transition of ITG-driven ZFs into ZF-turbulence equilibria and their evolution.

Self-consistent turbulence studies revealed that strong ZFs, which are excited when the turbulence self-organizes itself and starts forming pronounced radial streamers, evolve into a nearly stationary pattern that tears the radial streamers apart resulting in a ZF-turbulence equilibrium with a nearly stationary radial heat-transport level which is orders of magnitude lower than in cases without ZFs (see Chap. 4). The radial scale length of the equilibrium ZFs is hereby different from the scale length of marginal flows, as excited by a turbulence exhibiting no formation of radial streamers, and even different from the scale length during the initial excitation phase of strong ZFs. ZF theories describing the excitation phase only, which covers only a short phase of the ZF evolution, are therefore unsuitable to make adequate predictions of the ZF-turbulence equilibrium.

Further turbulence studies revealed that states with arbitrary initial flows evolve self-consistently into ZF-turbulence equilibria with one robust and characteristic radial scale length for a given set of plasma parameters. Examination of the perpendicular and parallel Reynolds stresses corresponding to the flows yielded large deterministic contributions in the stress patterns which are clearly correlated with the flow. This suggested that the construction of a deterministic Reynolds stress response functional that describes all the characteristic ZF features observed in ZF-turbulence studies, namely a nearly stationary saturated ZF pattern maintaining a characteristic radial scale, is possible. The diamagnetic contribution to the perpendicular stress is of the same order as the $\mathbf{E} \times \mathbf{B}$ contribution and therefore can not be neglected. The ZF patterns of the two-fluid description are qualitatively equal to the patterns obtained with the gyro-kinetic code GYRO. This justifies the use of the two-fluid approach, which comes at a lower computational expense, and

made the extensive turbulence studies necessary to map out the requirements upon a stress functional possible feasible in the first place.
Examination of the stresses in self-consistent turbulence studies reveals that they are proportional to the shearing-rate u (Fig. 5.2). To identify additional contributions, the stress responses to artificial flow profiles were examined throughout chapter 5. The stress responses to oscillating large scale flows show large deviations from the proportionality to u in regions of small shearing-rates, accompanied by large increases of turbulence intensity, e.g. heat-flux Q or density fluctuation square. This motivated the use of the turbulence intensity as a second degree of freedom for the functional. Indeed, a rescaling of the stresses by the turbulence intensity restores the proportionality to the shearing-rate (Fig. 5.4a). A time-average of the rescaled stresses over several oscillation periods removes all contributions caused by the shearing-rate, and deterministic stress residuals proportional to the heat-flux gradient $\partial_x \ln Q$ are observed (Fig. 5.4b). The heat-flux is therefore the best choice for the turbulence intensity measure since this way two degrees of freedom will suffice. The identification of further terms was aided by the turbulence equations symmetries (2.69) that confine the domain of possible candidate terms.
The responses to a flow with a radially changing wave-number reveal a wave-length dependence of the stress responses. It was found that the residuals, after subtracting the contributions by u, are proportional to the second derivative of the shearing-rate $\partial_x^2 u$ (Fig. 5.6). The responses to a flow with a large amplitude show a finite saturation of the stresses identifying their proportionality to the nonlinearity u^3 (Fig. 5.8).
For appropriate coefficients a functional (Eq. 5.5) can be constructed, using the aforementioned contributions, that reproduces the stress patterns both qualitatively and quantitatively quite well for supplied self-consistent flow and heat-flux patterns (Figs. 5.9 and 5.10). However, numerical solutions with arbitrary initial states of the ZF momentum equation (5.6) induced by this functional always produce a flow pattern with the largest possible scale length (Fig. 5.11), contrary to the characteristic radial scale length observed in self-consistent studies. Using a mean-field approximation of the nonlinearity, an estimate of the ZF growth rate induced by the functional reveals a region of growth confined by $0 < K_x < K_{x,h}$ with a decreasing $K_{x,h}$ for an an increasing shearing-rate (Fig. 5.12a), which explains the decay of all but the largest flow scale length. The observations of the self-consistent ZF evolution are, though, that flows with large and small scale lengths are damped for a finite flow amplitude while flows of intermediate scale lengths continue to grow. This growth behavior is described by extending the functional with the term $\partial_x^4 u$ (Fig. 5.12b) resulting in a total stress functional

$$R_t = Q\left(\alpha_0 u - \alpha_1 u^3 - \alpha_2 \partial_x^2 u - \alpha_3 \partial_x^4 u - \alpha_4 \partial_x \ln Q\right) , \tag{7.1}$$

with coefficients $\alpha_i > 0$. Numerical solutions of the ZF momentum equation induced by this extended functional saturate into a profile with a characteristic scale length depending on the relations of the coefficients (Fig. 5.13).
Verification of the additional term in turbulence studies using standard analysis techniques, e.g. least-squares approximations, yield unsatisfactory results as the coefficients are highly susceptible to interfering noise, caused by random fluctuation remnants, and almost indistinguishably similar contributions by different terms. Hence, to verify the functional,

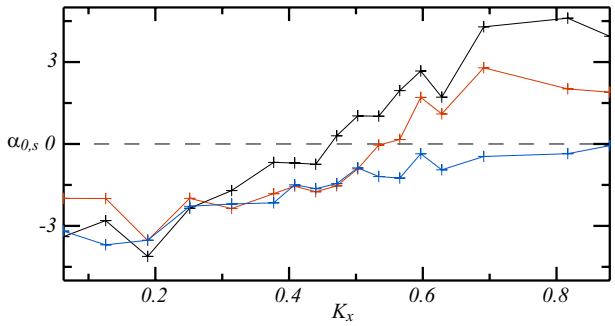

Figure 7.1: K_x-dependence of the stress response contribution $\alpha_{0,s}$ by the perturbatory shearing rate u_s in a turbulence study with an artificial flow shear of $u = u_p + u_s$ where $u_p = 0.1$ (black), $u_p = 0.12$ (red) and $u_p = 0.15$ (blue) and $u_s = 0.01 \sin(K_x x)$. Response is qualitatively equal to the prediction (5.8) thus verifying the $\partial_x^4 u$ term.

the growth rates of perturbations u_s to flows with constant shearing-rates were measured applying a minimal variance estimator. The covariance matrix needed to construct the estimator was initially obtained from observations of stress responses in a large ensemble of turbulence studies and subsequently iteratively refined. The measurements show (Fig. 7.1) that the region of growth of u_s is confined by $K_{x,l} < K_x < K_{x,h}$ with an increasing lower bound $K_{x,l}$ for an increasing shearing-rate, thus exhibiting the same properties as described by (7.1), which verifies the extended functional. This functional describes all the observed ZF features, namely excitation, finite saturation and characteristic radial scale of the ZF-turbulence equilibrium, and therefore permits the prediction of the time-evolution of ZFs, including their radial scale length.

Contemporary ZF equilibrium theories [52, 53, 54] derived a stress response functional analytically for drift-wave driven ZFs, using a wave-kinetic approach to obtain an expression for the perpendicular stress and taking the parallel stress contribution into account as a viscous modification of the linear ZF growth rate only. While this method can also be used for ITG-driven ZFs (see Chap. 6) and produces the same terms as observed in the stress responses, it gives coefficients with the wrong characteristics, most importantly the sign. Thus, it fails to predict the self-consistent ZF evolution, as do all contemporary wave-kinetic ZF theories. An adequate treatment of the contributions by the parallel stress to all coefficients is absolutely necessary to obtain a valid total stress functional. However, even though some wave-kinetic effects have been observed previously [57], coefficients derived using the wave-kinetic approach should not be taken literally, as a strict separation of scales, which is a requirement for the applicability of wave-kinetic theory, between the turbulence and the equilibrium ZFs is not fulfilled.

Knowledge about ZF activity is important as it is necessary for transport descriptions to take into account the amplitude as well as the radial scale length of the ZF shearing-rate, because the mean radial heat-flux level depends on both quantities, with a scale-length-dependent threshold for the shearing-rate below which the ZFs do not significantly influence the turbulence (see Sec. 4.3). The threshold is due to the fact that radially propagating

turbulent eddies passing quickly through regions with alternating flow directions are distorted but not torn apart. This is unless the shearing-rate amplitude is large enough to tear an eddy apart to such an extend that the radial streamer pattern collapses before it propagates to a region with an opposite flow direction. Furthermore, the turbulence retains some memory of the flow it was previously subjected to during transitions from one flow state to another and takes a comparatively long time to adjust.
Strong shear-flows can also cause corrugations in the heat-flux near local flow maxima and minima with $\partial_x \ln Q \sim \partial_x u^2$, which, self-consistently, will cause a response of the ZFs since their equilibrium state prefers vanishing deterministic heat-flux gradients. Additionally, in some regimes the corrugations show an asymmetric profile with respect to flows in ion- or electron-diamagnetic-drift direction which is due to differences in the heat-flux distributions along the field lines, indicating that a heat-flux description needs to take the third dimension into account. A transient wave-kinetic concentration of fluctuation energy [57], wave-trapping [97] or an increased drive of turbulence [95] may offer an explanation for the corrugations but a verification is left to future studies.
In summary, a Reynolds stress response functional for ZFs was derived that describes the excitation, evolution and robust characteristic radial scale length of ZFs [101]. Future studies on the plasma parameter dependencies of the functionals coefficients will yield a reliable map of ZF activity, which can then be incorporated into an advanced transport description. This will allow a predication of confinement far more accurate than overall scaling laws or anomalous diffusion coefficients that neglect ZFs, resulting in confinement optimization of experiments and giving an insight into the initial conditions for a transition into an H-mode regime or the formation of an internal transport barrier.

Bibliography

[1] P. C. Liewer. No Title. *Nuclear Fusion*, 25:543, 1985.

[2] J. Hugill. Transport in Tokamaks - a review of experiments. *Nulcear Fusion*, 23:331–373, 1983.

[3] AJ Wootton, BA Carreras, H Matsumoto, and K. Fluctuations and anomalous transport in tokamaks. *Physics of Fluids B:*, 2(12):2879–2903, 1990.

[4] F Wagner and U Stroth. Transport in toroidal devices-the experimentalist's view. *Plasma Physics and Controlled Fusion*, 35:1321–1371, 1993.

[5] FL Hinton and RD Hazeltine. Theory of plasma transport in toroidal confinement systems. *Reviews of Modern Physics*, 48(2):239–308, 1976.

[6] J. Wesson. *Tokamaks*. Clarendon Press, 1987.

[7] A. Hasegawa, C.G. Maclennan, and Y. Kodama. Nonlinear behavior and turbulence spectra of drift waves and Rossby waves. *Physics of Fluids*, 22:2122, 1979.

[8] A. Hasegawa and M. Wakatani. Self-organization of electrostatic turbulence in a cylindrical plasma. *Physical review letters*, 59(14):1581–1584, 1987.

[9] P H Diamond, S-I Itoh, K Itoh, and T S Hahm. Zonal flows in plasma—a review. *Plasma Physics and Controlled Fusion*, 47(5):R35–R161, May 2005.

[10] G. W. Hammett, M. A. Beer, W. Dorland, S. C. Cowley, and S. A. Smith. Developments in the gyrofluid approach to Tokamak turbulence simulations. *Plasma Physics and Controlled Fusion*, 35:973, 1993.

[11] B Lehnert. Experimental evidence of plasma instabilities. *Plasma Physics*, 9:301–337, 1967.

[12] R. D. Hazeltine and J. D. Meiss. *Plasma Confinement*. Dover Publications, New York, 2003.

[13] R. J. Goldston and P. H. Rutherford. *Plasms Physics*. Taylor and Francis Group, New York, 1995.

[14] G Bateman and Peng Y.-K. M. Magnetohydrodynamic stability of flux-conserving tokamak equilibria. *Physical Review Letters*, 38(15):829–832, 1977.

[15] D Dobrott, DB Nelson, JM Greene, and AH Glasser. Theory of ballooning modes in tokamaks with finite shear. *Physical Review Letters*, 39(15):943–946, 1977.

[16] JW Connor, RJ Hastie, and JB Taylor. Shear, periodicity, and plasma ballooning modes. *Physical Review Letters*, 40(6):396–399, 1978.

[17] VV Arsenin and VA Chuyanov. Suppression of plasma instabilities by the feedback method. *Soviet Physics Uspekhi*, 20(9):736–762, 1977.

[18] AA Galeev, SS Moiseev, and RZ. The theory of the stability of non-uniform plasma and anomalous diffusion. *Journal of Nuclear Energy. Part C, Plasma*, 6:645–669, 1964.

[19] C. Z. Cheng and L Chen. Unstable universal drift eigenmodes in toroidal plasmas. *Physics of Fluids*, 23(9):1770–1773, 1980.

[20] B. Coppi, MN Rosenbluth, and RZ Sagdeev. Instabilities due to temperature gradients in complex magnetic field configurations. *Physics of Fluids*, 10(3):582, 1967.

[21] H. Sugama and W. Horton. Neoclassical and anomalous transport in axisymmetric toroidal plasmas with electrostatic turbulence. *Physics of Plasmas*, 2(8):2989, 1995.

[22] GS Lee and PH Diamond. Theory of ion-temperature-gradient-driven turbulence in tokamaks. *Physics of Fluids*, 29:3291, 1986.

[23] F Wagner, G Becker, K Behringer, D Campbell, and A. Regime of improved confinement and high beta in neutral-beam-heated divertor discharges of the ASDEX Tokamak. *Physical Review Letters*, 49(19):1408, 1982.

[24] EJ Strait, LL Lao, ME Mauel, BW Rice, TS Taylor, KH Burrell, MS Chu, EA Lazarus, TH Osborne, SJ Thompson, and Others. Enhanced confinement and stability in DIII-D discharges with reversed magnetic shear. *Physical review letters*, 75(24):4421–4424, 1995.

[25] FM Levinton, MC Zarnstorff, SH Batha, M. Bell, RE Bell, RV Budny, C. Bush, Z. Chang, E. Fredrickson, A. Janos, and Others. Improved confinement with reversed magnetic shear in TFTR. *Physical review letters*, 75(24):4417–4420, 1995.

[26] W. Horton. Spectral distribution of drift-wave fluctuations in tokamaks. *Physical Review Letters*, 37(19):1269–1272, 1976.

[27] A. Hasegawa and K. Mima. Stationary spectrum of strong turbulence in magnetized nonuniform plasma. *Physical Review Letters*, 39(4):205–208, 1977.

[28] A. Hasegawa and K. Mima. Pseudo-three-dimensional turbulence in magnetized nonuniform plasma. *Physics of Fluids*, 21:87, 1978.

[29] E. Mazzucato. Small-scale density fluctuations in the adiabatic toroidal compressor. *Physical Review Letters*, 36(14):792–794, 1976.

[30] RH Kraichnan. Inertial Ranges in Two-Dimensional Turbulence. *Physics of fluids*, 10:1417, 1967.

[31] G. P. Williams. Planetary Circulations: 1. Barostropic Representation of Jovian and Terrestrial Turbulence. 35:1399, 1978.

[32] P. H. Diamond and Y.-B. Kim. Theory of mean poloidal flow generation by turbulence. *Physics of Fluids B: Plasma Physics*, 3(7):1626, 1991.

[33] A Muhm, A M Pukhov, K. H. Spatschek, and V. Tsytovich. Interaction of regular structures in drift-wave turbulence with small-scale fluctuations. *Physics of Fluids B*, 4(2):336–348, 1992.

[34] a Dyachenko. Wave-vortex dynamics in drift and β-plane turbulence. *Physics Letters A*, 165(4):330–334, May 1992.

[35] Z. Lin, TS Hahm, WW Lee, WM Tang, and RB White. Turbulent transport reduction by zonal flows: Massively parallel simulations. *Science*, 281(5384):1835–1837, September 1998.

[36] H Biglari, PH Diamond, and PW Terry. Influence of sheared poloidal rotation on edge turbulence. *Physics of Fluids B: Plasma Physics*, 2(1):1–3, 1990.

[37] T. S. Hahm. Rotation shear induced fluctuation decorrelation in a toroidal plasma. *Physics of Plasmas*, 1(9):2940, 1994.

[38] M. Rosenbluth and F. Hinton. Poloidal Flow Driven by Ion-Temperature-Gradient Turbulence in Tokamaks. *Physical Review Letters*, 80(4):724–727, January 1998.

[39] FL Hinton and MN Rosenbluth. Dynamics of axisymmetric and poloidal flows in tokamaks. *Plasma physics and controlled Fusion*, 653:A653–A662, 1999.

[40] Z. Lin, T. Hahm, W. Lee, W. Tang, and P. Diamond. Effects of Collisional Zonal Flow Damping on Turbulent Transport. *Physical Review Letters*, 83(18):3645–3648, November 1999.

[41] Z. Lin, T. S. Hahm, W. W. Lee, W. M. Tang, and R. B. White. Gyrokinetic simulations in general geometry and applications to collisional damping of zonal flows. *Physics of Plasmas*, 7(5):1857, 2000.

[42] BN Rogers, W Dorland, and M Kotschenreuther. Generation and stability of zonal flows in ion-temperature-gradient mode turbulence. *Physical review letters*, 85(25):5336–5339, December 2000.

[43] PH Diamond, Y.M. Liang, BA Carreras, and PW Terry. Self-regulating shear flow turbulence: A paradigm for the L to H transition. *Physical review letters*, 72(16):2565–2568, 1994.

[44] PH Diamond, MN Rosenbluth, FL Hinton, M Malkov, J Fleischer, and A Smolyakov. Dynamics of zonal flows and self-regulating drift-wave turbulence. In *17th IAEA Fusion Energy Conference*, 1998.

[45] L Chen, Z Lin, and R White. Excitation of zonal flow by drift waves in toroidal plasmas. *Physics of Plasmas*, 35(18):3021–3023, September 2000.

[46] P.H. Diamond, S. Champeaux, M. Malkov, a. Das, I. Gruzinov, M.N. Rosenbluth, C. Holland, B. Wecht, a.I. Smolyakov, F.L. Hinton, Z. Lin, and T.S. Hahm. Secondary instability in drift wave turbulence as a mechanism for zonal flow and avalanche formation. *Nuclear Fusion*, 41(8):1067–1080, August 2001.

[47] M. a. Malkov and P. H. Diamond. Bifurcation and scaling of drift wave turbulence intensity with collisional zonal flow damping. *Physics of Plasmas*, 8(9):3996, 2001.

[48] A. M. Dimits, G. Bateman, M. A. Beer, B. I. Cohen, W. Dorland, G. W. Hammett, C. Kim, J. E. Kinsey, M. Kotschenreuther, A. H. Kritz, L. L. Lao, J. Mandrekas, W. M. Nevins, S. E. Parker, A. J. Redd, D. E. Shumaker, R. Sydora, and J. Weiland. Comparisons and physics basis of tokamak transport models and turbulence simulations. *Physics of Plasmas*, 7(3):969, 2000.

[49] K. Hallatschek. Turbulent Saturation of Tokamak-Core Zonal Flows. *Physical Review Letters*, 93(6):1–4, August 2004.

[50] N Winsor, JL Johnson, and JM Dawson. Geodesic acoustic waves in hydromagnetic systems. *Physics of Fluids*, 11(11):6–8, 1968.

[51] T. S. Hahm, M. a. Beer, Z. Lin, G. W. Hammett, W. W. Lee, and W. M. Tang. Shearing rate of time-dependent E×B flow. *Physics of Plasmas*, 6(3):922, 1999.

[52] Ai Smolyakov, Ph Diamond, and M Malkov. Coherent structure phenomena in drift wave-zonal flow turbulence. *Physical review letters*, 84(3):491–4, January 2000.

[53] K. Itoh, K. Hallatschek, S. Toda, H. Sanuki, and S.-I. Itoh. Coherent Structure of Zonal Flow and Nonlinear Saturation. *Journal of the Physics Society Japan*, 73(11):2921–2923, November 2004.

[54] K. Itoh, K. Hallatschek, S.-I. Itoh, P. H. Diamond, and S. Toda. Coherent structure of zonal flow and onset of turbulent transport. *Physics of Plasmas*, 12(6):062303, 2005.

[55] MA Malkov, PH Diamond, and MN Rosenbluth. On the nature of bursting in transport and turbulence in drift wave–zonal flow systems. *Physics of Plasmas*, 8:5073, 2001.

[56] K Itoh, K Hallatschek, S Toda, S-I Itoh, P H Diamond, M Yagi, and H Sanuki. Collisional effects on coherent structures of zonal flows and turbulent transport. *Plasma Physics and Controlled Fusion*, 46(5A):A335–A340, May 2004.

[57] K. Hallatschek and D. Biskamp. Transport Control by Coherent Zonal Flows in the Core/Edge Transitional Regime. *Physical Review Letters*, 86(7):1223–1226, February 2001.

[58] a. Fujisawa, K. Itoh, H. Iguchi, K. Matsuoka, S. Okamura, a. Shimizu, T. Minami, Y. Yoshimura, K. Nagaoka, C. Takahashi, M. Kojima, H. Nakano, S. Ohsima, S. Nishimura, M. Isobe, C. Suzuki, T Akiyama, K. Ida, K. Toi, S.-I. Itoh, and P. Diamond. Identification of Zonal Flows in a Toroidal Plasma. *Physical Review Letters*, 93(16):1–4, October 2004.

[59] A. Fujisawa, Akihiro Shimizu, Haruhisa Nakano, Shinsuke Ohshima, Kimitaka Itoh, Yoshihiko Nagashima, Sanae-I. Itoh, Harukazu Iguchi, Yasuo Yoshimura, Takashi Minami, Keiichi Nagaoka, Chihiro Takahashi, Mamoru Kojima, Shin Nishimura, Mitsutaka Isobe, Chihiro Suzuki, Tsuyoshi Akiyama, Takeshi Ido, Keisuke Matsuoka, Shoichi Okamura, and Patrick H. Diamond. Causal Relationship between Zonal Flow and Turbulence in a Toroidal Plasma. *Journal of the Physical Society of Japan*, 76(3):033501, February 2007.

[60] a. Fujisawa, K. Itoh, a. Shimizu, H. Nakano, S. Ohshima, H. Iguchi, K. Matsuoka, S. Okamura, T. Minami, Y. Yoshimura, K. Nagaoka, K. Ida, K. Toi, C. Takahashi, M. Kojima, S. Nishimura, M. Isobe, C. Suzuki, T. Akiyama, T. Ido, Y. Nagashima, S.-I. Itoh, and P. H. Diamond. Experimental studies of zonal flow and field in compact helical system plasma. *Physics of Plasmas*, 15(5):055906, 2008.

[61] D. Gupta, R. Fonck, G. McKee, D. Schlossberg, and M. Shafer. Detection of Zero-Mean-Frequency Zonal Flows in the Core of a High-Temperature Tokamak Plasma. *Physical Review Letters*, 97(12):1–4, September 2006.

[62] A. Fujisawa. A review of zonal flow experiments. *Nuclear Fusion*, 49(1):013001, January 2009.

[63] K Hallatschek. Nonlinear three-dimensional flows in magnetized plasmas. *Plasma Physics and Controlled Fusion*, 49(12B):B137–B148, December 2007.

[64] K. Hallatschek and a. Zeiler. Nonlocal simulation of the transition from ballooning to ion temperature gradient mode turbulence in the tokamak edge. *Physics of Plasmas*, 7(6):2554, 2000.

[65] D Montgomery and T Hatori. Analytical estimates of turbulent MHD transport coefficients. *Plasma Physics and Controlled Fusion*, 26(5):717–730, May 1984.

[66] J. Candy and R.E. Waltz. An Eulerian gyrokinetic-Maxwell solver. *Journal of Computational Physics*, 186(2):545–581, April 2003.

[67] J. Anderson, H. Nordman, R. Singh, and J. Weiland. Zonal flow generation in ion temperature gradient mode turbulence. *Physics of Plasmas*, 9(11):4500, 2002.

[68] a. I. Smolyakov, P. H. Diamond, and M. V. Medvedev. Role of ion diamagnetic effects in the generation of large scale flows in toroidal ion temperature gradient mode turbulence. *Physics of Plasmas*, 7(10):3987, 2000.

[69] R. D. Hazeltine and F. L. Waelbroeck. *The Framework of Plasma Physics*. Westview Press, Cambridge, 2004.

[70] V. D. Shafranov. *Review of Plasma Physics*, volume 2. Consultants Bureau, New York, 1966.

[71] A. A. Ware and F. A. Haas. Stability of a circular toroidal plasma under average magnetic well conditions. *Phys. Fluids*, 9:956, 1966.

[72] J. M. Greene, J. L. Johnson, and K. E: Weimer. Tokamak equilibrium. *Phys. Fluids*, 14(3):671, 1971.

[73] W Horton. Nonlinear drift waves and transport in magnetized plasma. *Physics Reports*, 192(1-3):1–177, August 1990.

[74] A. Zeiler. *Tokamak edge turbulence*. Habilitation, Max-Planck-Institute for Plasma Physics, 1999.

[75] Allen H. Boozer. What is a stellarator? *Physics of Plasmas*, 5(5):1647, 1998.

[76] J. D. Jackson. *Classical Electrodynamics*. Wiley, New York, 1999.

[77] R. D. Hazeltine and F. L. Waelbroeck. *The Framework of Plasma Physics*. Westview Press, Cambridge, 2004.

[78] S.I. Braginskii. Transport processes in a plasma. *Consultants Bureau, New York*, 1:205, 1965.

[79] A. N. Kaufman. Plasma viscosity in a magnetic field. *Phys. Fluids*, 3:610, 1960.

[80] A. Zeiler. *Tokamak edge turbulence*. PhD thesis, Max-Planck-Institute for Plasma Physics, 1999.

[81] F. L. Hinton and C. W. Horton. Amplitude limitation of a collisional drift wave instability. *Phys. Fluids*, 14(1):116, 1971.

[82] S. Tsai, F. Perkins, and T. Stix. Thermal conductivity and low frequency waves in collisional plasmas. *Phys. Fluids*, 13(8):2108, 1970.

[83] PN Guzdar, JF Drake, D. McCarthy, AB Hassam, and CS Liu. Three-dimensional fluid simulations of the nonlinear drift-resistive ballooning modes in tokamak edge plasmas. *Physics of Fluids B: Plasma Physics*, 5:3712, 1993.

[84] W. Horton. Drift waves and transport. *Reviews of Modern Physics*, 71(3):735–778, April 1999.

[85] DW Ross and SM Mahajan. Are drift-wave eigenmodes unstable? *Physical Review Letters*, 40(5):324–327, 1978.

[86] PN Guzdar, L Chen, PK Kaw, and C Oberman. Effect of magnetic shear on dissipative drift-wave instabilities. *Physical Review Letters*, 40(24):1566–1570, 1978.

[87] KT Tsang, JC Whitson, JD Callen, PJ Catto, and J Smith. Drift Alfven waves in tokamaks. *Physical Review Letters*, 41(8):557–561, 1978.

[88] PJ Catto, MN Rosenbluth, and KT Tsang. Resistive Drift-Alfven waves in sheared magnetic fields. *Physics of Fluids*, 22(7):1284–1288, 1979.

[89] W Jr Horton, DI Choi, and WM Tang. Toroidal drift modes driven by ion pressure gradients. *Physics of Fluids*, 24(6):1077–1085, 1981.

[90] F Romanelli. Ion temperature gradient driven modes and anomalous ion transport in tokamaks. *Physics of Fluids B: Plasma Physics*, 1(5):1018–1025, 1989.

[91] S Brunner, M Fivaz, TM Tran, and J Vaclavik. Global approach to the spectral problem of microinstabilities in tokamak plasmas using a gyrokinetic model. *Physics of Plasmas*, 5(11):3929–3949, 1998.

[92] A. Zeiler, D. Biskamp, JF Drake, and BN Rogers. Transition from resistive ballooning to η driven turbulence in tokamaks. *Physics of Plasmas*, 5(7):2654, 1998.

[93] S Champeaux and PH Diamond. Streamer and zonal flow generation from envelope modulations in drift wave turbulence. *Physics Letters A*, 288(3-4):214–219, September 2001.

[94] P Beyer, S Benkadda, X Garbet, and Ph Diamond. Nondiffusive transport in tokamaks: three-dimensional structure of bursts and the role of zonal flows. *Physical review letters*, 85(23):4892–5, December 2000.

[95] V. B. Lebedev, P. H. Diamond, V. D. Shapiro, and G. I. Soloviev. Modulational interaction between drift waves and trapped ion convective cells: A paradigm for the self-consistent interaction of large-scale sheared flows with small-scale fluctuations. *Physics of Plasmas*, 2(12):4420, 1995.

[96] K. L. Sidikman, B. a. Carreras, P. H. Diamond, and L. Garcia. Theory of electric-field curvature effects on long-wavelength drift wave turbulence. *Physics of Plasmas*, 1(5):1142, 1994.

[97] P. Kaw, R. Singh, and P. H. Diamond. Coherent nonlinear structures of drift wave turbulence modulated by zonal flows. *Plasma Physics and Controlled Fusion*, 44:51–59, 2002.

[98] M Camac, AR Kantrowitz, MM Litvak, RM Patrick, and HE Petschek. Shock waves in collision-free plasmas. *Nuclear Fusion, Suppl. 2*, page 423, 1962.

[99] AA Galeev and VI Karpman. Turbulence theory of a weakly nonequilibrium low density plasma and structure of shock waves. *Sov. Phys.–JETP*, 17:403–409, 1963.

[100] a. I. Smolyakov and P. H. Diamond. Generalized action invariants for drift waves-zonal flow systems. *Physics of Plasmas*, 6(12):4410, 1999.

[101] N. Guertler and K. Hallatschek. Predicting Zonal Flows - A Comprehensive Reynolds-Stress Response-Functional from First-Principles-Plasma-Turbulence Computations. *submitted to PRL*, 2011.